S. B. M. VELDHUIJSEN

THE SPATIAL AND TEMPORAL PATTERNS OF REFREEZING IN A HIMALAYAN CATCHMENT AND ITS EFFECTS ON RUNOFF

MSc Thesis

Universiteit Utrecht

The spatial and temporal patterns of refreezing in a Himalayan catchment and its effects on runoff

MSc Thesis
by
S.B.M. Veldhuijsen
4149734

Supervisor: dr. ir. R. J. de Kok

prof. dr. W. W. Immerzeel

Co-supervisors: E. E. Stigter MSc

J. F. Steiner MSc

MSc Thesis Earth, Surface and Water

Department of Physical Geography

Utrecht University

Utrecht, The Netherlands

April 2020

Universiteit Utrecht

ABSTRACT

Snowmelt contributes significantly to the annual runoff in the Himalaya and both the timing and volume of snowmelt are of critical importance for downstream communities. Refreezing of meltwater within the snowpack is known to significantly influence annual snow mass and energy balances in the Arctic and Antarctica. The conditions for refreezing in the Himalaya are considered even more favorable, however the importance and patterns of meltwater refreezing in the region are still largely unknown. Hence, in this study, insight is gained in the role and importance of refreezing in the Langtang catchment in the Nepalese Himalaya. We have assessed, for the first time to our knowledge, the spatial and temporal patterns, and the effect on melt runoff of refreezing in the current and a changed future climate at a catchment-scale in the Himalaya. This was done by using the modified seNorge model (v2.0), which includes a physically based parameterization of refreezing based on Stefan's Law.

Since snow models are highly sensitive to small changes in meteorological input data and the quality of input data often limits the performance, the first part of this study focuses extensively on developing meteorological forcing data, which were derived from an elaborate network of meteorological stations and high-resolution WRF simulations. In the second part of this study, the refreezing model was forced with the meteorological data and run at an hourly timestep. The model validation showed that the results are generally in good agreement with snow satellite imaginary and in-situ snow depth and SWE observations. The refreezing model results revealed that refreezing significantly influences the snow mass balance in the Langtang catchment, with a contribution of 131 mm year^{-1} (35% of the melt runoff). The spatial and temporal pattern of refreezing are predominantly controlled by the amount of SWE and the magnitude of the diurnal temperature fluctuations around the freezing point. Therefore, refreezing has a strong relation with elevation and mostly occurs in the pre- and post-monsoon seasons. Intra-annual variability is primarily caused by variations of snowfall in the post-monsoon and winter. 67% of the refreezing occurs during the same day that the melt is generated, which emphasizes the importance of using sub-daily temporal resolution. The results show that refreezing is important for snow persistence and the timing of melt runoff, and excluding it in models consequently results in an earlier melt runoff onset.

In the third part of this study, climatic sensitivity experiments were performed, which revealed that the model is highly sensitive to temperature and incoming shortwave radiation changes. Future climate change will cause a seasonal runoff shift, with predominantly more runoff in the pre-monsoon and less in the monsoon. The results reveal that refreezing influences the response of the snowpack to future climate change, as it moderates this seasonal runoff shift. We conclude that including refreezing with sub-daily temporal resolution is required for a detailed assessment of snow dynamics and is highly relevant for the modeling of runoff in the current and a changed future climate in the Himalaya.

CONTENTS

Figures

Tables

Abbreviations
AWS Automatic Weather Station
MODIS Moderate-resolution Imaging Spectroradiometer
WRF World Research and Forecasting
SWE Snow Water Equivalent

Definition seasons
Winter	January to February
Pre-monsoon	March to May
Monsoon	June to September
Post-monsoon	October to December

1   INTRODUCTION

1.1   Background

Many large rivers, such as the Indus, Ganges, Brahmaputra, Yangtze and Yellow rivers, originate in the Himalaya and the adjacent Tibetan plateau. These rivers are providing freshwater to over 1.4 billion people living downstream, who are dependent on this water supply for their irrigated agriculture, food security and water availability (Immerzeel et al. 2010). Additionally, the Himalaya itself has a high diversity of species and ecosystems, which also depend on the periodically availability of freshwater (Xu et al. 2009). In fact, these river basins all score high on the global Water Tower Index, an importance index, where water towers are ranked in terms of their water supply, their downstream demands of ecosystems and societies and their overall vulnerability (Immerzeel et al. 2019).

The Himalaya and the Tibetan plateau are often called "The Water Towers" of Asia, since they store precipitation as snow and ice, thereby sustaining seasonal water availability. Water is stored as a buffer over multiple years as ice and perennial snow and within a year as seasonal snow. Runoff from snow and glacier melt contributes significantly to annual runoff in this region, although there is a large spatial variation in the contribution. Snowmelt contributes 21.8% of the annual runoff in the upper Indus Basin, 9.0% in the Upper Brahmaputra basin and 8.6% in the upper Ganges Basin. Glacier melt contributes 40.6% of the annual runoff in the upper Indus Basin, 11.5% in the upper Ganges Basin and 15.9% in the upper Brahmaputra Basin (Lutz et al. 2014). Especially during pre- and early monsoon, when the runoff consists mostly of snow and glacier melt, the meltwater is important to sustain enough runoff for the large irrigation water demand (Bookhagen and Burbank, 2010). Melt runoff in the non-monsoon seasons is also important to sustain enough runoff for hydropower generation, which meets about 95% of electric demand in Nepal (Sharma and Shakya, 2006). On the other hand, the region is also affected by flooding disasters caused by fast melting of snow and glaciers and extreme precipitation events (Elalem and Pal, 2015).

1.2   Problem definition

Observational studies have shown an overall increasing trend in temperature in the Himalaya. In fact, the increase in temperature from 1975 to 2005 in the Himalaya was more than twice as high than the global average (Shrestha et al. 2012). This is the result of elevation-dependent warming, an amplified warming response at higher elevation, due to various feedback system, such as the snow and ice albedo feedback (Wang et al. 2014; Pepin et al. 2015). As a result of this ongoing climate change, the amount of water stored as ice and snow in the Himalaya has already reduced substantially (Bolch et al. 2012; Kulkarni et al. 2010). Both increasing temperatures and increasing precipitation are expected to further affect this water storage and the hydrology of headwater catchments in the Himalaya (Aktar et al. 2008; Immerzeel et al. 2010; Lutz et al. 2014). Glacio-hydrological models make it possible to predict these changes. However, the lack of hydro-meteorological and cryosphere data, the large climatic heterogeneity and the uncertainty in glacier and snow dynamics make the modelling in this region challenging (Pellicciotti et al. 2012; Beniston, 2003). Additionally, there are also large uncertainties related to future climate change projections, and especially precipitation projections are uncertain, with no clear existing consensus (e.g. Wu et al. 2017; Rangwala et al. 2020).

A study conducted by Immerzeel et al. (2010) showed that from 2046 to 2065 the upstream water supply is expected to decrease for the Indus (-8.4%), the Ganges (-17.6%), Brahmaputra (-

19.6%) and the Yangtze rivers (-5.2%). Accordingly, Lutz et al. (2014) also projects an increase in upstream runoff until at least 2050 for the Indus, the Ganges and the Brahmaputra. Rising temperatures cause enhanced glacier melt, thereby releasing long-term glacier storage, which together with increased mean upstream rainfall explains the initial increase in discharge (Immerzeel et al. 2010; Lutz et al. 2014; Hock et al. 2019). The shrinking and retreating to higher elevation of the glaciers eventually causes a decrease in meltwater production and therefore a decrease in runoff (Hock et al. 2019). However, the decrease in meltwater is partly compensated by the increase in mean upstream rainfall (Immerzeel et al. 2010). This glacier shrinkage can also cause seasonal shifts in the melt runoff peak (Hock et al. 2019). Additionally, it is important to note that although annual runoff may only change slightly, there could still be a significant seasonal distribution change or composition change. In fact, these seasonal shifts and the increase in hydrological extremes pose the biggest threats to downstream societies. For the Indus reduced summer runoff is expected, which threatens the availability of water for irrigation, while the intensity and frequency of extreme discharge are also expected to increase, resulting in an increased risk of flooding (Lutz et al. 2016). For the Ganges and the Brahmaputra increased summer runoff is expected, which also implies an increase in flooding events (Nepal and Shrestha, 2015). However, due to unreliable data input, the large spatial scale and therefore relatively simple approaches, existing models show varying results (Pellicciotti et al. 2012).

Previous studies have predominantly focused on the effects of climate change on glacier melt and the resulting runoff. However, snowmelt contributes significantly to annual runoff in the Himalaya (Lutz et al. 2014; Bookhagen and Burbank, 2010) and both the timing and volume of snowmelt are of critical importance for the downstream communities (Smith et al. 2017; Biemans et al. 2019). Additionally, a recent study reveals that snowmelt is more sensitive to future climate change than glacier melt (Kraaijenbrink et al. *in press*). Snow is also important for regional climate through atmospheric land feedbacks, such as the snow albedo feedback as mentioned above. Snow accumulation in the Himalaya generally occurs from November to March, while snowmelt is mainly observed from April to June. During March to June, snowmelt is generally the predominent source of runoff and from July to September it forms a significant contribution to glacier melt and rain (Bookhagen and Burbank, 2010).

Studies about snowmelt in the Himalaya previously mainly used remotely sensed snow cover data to simulate snowmelt runoff (e.g. Immerzeel et al. 2009; Bookhagen and Burbank, 2010; Jain et al. 2010; Wulf et al. 2016). However, for more accurate estimates of the snowmelt runoff, the snow water equivalent (SWE) should be considered and consequently an increasing number of such snow models have been developed and implemented in the Himalaya recently (Stigter et al. 2017; Saloranta et al. 2019). Over the last years many important snow processes, such as compaction, avalanching, sublimation and evaporation have been quantified with field observations, parameterizations and modelling, which strongly increased our understanding about snow dynamics in the Himalaya (e.g. Ragettli et al. 2015; Stigter et al. 2017; Stigter et al. 2018; Kirkham et al. 2019; Saloranta et al. 2019).

Refreezing of meltwater within the snowpack is known to significantly influence the annual snow mass and energy balances in the Subarctic, Arctic and Antarctic, where it has been rather well-studied with various parameterization schemes (e.g. Bengtsson, 1982, Reijmer et al. 2012; Van Pelt et al. 2016). A study of the snowpack of a temperate alpine Canadian glacier estimates that 10% of the total melt refreezes and expects that the importance of refreezing is more significant for colder alpine environments such as the Himalaya (Samimi and Marshall, 2017). Accordingly,

studies of an alpine glacier in the Andes reveals that above 4,000 m a.s.l. a significant amount of the annual melt refreezes, with a peak value of 610 mm (~50% of the melt) between 4,500 – 5,000 m a.s.l. (Ayala et al. 2017b). The conditions in the Himalaya are favorable for refreezing, especially in the pre- and post-monsoon seasons, as the daily temperatures, have a high diurnal variability and the elevation of the 0°C line is located around 4,500 m a.s.l. (Immerzeel et al. 2014; Heynen et al. 2016). Observations at 4,200 and 5,000 m a.s.l. showed that the temperature fluctuates around 0°C for 44 and 57% of the days, respectively (Saloranta et al. 2019).

Recently, for the first time, a snow modelling study in the Himalaya has been conducted, which includes a catchment-wide process-based parameterization of refreezing. That study estimates that 36% of the total snowmelt refreezes and up to 48% during the non-monsoon seasons (Saloranta et al. 2019). Some previous studies in the Himalaya already used uncertain degree-day approaches to include refreezing in their snow models (Konz et al. 2007; Saloranta et al. 2016; Stigter et al. 2017). A glacier mass balance study conducted on the Tibetan Plateau shows that from May to September about 60% of the meltwater in the accumulation zone refreezes (Fujita et al. 1996). Diurnal refreezing has also been observed in the field on ice cliffs of a Himalayan glacier and including refreezing in the model of that study improved the melt simulation during the post-monsoon season considerably (Steiner et al. 2015). Residual energy flux calculations of Bonekamp et al. (2019) reveal that refreezing could amount up to 60% of the total melt in the Langtang catchment. However, the importance and patterns of meltwater refreezing in the Himalaya are still largely unknown. Refreezing causes a delay of meltwater runoff from the snowpack, since more energy is needed to melt the snowpack (Van Pelt et al. 2012). It is therefore essential to account for refreezing in snow model when simulating snowpack persistence and snowmelt runoff. It is also important when simulating the effects of future climate change, since refreezing is very sensitive to changes in temperature (Van Pelt et al. 2016). Therefore, it is important to characterize the patterns and effect on melt runoff of refreezing, which can be done with a snow model.

Three main types of snow models exist: temperature-index models, enhanced temperature-index models and surface energy balance models. Temperature-index models only require inputs of temperature and precipitation and enhanced temperature-index models also require inputs of shortwave radiation (Pellicciotti et al. 2005). Surface energy balance models require temperature, precipitation, shortwave radiation, longwave radiation, wind, humidity and air pressure (Armstrong and Brun, 2008). Due to limited availability of meteorological data, most hydrological models used in the Himalaya model snowmelt with temperature-index or enhanced temperature-index models (Litt et al. 2019). It is commonly acknowledged that air temperature is of great importance in estimating melt, since longwave radiation is the most dominant energy source, of which 70-90% comes from the first 1 km of the atmosphere and for which the surface air temperature is the most controlling factor. The other two most important energy sources, shortwave radiation and sensible heat are also strongly correlated with air temperature (Ohmura, 2001). Additionally, several studies show that simpler models can perform as well as more sophisticated models (Rutter et al. 2009; Essery et al. 2013; Magnusson et al. 2015). Temperature-index models with the degree-day method generally yield good simulations of daily snowpack runoff (Avanzi et al. 2016). However, the recent study of Litt et al. (2019) shows that in high elevation catchments at low latitudes, air temperature only correlates partially with the surface energy balance model and that incoming shortwave radiation is the most important energy input. Additionally, with sub-daily temporal resolution enhanced temperature-index models, which also require incoming shortwave radiation outperform temperature-index models in high elevation catchments (Avanzi et al. 2016). The results of

Saloranta et al. (2019) show that a sub-daily time step improves the snowmelt modeling substantially, because it captures the diurnal melt-refreeze cycles.

1.3   Objectives and research questions

The preceding section shows that knowledge about refreezing in the Himalaya is largely lacking, while it is has a significant effect on snow dynamics. In this study we therefore aim to gain insight in the importance and role of meltwater refreezing in the Langtang catchment in Nepal. The modified seNorge model (v2.0), which includes a process based parameterization of refreezing, is most suitable for this, and was therefore used for this purpose (Saloranta et al. 2019).

The overall objective of this study is:

To characterize the spatial and temporal patterns and the effect on melt runoff of the refreezing of snow meltwater in the current and changed future climate in the Langtang catchment, Nepal.

Based on the aim of this study, the following three research questions will be addressed:

Q1:   What are the spatial and temporal patterns of refreezing?
Q2:   How does refreezing impact melt runoff in the current climate?
Q3:   How does refreezing impact melt runoff in a changed future climate?

2   METHODS AND DATA

2.1   Study area

The Langtang catchment is located in the central part of the Nepalese Himalaya, 70 km north of Kathmandu (Figure 1a,b). The catchment has an area of 584 km², including 140 km² of glacier area (Collier and Immerzeel, 2015). The catchment has a complex topography with elevations ranging
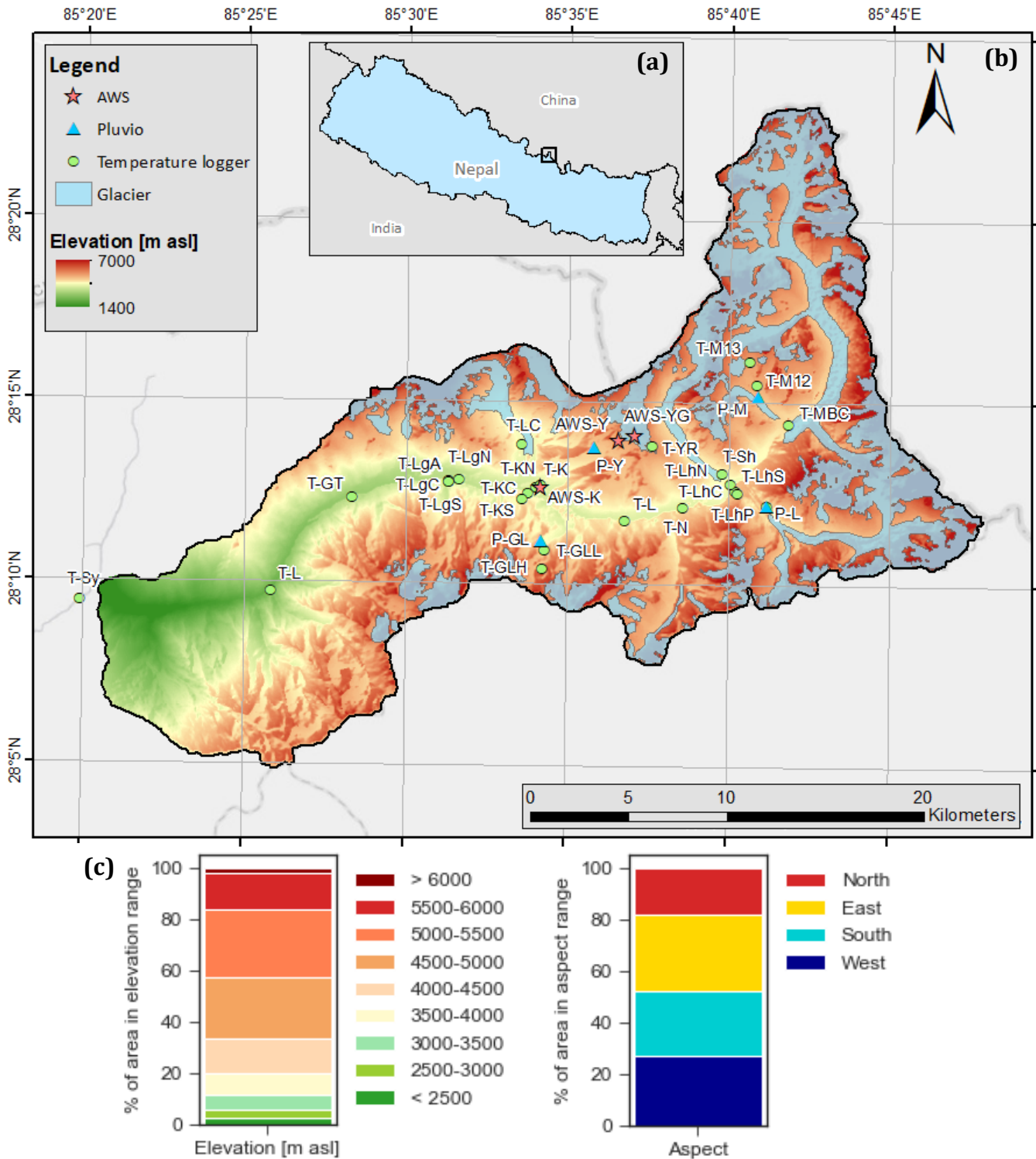

FIGURE 1 | Study area location. **(a)** Location of the Langtang catchment in Nepal. **(b)** Location of the meteorological stations and glaciers within the Langtang catchment. **(c)** Elevation and aspect distribution in the catchment. Glacier outlines are obtained from glims.org. (Snow-Y not shown, but located at 200 m from AWS-Y)

from 1,406 m a.s.l. at the catchment outlet near Syaphru to 7,234 m a.s.l. at the highest Peak, Langtang Lirung. Figure 1c shows the elevation and aspect distribution of the catchment. The Langtang River flows through the main valley, which is U-shaped upstream and V-shaped downstream, and is part of the Trishuli River system, which is a major tributary of the Narayani River, which is a major tributary of the Ganges.

The climate of the catchment is dominated by monsoon circulation with predominant easterly winds in the monsoon and westerly winds in the non-monsoon season. Based on Immerzeel et al. (2014) and Saloranta et al. (2019) we defined the winter from January to February, the pre-monsoon from March to May, the monsoon from June to September and the post-monsoon from October to December. During the monsoon 68 to 89% of the total annual precipitation occurs, with precipitation events nearly every day (Immerzeel et al. 2014). During the winter the wet day frequencies are much lower, while the intensities are generally higher than in the monsoon. During the pre-monsoon there is occasionally precipitation, while during the post-monsoon there is almost no precipitation (Immerzeel et al. 2014). Additionally, there is a strong seasonal variation in spatial precipitation patterns, and there is a strong interaction between topography and precipitation patterns (Collier and Immerzeel et al. 2015). The mean daily temperature from 1957 to 2002 at Kyangin, which is located at 3,920 m a.s.l., is 0.5 °C from October to June and 8.4°C during the monsoon (Uppala et al. 2005) and the temperatures in the catchment are strongly correlated with elevation (Immerzeel et al. 2014). The river has a glacial discharge regime with maximum discharges in July and August, due to high melt rates and monsoon precipitation, and minimum discharges during the winter due to low air temperatures (Immerzeel et al. 2012).

Snowmelt is with 40% the most important contributor to runoff in in the upper part of the catchment (upstream of Kyangjin) (Ragettli et al. 2015). 211 mm (17%) of the annual precipitation is estimated to fall as snow, predominantly during strong precipitation events in winter (Immerzeel et al. 2014). However, for the upper part of the catchment (upstream of Kyangjin) above 5,600 m a.s.l. 75% of the total annual snowfall occurs during the monsoon (Steinegger et al. 1993).

The height of the 0°C isotherm varies from about 3,000 m a.s.l. during the winter to 6,000 m a.s.l. during the monsoon (Shea et al. 2015). Snow cover and the snowline elevation in the catchment therefore have a strong seasonality. The lowest snowline elevation and highest snow cover fraction values occur in the pre-monsoon followed by the winter, while the highest snowline elevation and lowest snow cover fraction values occur in the monsoon and December (Girona-Mata et al. 2019). The annual mean snow line elevation ranges from about 5,000 m a.s.l. to 5,500 m a.s.l. (Girona-Mata et al. 2019). The highest inter-annual variability in snowcover and snow line elevation are observed during winter, which is related to a high inter-annual variability in timing of large snowfall events (Girona-Mata et al. 2019). Differences in amount and timing of incoming shortwave radiation result in higher snowline elevation values on south-facing slopes than on north-facing slopes, and higher values on west-facing slopes than on east-facing slopes. Additionaly, positive snow line elevation gradients are found from the west towards the east and from the north to the south, both controlled by spatial precipitation patterns (Immerzeel et al. 2014; Girona-Mata et al. 2019). Over the last decades, decreasing snow cover trends in the winter and monsoon season have been observed, which is related to increasing temperatures (Thapa et al. 2020).

2.2 Obsevational data

2.2.1 Meteorological data

Several air temperature, precipitation and incoming shortwave radiation measurements were available between April 2012 and April 2019 at elevations ranging from 1,395 to 5,500 m a.s.l. (Figure 1b and Tables 1 and 2). Temperature, precipitation, and incoming shortwave radiation were monitored at three AWSs (Figure 2). The sensors recorded with a 10 min interval, after which the hourly mean temperature and incoming shortwave radiation and the hourly cumulative

TABLE 1 | Location and characteristics of the observational stations.

Station	Code	Elevation (m a.s.l.)	Latitude	Longitude	Start date (d-m-y)	End date (d-m-y)
AWS						
Kyangjin	AWS-K	3,862	28.21081	85.56948	01-01-2012	01-05-2019
Yala	AWS-Y	5,090	28.2323	85.60967	01-01-2012	05-05-2019
Yala Glacier	AWS-YG	5,350	28.23463	85.61797	07-05-2016	15-10-2017
Pluvio Yala						
Ganja La	P-GL	4,361	28.18625	85.56961	01-01-2012	01-05-2019
Langshisha	P-L	4,452	28.20265	85.68619	25-10-2013	02-01-2015
Morimoto	P-M	4,919	28.25296	85.68152	29-10-2013	06-05-2019
Yala	P-Y	4,831	28.229	85.597	07-05-2012	25-04-2015
Temperature loggers						
Ganja La High	T-GLH	4,870	28.17355	85.5704	10-05-2014	04-11-2014
Ganja La Low	T-GLL	4,472	28.18177	85.57191	16-10-2013	30-05-2015
Ghoda Tabela	T-GT	3,096	28.2055	85.472	05-11-2012	03-05-2013
Jathang	T-L	3,947	28.1958	85.6132	05-05-2012	12-10-2014
Kyangjin	T-K	3,857	28.21096	85.56686	04-09-2012	02-10-2013
Kyangjin Center	T-KC	3,786	28.20807	85.56287	03-11-2012	05-05-2013
Kyangjin South	T-KS	3,899	28.21192	85.56968	03-11-2012	05-05-2013
Kyangjin North	T-KN	3,800	28.20513	85.56009	03-11-2012	05-05-2013
Lama	T-L	2,492	28.16212	85.43073	01-05-2012	08-10-2014
Langshisha Center	T-LhC	4,109	28.20965	85.67008	31-10-2012	27-10-2014
Langshisha North	T-LhN	4,113	28.21292	85.66759	31-10-2012	19-05-2013
Langshisha Pluvio	T-LhP	4,437	28.202648	85.686192	22-05-2013	19-04-2016
Langshisha South	T-LhS	4,120	28.20853	85.671	31-10-2012	19-05-2013
Langtang Above	T-LgA	3,557	28.21398	85.52745	02-05-2012	09-10-2013
Langtang Center	T-LgC	3,519	28.21294	85.52208	11-05-2012	05-05-2013
Langtang North	T-LgN	3,568	28.213389	85.522138	11-05-2012	05-05-2013
Langtang South	T-LgS	3,538	28.2126667	85.521694	11-05-2012	05-05-2013
Lirung Camp	T-LC	4,141	28.23027	85.55958	05-11-2013	23-10-2014
Morimoto 12	T-M12	5,101	28.25814	85.68103	16-10-2013	29-10-2014
Morimoto 13	T-M13	5,308	28.26879	85.67692	16-10-2013	29-10-2014
Morimoto BC	T-MBC	4,617	28.24014	85.69743	31-10-2013	22-10-2015
Numhang	T-N	3,983	28.20213	85.64313	05-05-2012	20-10-2015
Shalbacum	T-Sh	4,295	28.217581	85.663023	05-09-2013	10-08-2015
Syaphru	T-Sy	1,395	28.15743	85.33218	01-05-2012	01-05-2013
Yala Ridge	T-YR	5,500	28.23023	85.62721	21-10-2015	16-10-2016
Snow station						
Yala	S-Y	5,090	28.23331	85.60867	26-10-2017	27-05-2019

precipitation values were logged. Additionally, temperature and precipitation were monitored at four Pluvio stations with a 15 min interval. Temperature was also monitored at twenty-four locations with temperature loggers at a 5-, 10- or 15-min interval.

Temperatures were measured about 2 m above the surface and to avoid influence of direct solar radiation the sensors were covered with an unventilated radiation shield. The Pluvio sensors are based on the weighing principle. All the stations sites expect for AWS Yala Glacier are located off-glacier. The stations have various coverages with some interruption due to battery problems, memory limitations, extreme conditions and damage. Table 2 provides an overview of the technical characteristics of the sensor incorporated within the stations.

TABLE 2 | Technical characteristics of the observational stations.

Parameter	Sensor	Range	Accuracy (±)	Recording interval
AWS				
Air temperature	Rotronic HC2	-50 - +100°C	0.1 °C	10 min
	Campbell HC2S3	-50 - +100°C	0.1 °C	10 min
Precipitation	OTT Pluvio2		1%	10 min
Shortwave incoming radiation	CNR4 Kipp & Zonen		10%	10 min
Snow depth	< 2015: Jenoptik SHM30	2.0 - 2.7 m	5 mm	6 min
	> 2015: SR50a	2.0 - 2.7 m	10 mm	6 min
Pluvio				
Air temperature	Campbell 109-L	-50 - +70°C	< -10 °C: 0.60 °C > -10 °C: 0.25 °C	15 min
Precipitation	OTT Pluvio2		1%	15 min
Snow depth	SR50	< 2.7 m	10 mm	15 min
Temperature logger				
Air temperature	HOBO TidbiT v2 UTBI-001	-20 - +70°C	0.2 °C	5/10/15 min
Snow station				
Snow depth	SR50a	2.0 – 2.7 m	10 mm	6 min
SWE	Campbell CS725	< 600 mm	>300 mm: 15mm <300 mm: 15%	24 hours

2.2.2   In situ snow depth and SWE data

Snow depth was measured at AWS Yala BC, Pluvio Yala and Snow Station Yala. The sensors are mounted between 2.0 to 2.7 m. At AWS Yala BC the sensors recorded every 6 min, after which the best quality value was logged every hour. At Pluvio Yala the sensors recorded every 15 minutes. The SWE was measured at AWS Yala BC. The sensor measures gamma-rays emitted from Potassium (^{40}K) and Thallium (^{208}Tl), which are weak radioactive elements that are naturally present in the underlying soil and overburden (Stranden et al. 2015). When water is present these gamma rays are progressively reduced in strength, due to absorption and scattering of the energy. This attenuation of the gamma rays is used to calculate the SWE. The sensor is mounted at 3.0 m and integrates the gamma-rays strength over a period of 24 hours, after which 6-hourly values are logged.

FIGURE 2 | AWS Kyangjin (Photo by: dr. J. Kirkham).

2.3   Meteorological analysis

It is evident that reliable meteorological forcing data is a crucial element in hydrological modelling, since the quality of input data and not model formulation often limits the performance of models (Magnusson et al. 2015). Additionally, the modified seNorge (v2.0) model is found to be highly sensitive to changes in temperature and precipitation input (Stigter et al. 2017; Immerzeel et al. 2014). Hence, the first part of this study will focus extensively on developing accurate meteorological forcing data.

2.3.1   Air temperature

Air temperature is an key control on processes affecting snow, such as snowfall, melt, refreezing and albedo decay and is therefore an essential input to snow models. Air temperature is generally assumed to decrease with elevation according to constant lapse rates (Lundquist et al. 2008; Marshall and Sharp, 2009). Observed temperatures can therefore be extrapolated according to the lapse rates in complex terrain. Snow model outputs in the catchment are found to be highly sensitive to small changes in temperature lapse rates, due to the extreme topography, thereby highlighting the importance of approximating them accurately (Stigter et al. 2017; Immerzeel et al. 2014). Lapse rates (LR; °C m^{-1}) can be calculated as follows (Petersen and Pellicciotti, 2011):

$$LR = \frac{T_1 - T_2}{z_1 - z_2} \tag{1}$$

where T_1 and T_2 are the air temperatures (°C) of respectively the higher and lower locations, and z_1 and z_2 the associated elevations (m a.s.l.). However, in this study the lapse rates are calculated as a linear regression through all the measuring locations, which allows more field data to be included. Additionally, this makes it possible to calculate the strength and the significance of the relationship between temperature and elevation. The resulting slope indicates the lapse rate, the R-squared value indicates the strength of the correlation and the p-value indicates the significance.

The temperature lapse rates in the catchment have a high diurnal variability, which is important for snowmelt and refreezing processes especially considering the extreme topography (Immerzeel et al. 2014; Heynen et al. 2016). Additionally, the diurnal variability of the temperature lapse rates differs between the seasons (Petersen and Pellicciotti 2011; Kattel et al. 2013; Immerzeel et al. 2014; Collier and Immerzeel, 2015; Heynen et al. 2016), and also within the seasons (Heynen et al. 2018), mainly as a result of the differences in cloudiness and snowcover (Kattel et al. 2013; Kattel et al. 2015). Based on the seasonal and diurnal lapse rates patterns observed by Heynen et al. (2016), we chose to force the model with a fixed lapse rate for each particular hour of each month, which are referred to as monthly average hourly lapse rates henceforth, and comes down to 288 lapse rates (24 hour for 12 months). To interpolate the lapse rates, the observed air temperatures were first aggregated to hourly values and then averaged for each particular hour of each month. To reduce bias, monthly averages were only taken into account when the station has more than 80% data coverage in that month. Additionaly, several studies suggest that the lapse rates in the catchment vary spatially due to differences in aspect, shading, snow cover, proximity to debris covered glaciers and moraines and valley and katabatic winds (e.g. Heynen et al. 2016; Steiner and Pellicciotti, 2016). Hence, spatial differences in air temperature lapse rates were analysed. The lapse rate deviation on debris covered glaciers is caused by warming up of the debris layer during the night and cooling down during the day (Steiner et al. 2016). However, none of the meteorological stations are located on a debris covered glacier.

The hourly time-series at AWS Kyangjin was used to create spatial temperature fields. When data at AWS Kyangjin was missing, the record was first completed using the following priority of stations: AWS Yala BC, Pluvio Langshisha, Pluvio Yala or T-logger Kyangjin according to the previously determined lapse rates. Subsequently, hourly distributed temperature fields were created by extrapolating the time-series at AWS Kyangjin according to the determined lapse rates and a 100-m DEM.

2.3.2 Precipitation

High-elevation precipitation is the largest contributor to the hydrological water balance in the Himalaya (Bookhagen and Burbank, 2010) and is therefore an essential input to snow models in the region. The amount of precipitation is predominantly controlled by monsoon circulation and westerly winds (Whiteman, 2000). As a result, there is a strong seasonal variation in the amount of precipitation and spatial patterns (Immerzeel et al. 2014). Additionally, there is a diurnal precipitation variability during the monsoon, related to thermally driven regional and local valley winds (Collier and Immerzeel, 2015). During the monsoon, the peak values in the Langtang catchment are found around 3,000 m a.s.l., while during the winter, peak values are found above 5,000 m a.s.l. (Collier and Immerzeel, 2015). The spatial pattern in precipitation is mainly affected by the extreme relief, elevation, moisture availability and aspect (Whiteman, 2000). Consequently, the precipitation pattern in the Himalaya shows increasing south-north and east-west gradients, and locally gradients with a higher amount of precipitation at south-facing than north-facing slopes and a higher amount at the ridges than in the valleys (Bhatt and Nakamura, 2005; Anders et al. 2006). Since precipitation is a key input to hydrological models it is essential to have accurate spatially distributed precipitation forcing data. In fact, snow model outputs in the catchment are found to be highly sensitive to small changes in precipitation input (Stigter et al. 2017). However, the interaction and the different scale-dependent meteorological processes results in complex precipitation patterns with high spatial and seasonal variability, while high altitude observations are

scare. It is therefore not possible to establish uniform catchment-wide precipitations gradients (Immerzeel et al. 2014). Commonly used gridded precipitation datasets are also not suitable for high-resolution hydrological studies in regions with extreme topography due to their coarse resolution in comparison with the topography (Palazzi et al. 2013).

High-resolution atmospheric models can provide accurate precipitation forcing data, which can compensate for spatial and temporal gaps in observational networks and can be used as forcing data for hydrological models. The Weather Research and Forecasting (WRF) model (Skamarock and Klemp, 2008) is such a model and has successfully been used in several studies in the Himalaya, showing reasonable agreement with observations (e.g. Maussion et al. 2014; Bonekamp et al. 2018; Bonekamp et al. 2019; Collier and Immerzeel, 2015). Simulations with a one kilometer resolution WRF model provide a reasonable match with observations and a plausible spatial distribution of precipitation in the catchment (Bonekamp et al. 2018; Collier and Immerzeel, 2015). However, these models are still subjected to analysis and forecast errors and do not assimilate precipitation observations. Therefore, the spatial patterns that result from the WRF model can be used to scale observed station precipitation and provide more reliable precipitation patterns. In this study we use the WRF output of Bonekamp et al. (2019), which covers the period 2011-2013 with a spatial resolution of 1 km, and has proven to captures the spatial variability of both monsoon and winter precipitation (Bonekamp et al. 2018). 288 precipitation fields were available, one for each particular hour of each month. The WRF precipitation fields from were in the UTC time zone and were therefore converted to the Nepal time zone (UTC +5:45). This was done by shifting the time, followed by linear interpolation.

To account for the seasonal change in precipitation pattern, monthly WRF precipitation fields are used to scale the observed precipitation at AWS Kyangjin in the non-monsoon season. Since Collier and Immerzeel (2015) found that there is a diurnal precipitation variability during the monsoon, which is related to thermally driven regional and local valley winds, it is investigated in this study if there are sub-daily changes in spatial precipitation patterns during the monsoon. If so, these sub-daily monthly precipitation fields are used to scale the observed precipitation, and if not, the monthly precipitation fields are used. The WRF simulation outputs are first compared to observed precipitation at AWSs and Pluvios, and then used to scale the observed precipitation at AWS Kyangjin.

To compare the WRF output with observations, model data were taken from the closest grid point to each station without interpolation. For the comparison, observations from AWS Yala BC and Pluvio Langshisha, Pluvio Morimoto and Pluvio Yala were used (Table 1). To reduce bias, observations of a month were only taken into account when the station has more than 80% data coverage in that month. Based on available measurements, the observations of 2013 and 2014 were used. During the non-monsoon seasons observed precipitation were aggregated to monthly values and during the monsoon the observed precipitation were aggregated to hourly values and then averaged for each hour of each month.

Distorted wind flow around precipitation gauges leads to significant undercatch of precipitation (Sevruk et al. 1991). The magnitude of this effect varies with wind speed, the presence or absence of windshields, gauge design, and the size, phase and fall velocity of snowflakes or rain droplets (Colli et al. 2015; Wolff et al. 2013). Undercatch of rain can be as high as 10% and undercatch of snow can even exceed 50% (Ye et al. 2004; Wolff et al. 2015). In this study, we therefore use a correction functions to account for this undercatch. Several studies have quantified the amount of undercatch of precipitation (e.g. Kochendorfer et al. 2017; Thériault et al. 2012; Wolff et al. 2015).

In this study, we use the theoretical catch efficiency ratio calculated from Kochendorfer et al. (2017), which is derived from the results of the World Meteorological Organization Solid Precipitation Intercomparison Experiment. This correction function is calculated from a large precipitation dataset gathered from multiple climatic regions including mountainous areas and is thereby the most comprehensive evaluation of precipitation undercatch available. Moreover, in a study conducted in the catchment the function largely corrected the undercatch of solid precipitation (Kirkham et al. 2019). The catch efficiency (*CE; -*) is calculated as (Kochendorfer et al. 2017):

$$CE = e^{-a(U)(1-tan^{-1}(b(T_{air}))+c)} \tag{2}$$

where U is wind speed (m s^{-1}), T_{air} is the air temperature (°C), and *a*, *b* and *c* are empirical coefficients. At Pluvio Morimoto and Pluvio Yala no wind measurements were available, which meant we could therefore not correct those for undercatch.

Spatial precipitation input fields were created by scaling the hourly time-series at AWS Kyangjin with the WRF precipitation fields. For this, ratios were calculated between the closest grid point to AWS Kyangjin and the other grid points for each WRF precipitation fields, as follows:

$$R_{gp} = \frac{P_{gp}}{P_{AWS\ Kyangjin}} \tag{3}$$

in which P_{gp} (mm) is the precipitation at a certain grid point, $P_{AWS\ Kyangjin}$ is the precipitation at the grid point closest to AWS Kyangjin (mm) and R_{gp} is the ratio at that certain grid point. The resulting spatial precipitation ratio fields are used to scale the hourly time-series at AWS Kyangjin, which was done by multiplying the spatial precipitation ratio fields with the observed hourly precipitation. When data at AWS Kyangjin is missing, the record is first completed using the following priority of stations: AWS Yala BC, Pluvio Langshisha, Pluvio Yala or Pluvio Morimoto according to the previously calculated WRF ratio fields.

2.3.3 Incoming shortwave radiation

Incoming shortwave radiation is the most important energy input in high elevation catchments at low latitudes (Litt et al. 2019). It has a pronounced diurnal and annual cycle and the topographic shading, aspect and slope exert a strong control on the spatial and diurnal distribution of this radiation. Clear-sky incoming radiation can be calculated with GIS models without any meteorological input data, and therefore provides a valuable input for capturing the spatial variation in diurnal melt-refreeze cycles. Additionally, in low latitude, high-elevation mountainous regions, incoming shortwave radiation is an import driver of meltwater generation, since it causes substantial meltwater generation at temperatures close to the freezing point (Bookhagen and Burbank, 2010). The clear-sky incoming shortwave radiation is corrected for clouds with the WRF atmospheric transmissivity outputs of Bonekamp et al. (2019). The corrected incoming shortwave radiation is compared to observations at AWSs in the catchment.

The ArcGIS Points Solar Radiation tool was used to calculate the clear-sky incoming shortwave radiation. This tool calculates insolation for specific locations, based on methods from hemispherical viewshed algorithm (Fu and Rich, 2002). The model accounts for the aspect, slope, shading due to surrounding topography and elevation. The model requires input of transmissivity and diffusion proportion. Since we corrected the clear-sky incoming shortwave radiation with transmissivity fields, the transmissivity was set to 1. The diffuse proportion is set to 0.3, the default

value for generally clear sky conditions. The model was run at a 100 m resolution for the year 2017 (a non-leap year) at an hourly time step based on a 90-m SRTM DEM.

To obtain atmospheric transmissivity fields, the ratios between the monthly average hourly shortwave radiation received at the top of the atmosphere and the shortwave radiation received at the earth's surface, a measure of atmospheric transmissivity determined by cloud attenuation, was calculated from the WRF output. Since clear-sky incoming shortwave radiation has strong seasonal and diurnal pattern, the 2017 time-series of hourly incoming shortwave radiation was averaged to monthly average hourly values. Since cloud cover also has strong seasonal and diurnal patterns, we used the monthly average hourly atmospheric transmissivity outputs (e.g. Karki et al. 2019). To obtain net hourly incoming shortwave radiation, the clear-sky incoming shortwave radiation was multiplied with the atmospheric transmissivity ratios.

To compare the model output with observations, model data were taken from the closest grid point to each station without interpolation. For this, hourly observations from AWS Kyangjin, AWS Yala BC and AWS Yala Glacier were used and converted to monthly average hourly values. To reduce bias, monthly averages from a year were only considered when the station has more than 80% data coverage in that month.

It was investigated if it is suitable to scale the observed hourly shortwave radiation at AWS Kyangjin with ratio fields, as was done for the precipitation. When data at AWS Kyangjin is missing, the record is first completed using the following priority of stations: AWS Yala Glacier or AWS Yala BC according to the ratio fields. Ratio fields were calculated as in equation (3), for each monthly average hourly modelled field. The resulting spatial incoming shortwave radiation ratio fields are used to scale the hourly time-series at AWS Kyangjin, which was done by multiplying the spatial incoming shortwave radiation ratio fields with the observed incoming shortwave radiation.

2.4   Modified seNorge snow model

2.4.1   Model description

The seNorge snow model (Saloranta, 2012, 2014, 2016) is a single-layer temperature-index model, with a 100 m resolution, which takes as input forcing the daily average temperature and daily sum of precipitation. The model was originally developed for operational snow mapping in Norway, but recently, a high-mountain version (v.2) has been developed (Saloranta et al. 2019). The revised seNorge model (v.1.1.1) of Saloranta (2016) consists of a snowpack water balance module with a degree-day refreezing approach, and a snow compaction and density module. Stigter et al. (2017) improved the seNorge model of Saloranta (2016) by implementing albedo decay and avalanching. The model was also improved by implementing an enhanced temperature index melt algorithm and, therefore, includes the influence of incoming shortwave radiation on melt. The modified seNorge model of Stigter et al. (2017) was further improved by Saloranta et al. (2019) by implementing sublimation and evaporation, an improved parameterization of albedo decay, and a physically based parameterization of refreezing, and by running the model at a 3-hourly time step.

The seNorge model (v.2) was selected for this study since it has an physically based parametrization of refreezing, an enhanced temperature-index melt algorithm and it can be run at a sub-daily time step, which is needed to capture diurnal melt-refreeze cycles (Saloranta et al. 2019). An enhanced temperature-melt algorithm is most suitable, since distributed fields of air temperature, precipitation and shortwave radiation forcing data are available, while distributed fields of longwave radiation, wind, humidity and air pressure forcing data are not available. As has been mentioned previously, enhanced temperature-index models outperform temperature-index

models in high elevation catchments at low latitude with sub-daily temporal resolution (Avanzi et al. 2016; Litt et al. 2019). Moreover, the seNorge model (v2.0) has been proven to perform well and has already been calibrated in the catchment, by assimilation of MODIS snow cover maps and snow depth measurements, using an Ensemble Kalman Filter scheme (Stigter et al. 2017).

We further improved the model by (i) running it at an hourly time step, and by improving the model forcing (ii) by using high-resolution WRF simulations of precipitation to scale precipitation observations, and (iii) by using high-resolution WRF simulations of atmospheric transmissivity to correct clear-sky incoming shortwave radiation.

The sublimation/evaporation module was excluded in this study, for simplicity, and since it contains large uncertainties. However, excluding the sublimation and evaporation module results only in a 6% increase in non-monsoon melt runoff (Saloranta et al. 2019). Excluding sublimation and evaporation affects the SWE distribution significantly, with especially more SWE above 5,500 m a.s.l. (Saloranta et al. 2019), which limits the model performance. Reliable parameterizations of sublimation and evaporation, require spatial fields of wind speed, actual vapor pressure and surface temperature (Stigter et al. 2018), which entails surface energy balance modelling. For simplicity and due to uncertainties, the avalanching module was also excluded in this study. Excluding avalanching has no significant effect on the non-monsoon melt runoff (Saloranta et al. 2019). However, excluding avalanching also affects the SWE distribution significantly, with especially more SWE above 5,500 m a.s.l. and less SWE below 5,000 m a.s.l. (Saloranta et al. 2019), which limits the model performance. Since the model does also not account for wind-induced snow transport, there is no redistribution of snow from higher to lower elevation. In addition, we used the albedo decay function of Stigter et al. (2017) for simplicity. The use of the sophisticated albedo parametrization of Saloranta et al. (2019), which also includes solar angle, is beyond the scope of this research.

The modified seNorge model was rewritten in the environmental programming language, PCRaster Python (Karssenberg et al. 2001). PCRaster is an open source collection of software for the development and usage of spatio-temporal environmental models. Details about the model modules are described in the following sections and the model parameters used are shown in Table 3.

2.4.2 Accumulation, melt, refreezing and runoff

Precipitation (P; mm hour^{-1}) is separated in snow (P_s; mm hour^{-1}) and rain (P_r; mm hour^{-1}) by using the rain-snow temperature threshold (T_T; °C) as:

$$P_r = P, if\ T_a > T_T \tag{4}$$

$$P_s = P, if\ T_a \leq T_T \tag{5}$$

in which T_a is the air temperature (°C). The snowpack consists of a solid component (SWE_s; mm) and can retain liquid water from snowmelt and rain up to the maximum snow storage potential (r_{max}), which forms the liquid component (SWE_l; mm). The r_{max} is a fixed fraction of the SWE_s. When r_{max} is exceeded, the snowmelt or rain becomes runoff. The snowmelt simulation of the modified seNorge model is based on the enhanced temperature-index approach of Pellicciotti et al. (2005). When the T_a is higher than the threshold temperature for onset of melt (T_m; °C), the potential melt (M_{pot}; mm h^{-1}) of each grid cell is calculated as:

$$M_{pot} = T_a F_t + F_{sr} (1 - \alpha) R_{inc}, \ \ if \ T_a > T_m \tag{6}$$

where F_{sr} (m^2 mm W^{-2} h^{-1}) is the radiative melt factor, F_t (mm C^{-1} h^{-1}) is the temperature melt factor, α is the snow surface albedo and R_{inc} (Wm^{-2}) is the incoming shortwave radiation. Negative potential melt rates are set to zero. The calculation of α is described in the following section. The actual melt (M_a; mm) is restricted by the SWE_s as follows:

$$M_a \Delta t = \min(M_{pot} \Delta t, SWE_s), if \ T_a > T_m \tag{7}$$

where Δt is the length of the time step (h). When the T_a is below the threshold temperature for onset of melt (T_m; °C) and M_{pot} and P_{rain} are zero, the liquid component of the snowpack can refreeze. The refreezing module is based on Stefan's Law (Stefan, 1891), which is a basic analytic method describing the liquid-solid phase changes during the growth of sea-ice when seawater refreezes at the bottom of sea-ice. The model describes the conduction of latent heat that is released by the ice formation at the bottom and uses the surface temperature as a function of time and a

TABLE 3 | Parameters in the snow model

Parameter	Description	Value	Unit
Accumulation, melt and refreezing			
T_T	Rain-snow temperature threshold	0[a]	(°C)
r_{max}	Maximum snow storage potential	0.1[b]	
T_m	Threshold temperature for onset of melt	0[a]	(°C)
F_{sr}	Radiative melt factor	0.00625[a]	(m^2 mm W^{-2} h^{-1})
F_t	Temperature melt factor	0.18[a]	(mm C^{-1} h^{-1})
Albedo decay			
S_{reset}	Minimum snowfall to reset albedo	1[a]	(mm d^{-1})
α_{max}	Maximum value of albedo of fresh snow	0.85[a]	(-)
α_{ini}	Decay of albedo parameter for deep snow	0.713[c]	(-)
α_1	Decay of albedo parameter for deep snow	0.112[c]	(-)
α_u	Albedo of surface underlying ice/ground	0.25/0.15[c]	(-)
α_2	Decay of albedo parameter for shallow snow	0.442[c]	(-)
α_3	Decay of albedo parameter for shallow snow	0.058[c]	(-)
$d*$	Scaling length for transition albedo from deep to shallow snow	2.4[c]	(cm)
Compaction and density			
ρ_{min}	Minimum density of new snow	0.05[b]	(kg L^{-1})
α_{ns}	Snow density parameter	100[b]	
η_0	Initial viscosity	7.6[b]	(MN s m^{-2})
C_5	Viscosity parameter	0.1[b]	(°C^{-1})
C_6	Viscosity parameter	21[b]	(°C^{-1})
K_{comp}	Compaction factor	0.5[b]	(-)
g	Gravitation constant	9.81	(m s^{-2})

[a] Ragettli et al. (2015). [b] Saloranta (2014). [c] Brock et al. (2000).

fixed bottom temperature at freezing point as the boundary conditions. Since the model ignores thermal inertia, the ice temperature profile has a constant gradient in each layer (e.g. Lepparanta, 1983; Lepparanta, 1993). Besides this application, the model has recently also been used to model refreezing of liquid water retained in snowpacks (Saloranta et al. 2019). The temperature at the snow-ground interface is assumed to remain 0°C, as a result of the thermal insulation effect of the snowpack. T_a is assumed as the driving force of the cooling of the snowpack at the snow-atmosphere interface and is assumed to be equal to the temperature of the top of the snowpack. So, the snowpack is cooled from the snow-atmosphere interface in downward direction. During this cooling, all the liquid water is assumed to refreeze, thereby forming a refreezing front that penetrates downwards, during which latent heat is released. The temperature throughout the wet snowpack below the refreezing front is assumed to remain 0°C and the temperature gradient of the refreezing front is assumed to be constant. The liquid water is assumed to be evenly distributed over the wet part of the snowpack. An overview of the processes described above is shown in Figure 3 and the associated model formulation is described below. The depth of the refreezing front (z_{rf}; mm) is calculated as (Figure 3, time step 1):

$$z_{rf} = \sqrt{(z_{rf}{}^{t-1})^2 + \frac{2\kappa_s}{\rho_{lw}L}(-T_a)\Delta t_s} \cdot 1000 \qquad (8)$$

in which $z_{rf}{}^{t-1}$ (mm) is the depth of the refreezing front at the previous time step, κ_s is the thermal conductivity of snow (W m^{-1} K^{-1}), ρ_{lw} is the partial density of the liquid water in the snowpack (kg m^{-3}), which is calculated as in equation (35), L is the latent heat of fusion (J kg^{-1}) and Δt_s is the
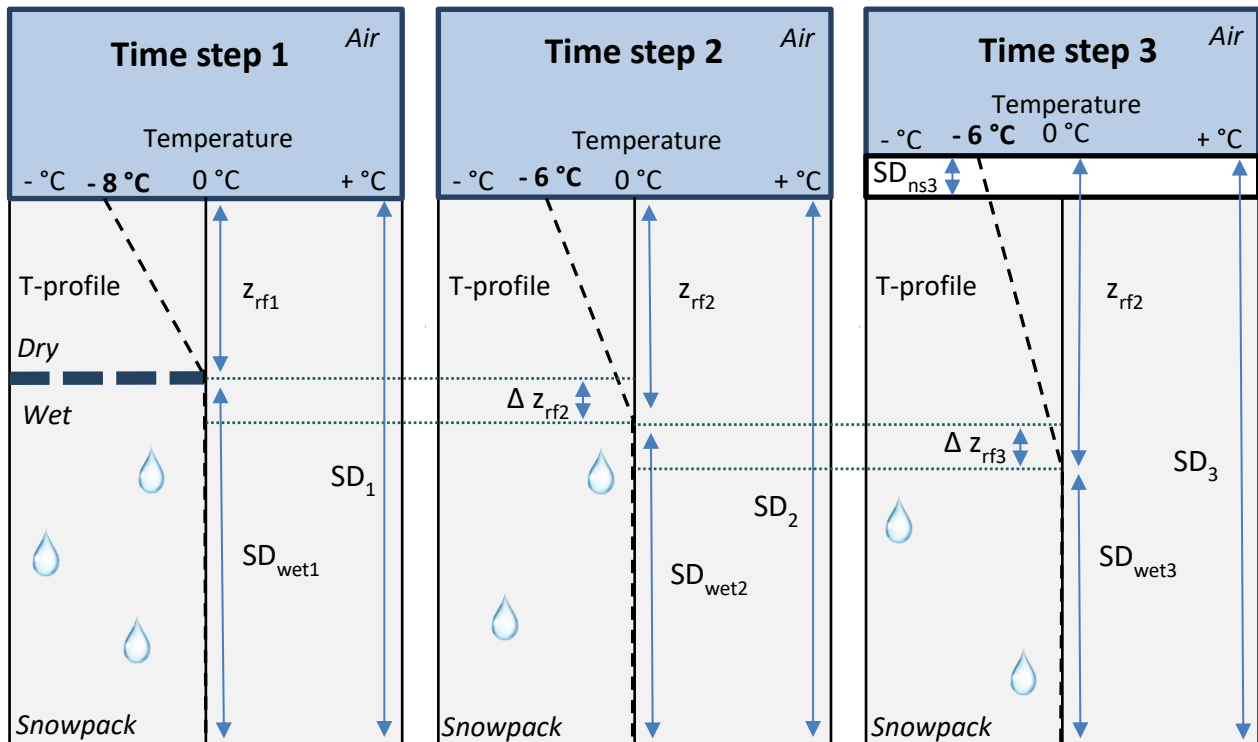
FIGURE 3 | Schematic diagram illustrating the refreezing module based on "Stefan's Law". Example with three successive time steps of the temperature profile (*T*-profile), refreezing front (z_{rf}), wet snow depth (SD_{wet}), new snow depth (SD_{ns}) and snow depth (SD) with changing air temperature and snowfall. Time step (1): T_a of -8°C and initial refreezing front (z_{rf1}). Timestep (2): T_a of -6°C results in growth of refreezing front (Δz_{rf2}). Timestep (3): T_a of -6°C results in growth of refreezing front (Δz_{rf3}) and snowfall results in growth of refreezing front and snow depth (SD_{ns3}).

length of the time step (s). κ_s is formulated with the empirical parameterization of Yen (1981), since it only requires snow density, as follows:

$$\kappa_s = 2.22362 \cdot \rho_s{}^{1.885} \tag{9}$$

where ρ_s (kg L-1) is the density of the solid snow, which is calculated as in equation (32) of the compaction module. The increase in refreezing front due to refreezing (Δz_{rf}; mm) is formulated as (Figure 3, time step 2):

$$\Delta z_{rf} = z_{rf} - z_{rf}{}^{t-1} \tag{10}$$

The amount of meltwater refreezing (R_{rf}; mm) as the refreezing front penetrates downwards is calculated as:

$$R_{rf} = \Delta z_{rf} \cdot \frac{SWE_l}{SD_{wet}} \tag{11}$$

SD_{wet} is the depth of the wet part of the snowpack, which is formulated as in equation (34). When melt or rain occurs, z_{rf} is set to zero. When snowfall occurs, the temperature of the new part of the snowpack is set equal to T_a. This snow depth is added to the refreezing front, but contains no liquid water, so there is no refreezing with this increase of the refreezing front. As the temperature of the new part of the snowpack is assumed to be equal to T_a, the Δz_{rf} is independent of snowfall. To calculate the change in snow depth due to snowfall the density of the newly fallen snow is needed, which is calculated as (Bras, 1990):

$$\rho_{ns} = \rho_{min+}(\frac{\max{(T_{fahr},0)}}{\alpha_{ns}})^2 \tag{12}$$

where ρ_{min} is the minimum snow density of fresh snow, T_{fahr} is the air temperature (°F) and α_{ns} an empirical coefficient. So, below 0°F, which is -17.8°C, the snow density of fresh snow is at its minimum. The change in SD due to snowfall (SD_{ns}) is defined as:

$$SD_{ns} = \frac{P_s}{\rho_{ns}} \tag{13}$$

The z_{rf} after snowfall is formulated as (Figure 3, time step 3):

$$z_{rf} = z_{rf} + SD_{ns} \tag{14}$$

The resulting SWE_s after the melt and refreezing is calculated as follows:

$$SWE_s = SWE_s - M_a + R_{rf} \tag{15}$$

As mentioned above, when the snow storage potential is exceeded, the snowmelt or rain becomes runoff. Since this study focusses on snow processes, it is important to separate runoff in rain runoff and snow runoff. When rain and melt occur simultaneously it is assumed that the rain saturates the snowpack first. The rain runoff (Q_r; mm) is calculated as:

$$Q_r = \max(P_r - (r_{max} \cdot SWE_s - SWE_l - M_a\Delta t), 0) \tag{16}$$

The melt runoff (Q_m; mm) is calculated as:

$$Q_m = \max(M_a\Delta t - (r_{max} \cdot SWE_s - SWE_l), 0) \tag{17}$$

Rain falling on snow free surfaces is directly converted to rain runoff. To calculate the resulting SWE_l, first the potential liquid component of the snowpack (SWE_{lp}; mm) is needed, which is formulated as:

$$SWE_{lp} = SWE_l + P_r + M_a \Delta t - R_{rf} \tag{18}$$

The amount of SWE_l is then formulated as follows:

$$SWE_l = \min (SWE_{lp}, r_{max} \cdot SWE_i) \tag{19}$$

The SWE is defined as:

$$SWE = SWE_i + SWE_l \tag{20}$$

2.4.3 Albedo decay

Since shortwave radiation is the main energy input in high elevation catchments (Litt et al. 2019), albedo is an important input to snow models. The snow surface albedo (α) is calculated with an albedo decay algorithm adapted from Brock et al. (2000). The albedo decay algorithm is based on cumulative daily maximum temperature since snowfall (T_{cm}; °C). A minimum amount of snowfall (S_{reset}) is needed to reset the snow albedo to the maximum albedo of fresh snow (α_{max}). The results of Brock et al. (2000) show that the albedo decays rapidly for fresh snow and more gradual and sustained for older snow. The albedo decay is therefore calculated with a logarithmic function for deep snow ($\geq$5 mm SWE). To enable albedo to decay to the underlying ice, debris or substrate albedo the albedo decay is calculated with an exponential function for shallow snow (<5 mm SWE) (Figure 3). The albedo decay for deep snow ($\geq$5 mm SWE) (α_{ds}) is formulated as:

$$\alpha_{ds} = \alpha_{ini} - \alpha_1 \cdot log_{10}(T_{cm}) \tag{21}$$

where α_{ini} and α_1 are empirical coefficients. The albedo decay for shallow snow (<5 mm SWE) (α_{ds}) is formulated as:

$$\alpha_{ss} = \alpha_u - \alpha_2 \cdot e^{(-\alpha_3 T_{cm})} \tag{22}$$

where α_u, α_3 and α_2 are empirical coefficients. There is a discontinuity between equation (21) and equation (22), this is overcome through a transition from α_{ds} to α_{ss} as a function of decreasing SWE:
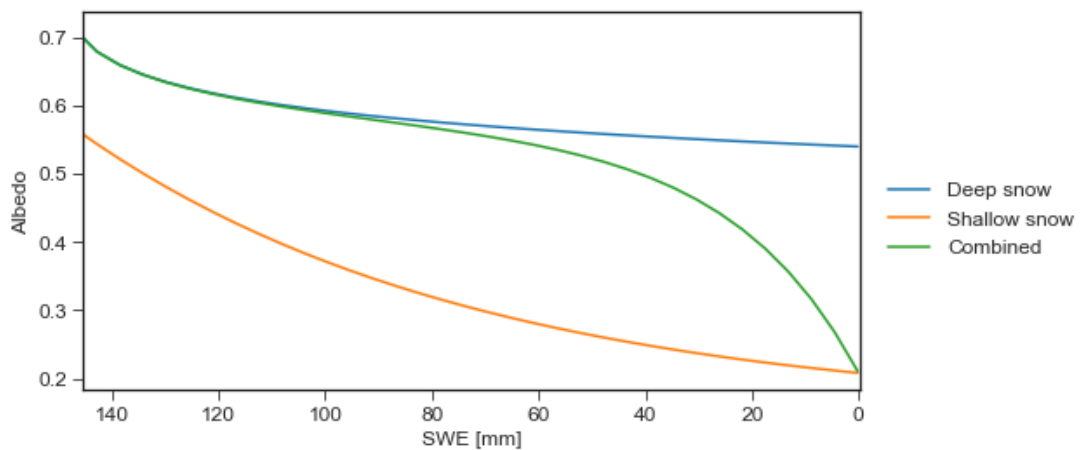

FIGURE 4 | Albedo decay functions for deep snow (equation 21), shallow snow (equation 22) and combined (equation 23). This example depicts a continuous 4.32 mm SWE decrease for each °C T_{cm}.

$$\alpha = (1 - e^{\frac{-SWE}{d*}}) \cdot \alpha_{ds} + e^{\frac{-SWE}{d*}} \cdot \alpha_{ss} \tag{23}$$

where $d*$ (cm) is the scaling length for the *SWE*. The scaling length has as a result that below a *SWE* of 5 cm, both α_{ss} and α_{ds} influence α, which prevents the discontinuity. When the *SWE* is higher than 5 cm, α_{ss} has negligible influence on α and when the *SWE* is lower than 1 cm α is dominated by α_{ss}. An example of this transition with increasing T_{cm} and decreasing *SWE* is shown in Figure 4.

2.4.4 Compaction

The snowpack depth (*SD*; mm) and snow density (ρ; kg L^{-1}) are calculated with the snowpack compaction and density module of Alfnes (2008). The module calculates changes in *SD* due to snowmelt, new snowfall and viscous compaction. The change in *SD* due to snowmelt (ΔSD_{sm}; mm) is calculated firstly as:

$$\Delta SD_{sm} = \frac{M_{act} \cdot SD^{t-1}}{SWE_s{}^{t-1}} \tag{24}$$

The change in *SD* due to snowfall (*SD*$_{ns}$; mm) is calculated as in equation (13), in which the P_s cannot exceed *SWE*$_s$, to account for melt. The resulting snow depth after snowmelt and snowfall is defined as:

$$SD_1 = SD^{t-1} + \Delta SD_{sm} + SD_{ns} \tag{25}$$

After this, the decrease of *SD* due to gradual compaction (ΔSD_{comp}) is calculated. In the compaction module the amount of liquid water in the snowpack is defined as the amount of water that actually passes the snowpack (*SWE*$_{cl}$) defined as:

$$SWE_{cl} = \max (SWE_l, \ V_{pore}) \tag{26}$$

$$V_{pore} = SD_1 - 1.1 \ SWE_{ice} \tag{27}$$

in which V_{pore} is the pore volume of the snowpack (mm). For the compaction it is assumed that snow behaves as a viscous medium (e.g. Yen, 1981; Armstrong and Brun, 2008) and the viscosity (η; Ns m^{-2}) is determined as in the Crocus model (Vionnet, et al. 2012):

$$\eta = \frac{1}{1+60 \cdot \frac{SWE_{cl}}{SD_1}} \frac{\rho_{ns}}{0.250} \cdot \eta_o \cdot e^{-C_5 \cdot T_{snow} + C_6 \cdot \rho_{ns}} \tag{28}$$

where η_0 is the initial viscosity (MN sm^{-2}) and C_5, C_6, 0.250 and 60 are empirical coefficients. T_{snow} is assumed to be half of the negative air temperature and zero when the air temperature is above zero, since it is assumed that the gradient of the temperature profile in the snowpack is constant. The ΔSD_{comp} is eventually calculated as:

$$\Delta SD_{comp} = -\frac{k_{comp} \cdot g \cdot SWE}{\eta} \cdot SD \cdot \Delta t \tag{29}$$

where K_{comp} is a coefficient of 0.5 indicating that half of the snow mass is used for calculating gravitational snow compaction, g is the gravitation constant (ms^{-2}) and Δt is the time step (s). Finally, the snow depth and the snow density are defined as:

$$SD = SD_1 + \Delta SD_{comp} \tag{30}$$

$$\rho = \frac{SWE}{SD} \tag{31}$$

The ρ_s is calculated as:

$$\rho_s = \frac{SWE_s}{SD} \tag{32}$$

The z_{rf} is formulated as:

$$z_{rf} = z_{rf} \cdot \frac{SD}{SD_1} \tag{33}$$

SD_{wet} is formulated as:

$$SD_{wet} = SD - z_{rf} \tag{34}$$

The ρ_{lw} is formulated as:

$$\rho_{lw} = \frac{SWE_{liq}}{SD_{wet}} \tag{35}$$

2.4.5   Model setup

The model was run from July 2012 to June 2014 and from July 2016 to June 2018 based on available measurements covering full hydrological years. There is a substantial data gap in 2015 due to the Gorkha earthquake, when almost every station got damaged. The model runs begin around the snow minimum of the catchment (Immerzeel et al. 2009) and cover a period of exactly four hydrological years. To simulate initial SWE_s, SWE_l, SD, z_{rf} and α, the model was first run for a spin-up period of one year from July 2012 to June 2013. The SWE_s, SWE_l, SD, z_{rf} and α of the final time step of first part of the run (July 2012-June 2014) were used as initial conditions for the second part of the run (July 2016-June 2018), which allowed the model to be run continuously. As mentioned previously, the model was run at an hourly time step to account for the high diurnal variability of air temperature, which is needed to capture the diurnal melt-refreezing cycle. To examine the importance of an hourly time step, model experiments with an hourly and a daily timestep were conducted, including the spin-up year. Additionally, to study the impact of refreezing, model experiments with and without refreezing were conducted, including the spin-up year.

2.5   Validation

To get a confirmation about the model performance the model outputs are validated against MODIS, snow depth and SWE observations. For the validation, we also ran the model with the simple degree-day refreezing approach of Stigter et al. (2017), since that model has been calibrated in the catchment. The model was run at an hourly and daily timestep for both the simple degree-day and the improved refreezing approach, to investigate the model performance.

2.5.1   MOYDGL06 snow cover fraction

The model outputs were validated with the combined Terra/Aqua MODIS snow-cover and RG6.0 glacier product called the MOYDGL06, which has been developed for High Mountain Asia for the period between 2002 and 2018 (Muhammad and Thapa, 2019). The Terra and Aqua satellite sensors image the same area on Earth approximately three hours apart every 1 to 2 days. The

MOYDGL06 snow product has a spatial resolution of 500 m and combines the Terra and Aqua 8-day maximum snow extent products (MOD10A2.006 and MYD10A2.006 respectively), thereby optimizing cloud-free surface viewings. A pixel is considered to be snow covered if a pixel is snow covered in both products. This reduces overestimations caused misclassification of cloud cover as snow, and sensor limitation. Cloudy pixels are converted to snow or no snow depending on the majority of the surrounding pixels. The product also classifies debris covered and debris-free ice surfaces by using RGI6.0 glacier boundaries. The product has improved the accuracy by 10% from 77% to 87% in comparison with the raw MODIS Aqua/Terra product.

In another study, the MOD10A2 product has been validated in the catchment against surface temperature, which is an indirect measurement of the presence of snow. The MOD10A2 classification accuracy was found to be 83.1%, with misclassifications mainly due to the extreme topography and clouds being classified as snow (Stigter et al. 2017). Especially during the monsoon MOD10A2 and MYD10A2 misclassify cloud cover as snow and therefore the monsoon season is excluded in this validation (Stigter et al. 2017; Kirkham et al. 2019). For the validation the snow cover fractions of the catchment of the MOYDGL06 and the model outputs were compared. The snow cover fraction of each MOYDGL06 image was calculated by dividing the amount of snow covered pixels by the total amount of pixels. For the model outputs, first the 8-day maximum snow extents were determined, after which the amount of snow covered pixels were divided by the total amount of pixels for each 8-day period.

2.5.2   *In situ snow depth and SWE measurements*
The model outputs are validated with in situ snow depth and SWE measurements. We measured snow depth at AWS Yala BC, Pluvio Yala and snow depth and SWE at Snow Station Yala (Figure 1b and Table 1). The model outputs and observations are compared for periods with a substantial snow depth and amount of SWE.

2.6   Climate sensitivity analysis
The sensitivity of refreezing to future climatic changes is unknown in the Himalaya. In order to study this sensitivity we performed multiple runs with changed air temperature and precipitation. In addition, various uncertainties related to the meteorological input exits. In order to characterize the performance of the model, it is therefore important to explore the sensitivity of the model to these uncertainties.

2.6.1   *Air temperature and precipitation sensitivity*
To study this sensitivity to climatic changes we performed multiple runs with changed air temperature and precipitation. The annual average air temperature in the Himalaya is expected to increase by about 2 °C by 2050, depending on the scenario used (Wu et al. 2017; Wester et al. 2019; Rangwala et al. 2020). However, projections for precipitation are less clear and show a large disagreement, between models and between scenarios. On average, studies expect an increase in precipitation of about 10% by 2050 (Wu et al. 2017; Wester et al. 2019; Rangwala et al. 2020). Temperature and precipitation changes are expected to differ throughout the year, with the highest increase in temperature in the winter and pre-monsoon, the highest precipitation increase in the monsoon, and some studies even project a decrease in winter precipitation (Wu et al. 2017; Rangwala et al. 2020).

Our aim is to test the sensitivity of the model to projected climate change within realistic bounds, to study how refreezing responds to these changes. Thus, the aim is not to project and quantify future climate change effects, which would require transient changes over a longer time span, such that the model is able to adjust (Kobierska et al. 2013), and including seasonality, which is both left for future work. Hence, we study the sensitivity of the model by changing the temperature and precipitation within realistic bounds of the average projections and also, and equally distributed over the seasons. Additionally, the aim is also to test the sensitivity to uncertainties related to meteorological input, and therefore we also include temperature and precipitation changes in opposite direction. It should be noted that, we did not quantify these uncertainties, however our aim is to explore how refreezing responds to these differences in input.

Four temperature experiments were carried out by changing the temperatures with -2°C, -1°C, + 1°C and +2°C. The precipitation experiments include four runs with changed the precipitation by -10%, -5%, +5% and +10%. For each run either temperature or precipitation was adjusted, while other inputs were kept unchanged. In addition, to explore how the refreezing responds to projected climate change we also performed an experiment in which both temperature and precipitation were changed simultaneously with a +2° C temperature increase and a +10% precipitation increase, both evenly distributed over the seasons.

2.6.2   *Incoming shortwave radiation sensitivity*

The resolution of the DEM used for the simulation of the clear-sky incoming shortwave radiation, has been found to have a strong effect on the outputs of the simulation, with generally increasing performance with increasing resolution (Hopkinson et al. 2010; Ruiz-Arias et al. 2009). To study the sensitivity of the snow model, also an experiment was conducted, where the snow model is forced with incoming shortwave radiation derived from a 500-m STRM DEM, instead of a 90-m STRM DEM.

3   RESULTS

3.1   Forcing data

3.1.1   Air temperature

The monthly average air temperatures are highly consistent over the years, especially for the months May-September (Figure 5). The slopes in Figure 5, which represent the lapse rates, are also quite consistent and linear, independent of the elevation, for every month. This suggest that the monthly lapse rates are spatially and inter-annually consistent. The hourly and monthly boxplots of lapse rates reveal a high seasonal and diurnal variability (Figure 6). The lapse rates are most shallow and constant during the monsoon and the night, while the lapse rates are steepest during the pre-monsoon season, indicating that the temperature differences across the catchment are largest. Figure 7 shows the monthly average hourly lapse rates for each year. This reveals that there is a seasonal pattern of the lapse rates diurnal variability. The monthly average hourly lapse rates are fairly consistent over the years with least variability for the months April-September (Figure 7). Since the lapse rates are consistent over the years and the seasonal and diurnal variability is high, the model is forced with monthly average hourly lapse rates. This also makes it possible to extrapolate observed temperatures for periods with insufficient observations to obtain reliable lapse rates.

The strong linearity in Figure 5 suggests that there are no substantial spatial differences in lapse rates, since this would result in deviating parts. Further analysis shows that separate lapse rates of the east and west part of the catchment are indeed similar. The combined lapse rates have
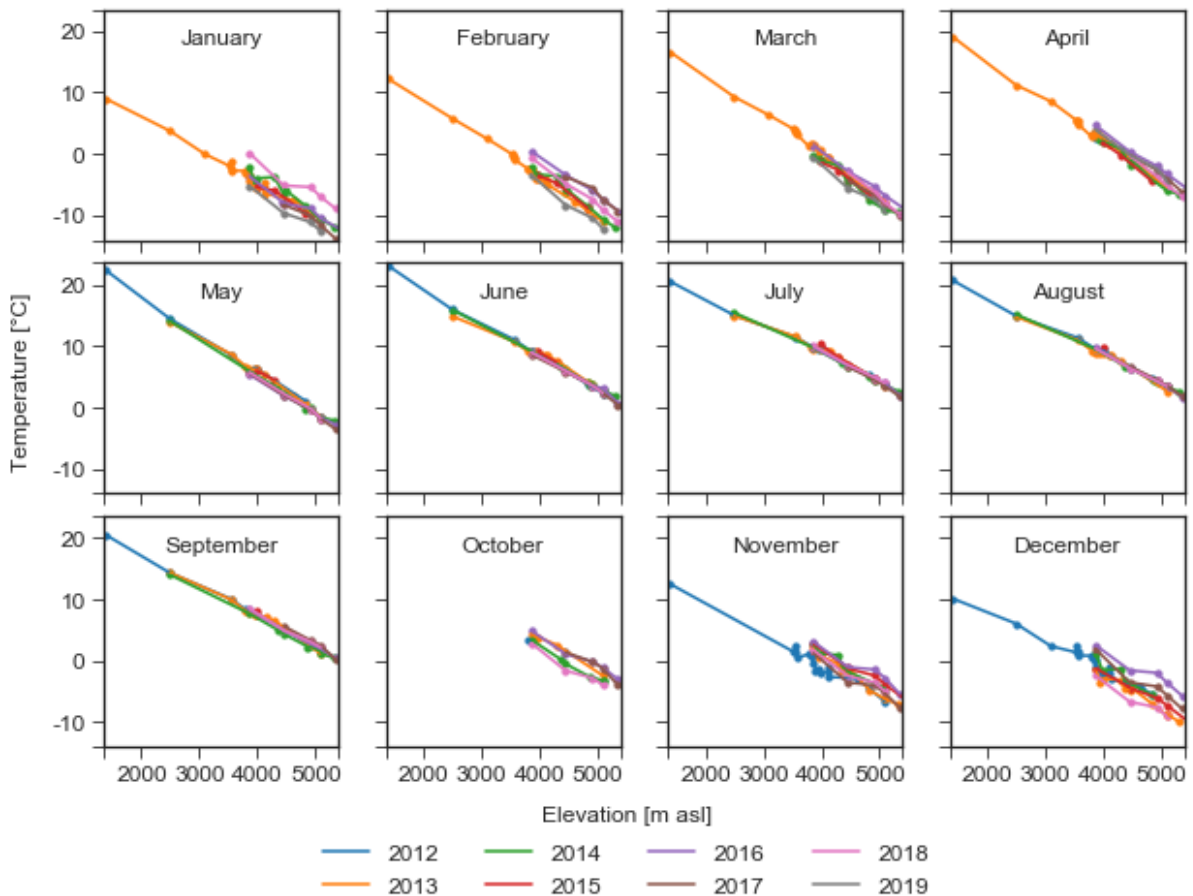

FIGURE 5 | Monthly average air temperature against elevation for all years. Trimmed to months which have more than 80% data coverage.
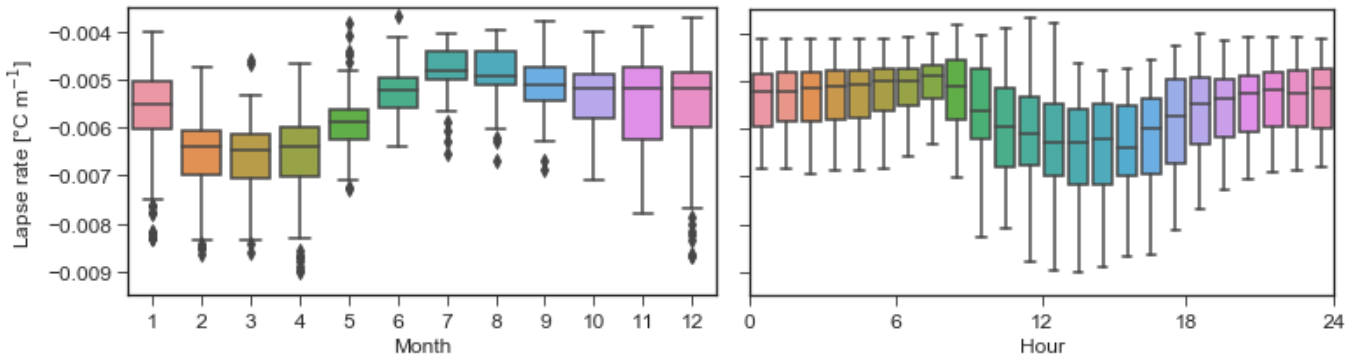
FIGURE 6 | Monthly and hourly boxplots of hourly lapse rates. Regressions have been trimmed to p <0.1, R-> 0.5 and number of observations > 3.

the highest R-squared values and lowest p values and we therefore use uniform lapse rates for the entire catchment.

Figure 8 shows the completed temperature time-series at AWS Kyangjin, including the station from which is extrapolated, when data was missing. There is a substantial data gap in 2015. The annual average temperatures are shown in Table 4. The time-series at AWS Kyangjin is used to extrapolate the temperature of the catchment according to the lapse rates. The previously determined monthly average hourly lapse rates and temperatures at AWS Kyangjin are shown in Figure 9. The lapse rates, especially in the monsoon and during the night, are highly linear with R-squared values close to one. The correlation of the lapse rates are lowest in the post-monsoon and during sunrise (Figure 9). The resulting monthly average temperature forcing data is shown in Figure 10.

FIGURE 7 | Monthly average hourly lapse rates. Regressions have been trimmed to p < 0.1 and number of observations > 3.
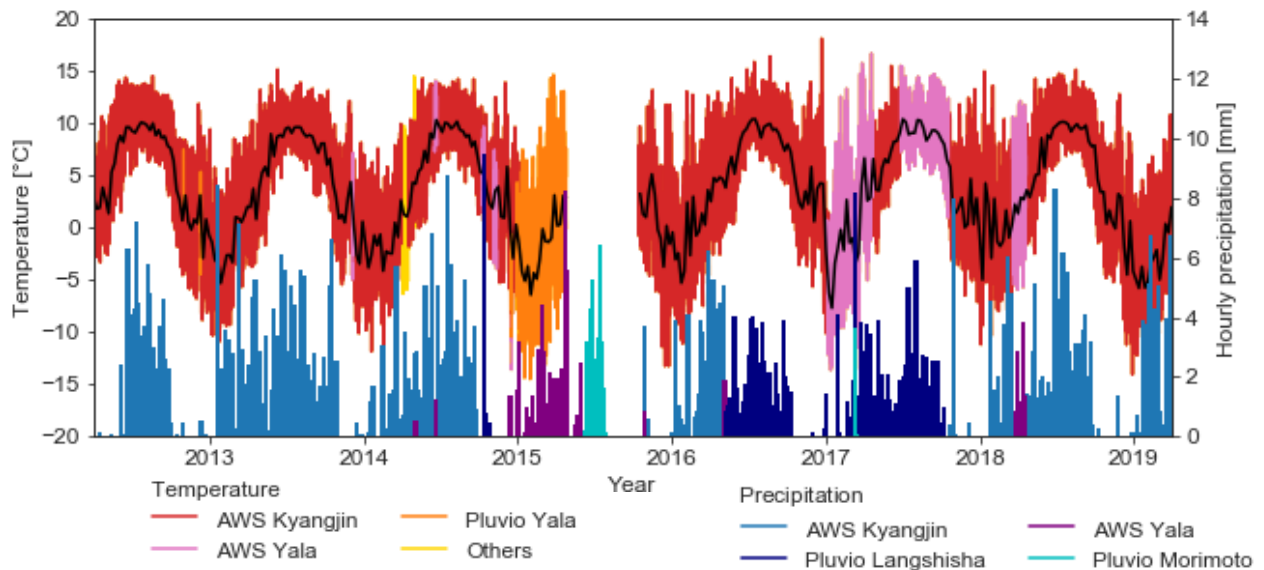
FIGURE 8 | Completed air temperature and precipitation hourly time-series at AWS Kyangjin, including the stations by which the time-series was completed. The black line indicates the average weekly air temperature.
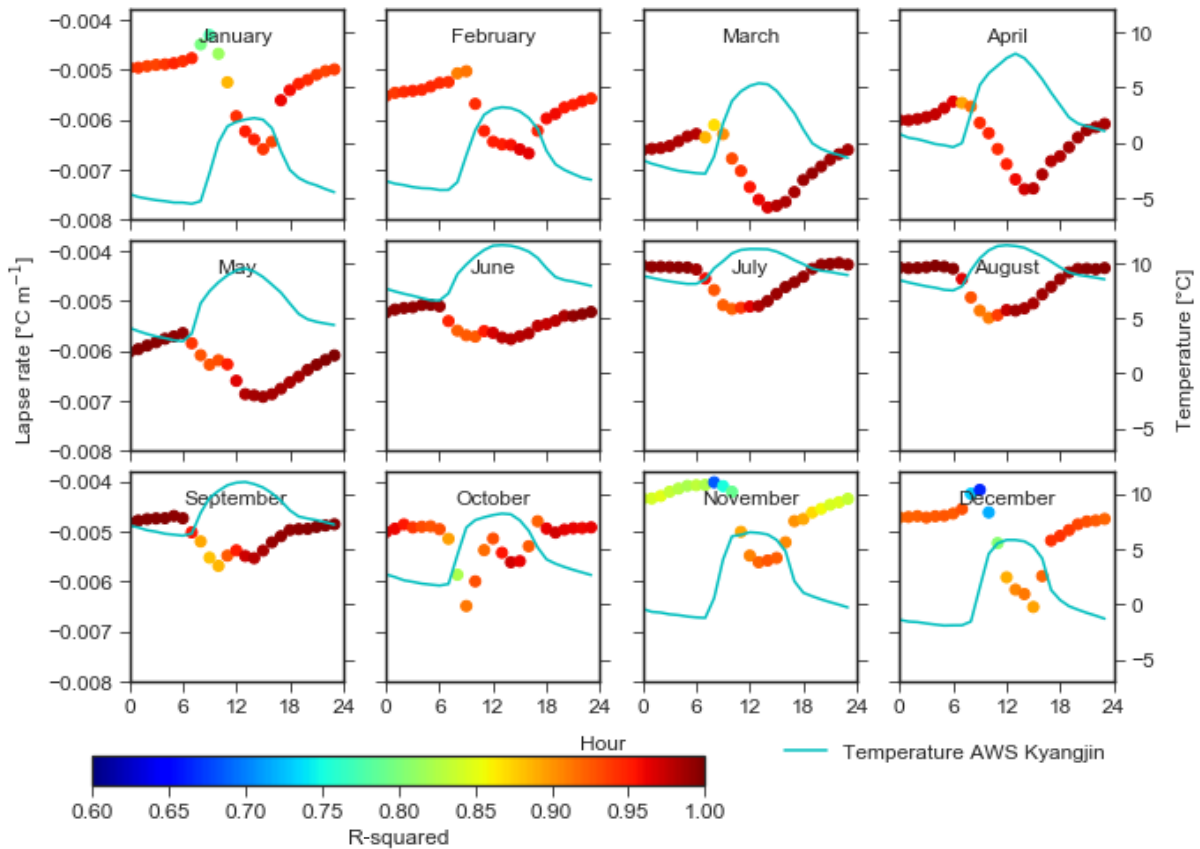
FIGURE 9 | Monthly average hourly lapse rates and air temperature at AWS Kyangjin.

TABLE 4 | Annual average air temperature and cumulative precipitation at AWS Kyangjin.

Hydrological year	Air temperature (°C)	Precipitation (mm)
2012-2013	3.8	979 mm
2013-2014	3.8	719 mm
2016-2017	4.4	694 mm
2017-2018	4.6	647 mm
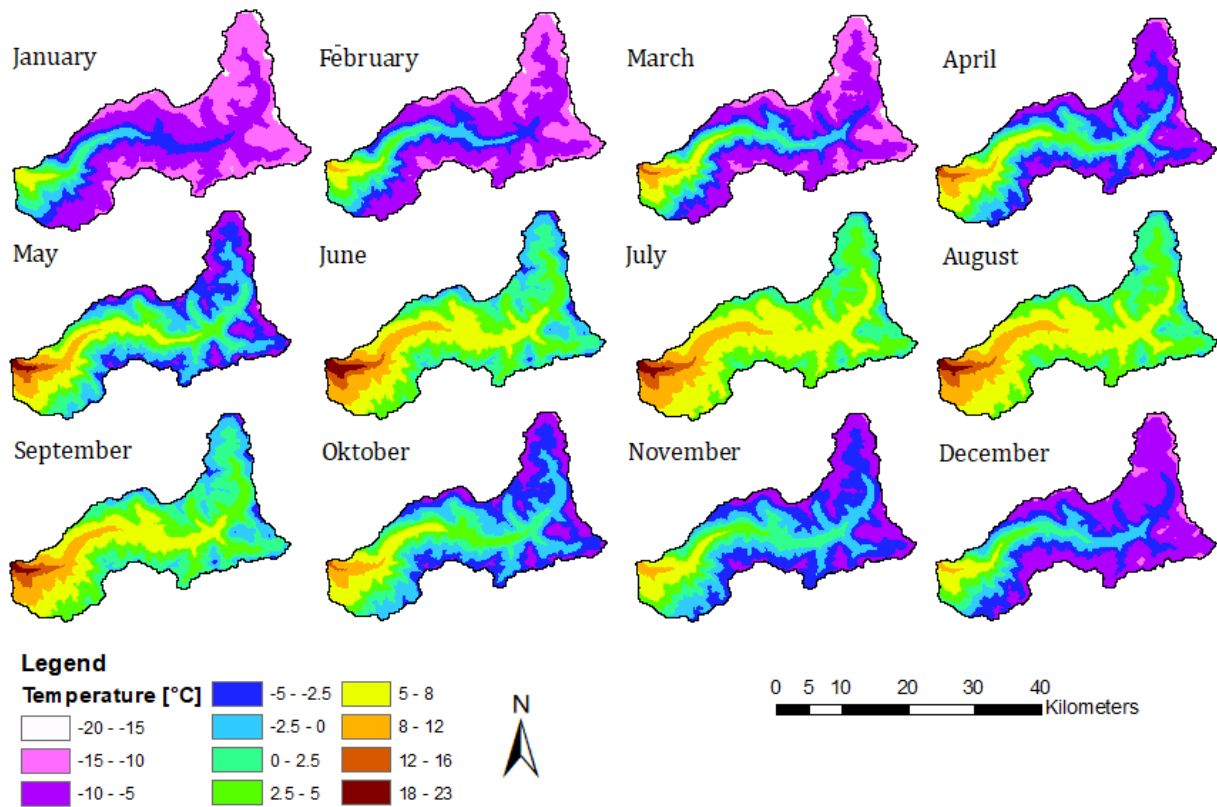
FIGURE 10 | Monthly average temperature.

In Figure 11 and 12 the diurnal temperature fluctuations around the freezing point are analysed, as these fluctuations are favourable for refreezing. Figure 11a,b,c show the number of days that the cumulative hourly temperatures above and below the freezing point are respectively 5, 10 and 20°C. The highest percentages are found between approximately 4,000 – 5,000 m a.s.l. (Figure 11e). A similar pattern is found for the average cumulative hourly temperatures of a day above and below the freezing point, with the highest values also found between 4,000 – 5,000 m a.s.l. (Figure 11d,e).

FIGURE 11 | Number of days that the cumulative hourly temperatures above and below the freezing point are **(a)** 5° C, **(b)** 10°C and **(c)** 20°. **(d)** The average cumulative hourly temperatures of a day both above and below the freezing point. **(e)** Figure a till d against elevation.

This is equal to the minimum of (i) the sum of all hourly temperatures of a day above the refreezing point and (ii) the sum of all hourly temperatures below the freezing point.

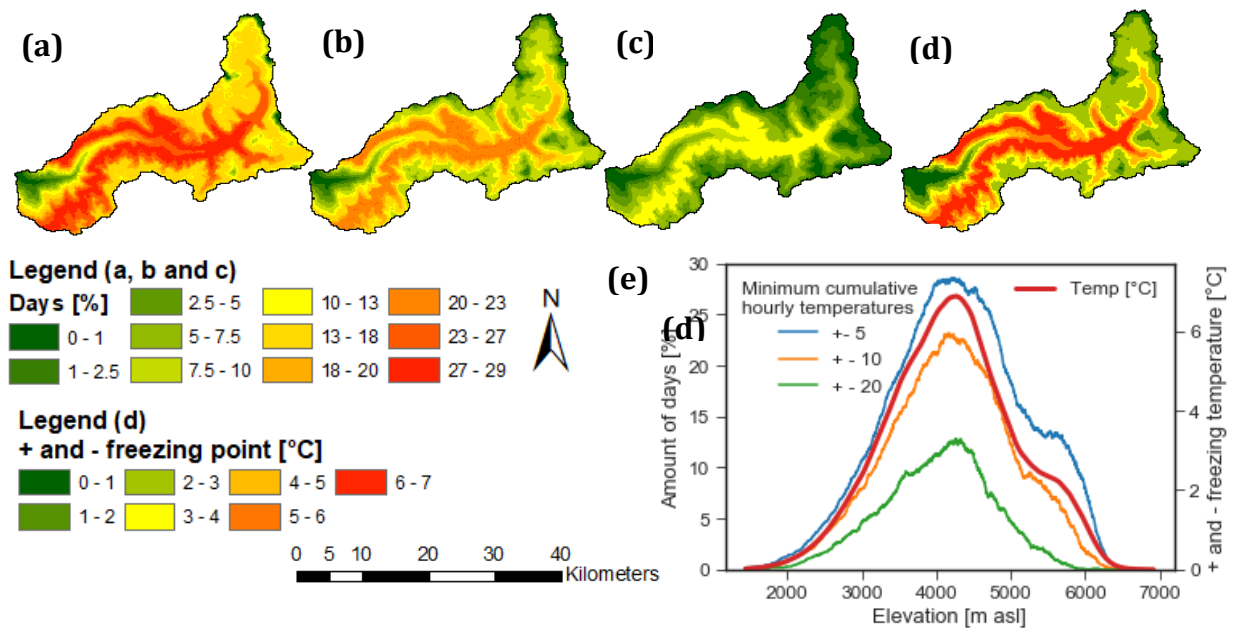Figure 12 reveals that the highest cumulative hourly temperatures of a day above and below the freezing point are found during the pre and post-monsoon seasons. During the winter season the highest values are found at low elevations, while in the post and pre-monsoon season the highest values are found at higher elevations (Figure 12). During the monsoon season the cumulative hourly temperatures of a day above and below the freezing point are generally low, which is caused by high and constant temperatures at AWS Kyangjin in combination with shallow constant lapse rates.
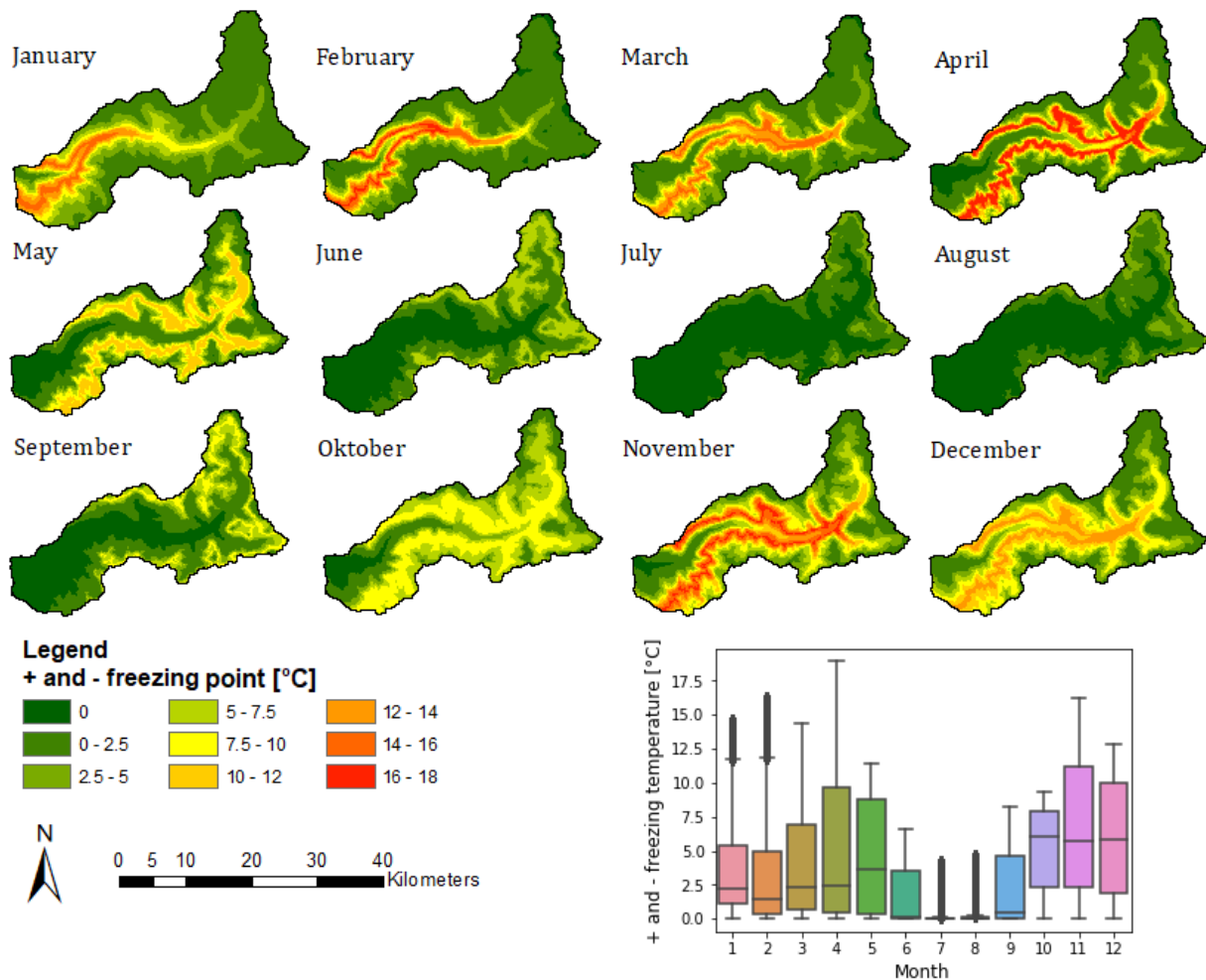
FIGURE 12 | The monthly average cumulative hourly temperatures of a day below and above the freezing point.

3.1.2 Precipitation

Figure 13 shows the monthly average precipitation outputs of the WRF simulations together with the monthly average precipitation recorded at the observation sites against elevation for 2013-2014. The amount of precipitation generally increases with elevation. However, the WRF output shows a small decline in precipitation at Pluvio Morimoto (4919 m a.s.l) in most months, which is located in the north eastern part of the catchment. This decline is also visible in the observational dataset in July. The model partly captures the seasonal variability with most precipitation during the monsoon and least in November and December. However, for the months January-May, and

FIGURE 13 | (a) Modelled and **(b)** observed average monthly precipitation against elevations for each station. The stations arranged from lower to higher elevation as: AWS Kyangjin, Pluvio Langshisha, Pluvio Yala, Pluvio Morimoto and AWS Yala BC. (a) and (b) both contain two views of the same graph.

especially in February, the model highly overestimates the precipitation at all sites. However, Pluvio Yala (4,813 m a.s.l.) and Pluvio Morimoto (4,919 m a.s.l.) are not corrected for undercatch, which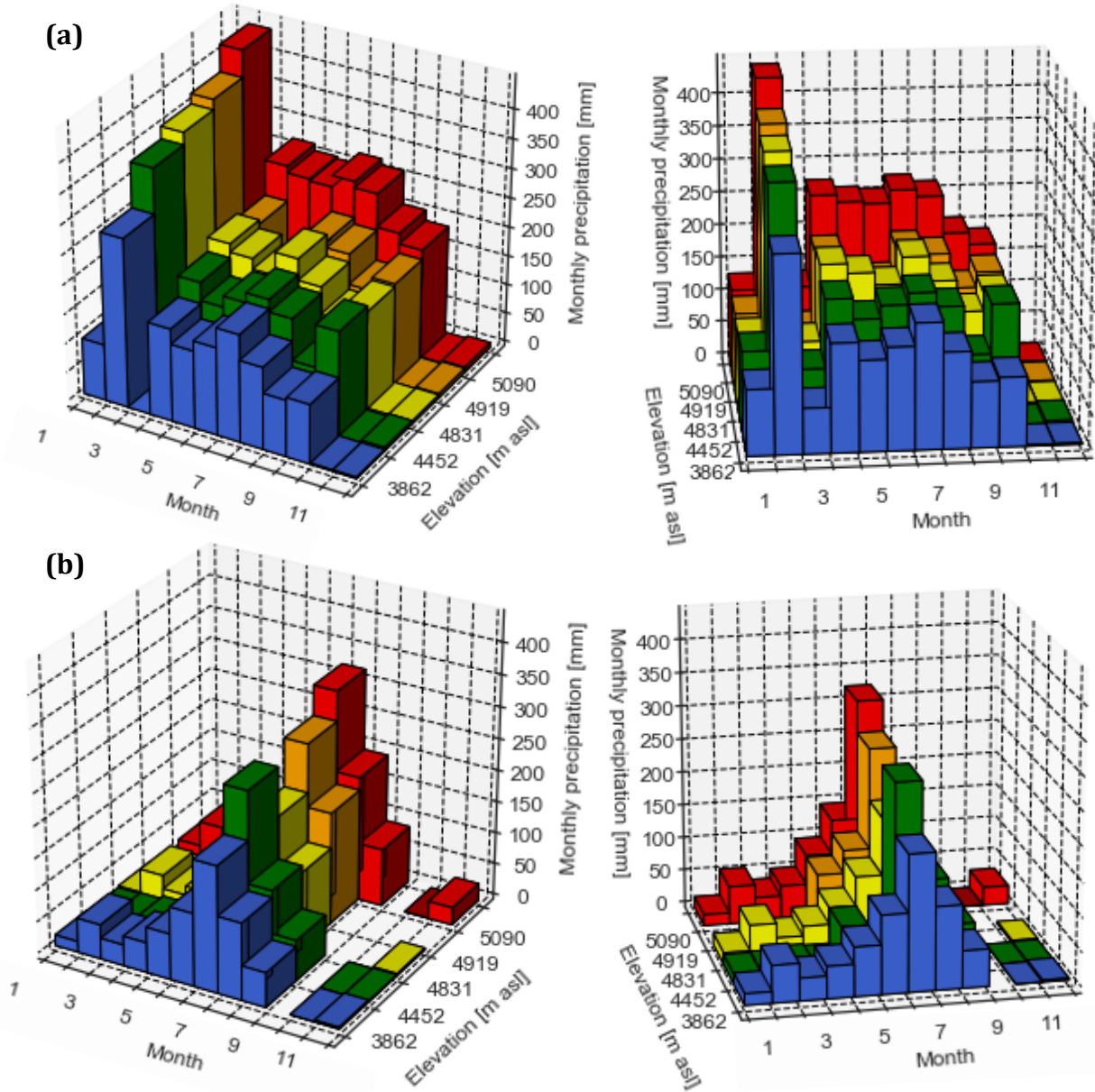 contributes to a certain extent to this disagreement. Moreover, the over- and underestimations of the amount of precipitation are generally similar for all sites (Figure 13). The disagreements between the precipitation ratios to Kyangjin, which are used to scale the observed precipitation, are therefore considerably lower (Figure 14a). The modelled ratios agree reasonably well with the observed ratios (RMSD = 0.34). For the comparison, values lower than 0.15 mm day^{-1} were filtered to avoid bias of extreme ratios with little precipitation.

During the monsoon, the model captures the diurnal cycle of precipitation reasonably well, with least precipitation from 06:00 to 12:00 (Figure 15). However, in particular for July, the model underestimates the amount of precipitation from 00:00 to 06:00, and in September, the model overestimates the amount of precipitation from 18:00 to 00:00. The over- and underestimations of

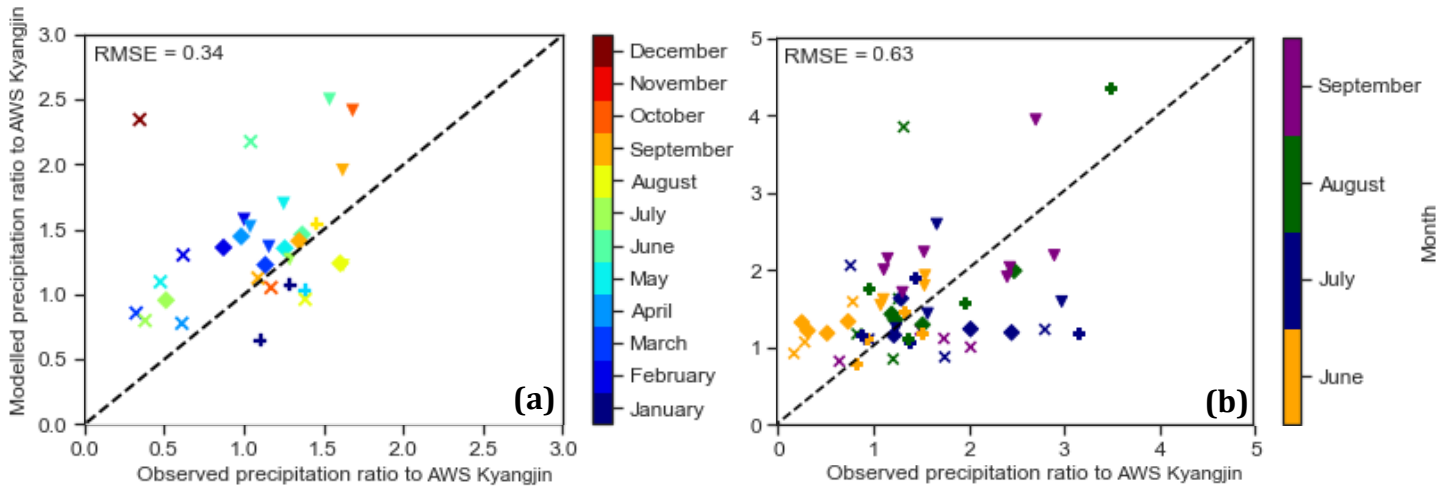**FIGURE 14 |** Modelled against observed precipitation ratio to AWS Kyangjin for **(a)** monthly average precipitation and **(b)** monthly average 6-hourly precipitation grouped by month. Crosses indicate Pluvio Langshisha, diamonds Pluvio Yala, triangles AWS Yala BC and circles Pluvio Morimoto.
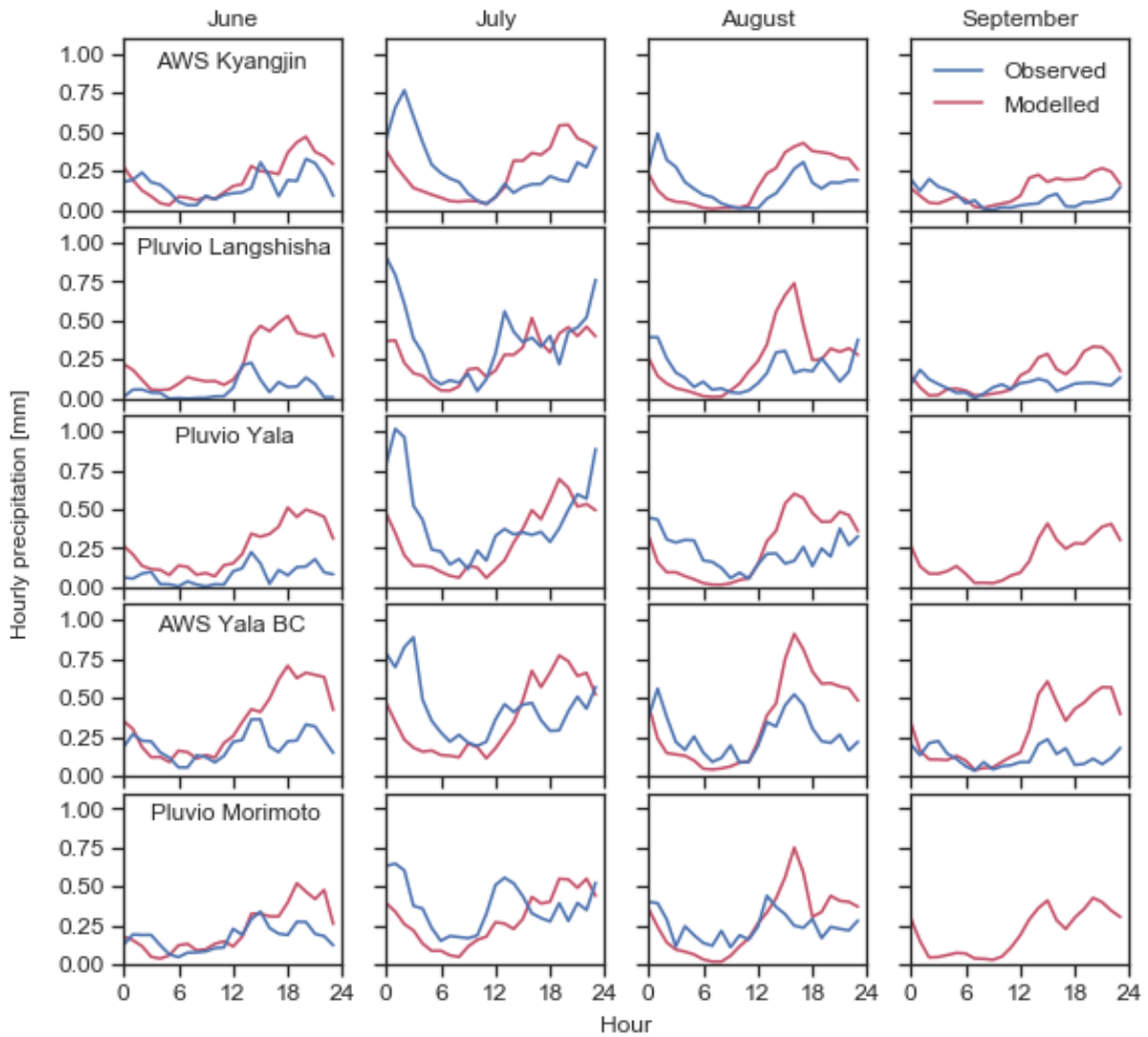

FIGURE 15 | Modelled and observed monthly average hourly precipitation at all sites during the monsoon season.

the amount of precipitation are again generally similar for all sites. The modelled ratios are therefore in better agreement with the observed ratios. Ratios of monthly precipitation fields are the best match with the observations (RMSE = 0.34) in comparison with hourly (RMSE = 0.95), 3-hourly (RMSE = 1.4) and 6-hourly (RMSE = 0.63), and therefore give the most plausible spatial distribution precipitation patterns. Figure 14b shows that there is indeed little agreement between the sub-daily modelled and observed ratios. Therefore, the monthly WRF ratios fields are used to scale the observed precipitation during the monsoon.

Figure 8 shows the completed precipitation time-series at AWS Kyangjin, including the station by which the time-series was completed, when data was missing. The annual average cumulative precipitation ranges from 647 mm to 979 mm (Table 4). Besides the before mentioned temperature data gap, there is also a large precipitation data gap in 2015. The scaled precipitation from Pluvio Langshisha has a lower intensity per hour, but the cumulative monthly values are similar. This time-series is scaled with monthly WRF precipitation ratios fields to create spatial precipitation input fields (Figure 16). The resulting monthly precipitation forcing data is shown in Figure 17. The mean annual catchment-wide precipitation is 1463 mm of which 431 mm (29%) falls as snow. 85% of the precipitation falls during the monsoon which consist out of 39% of the total snowfall and 96% of the total rainfall. Figure 18 reveals that most precipitation (62%) and snowfall (61%) occurs from 18:00 to 06:00.
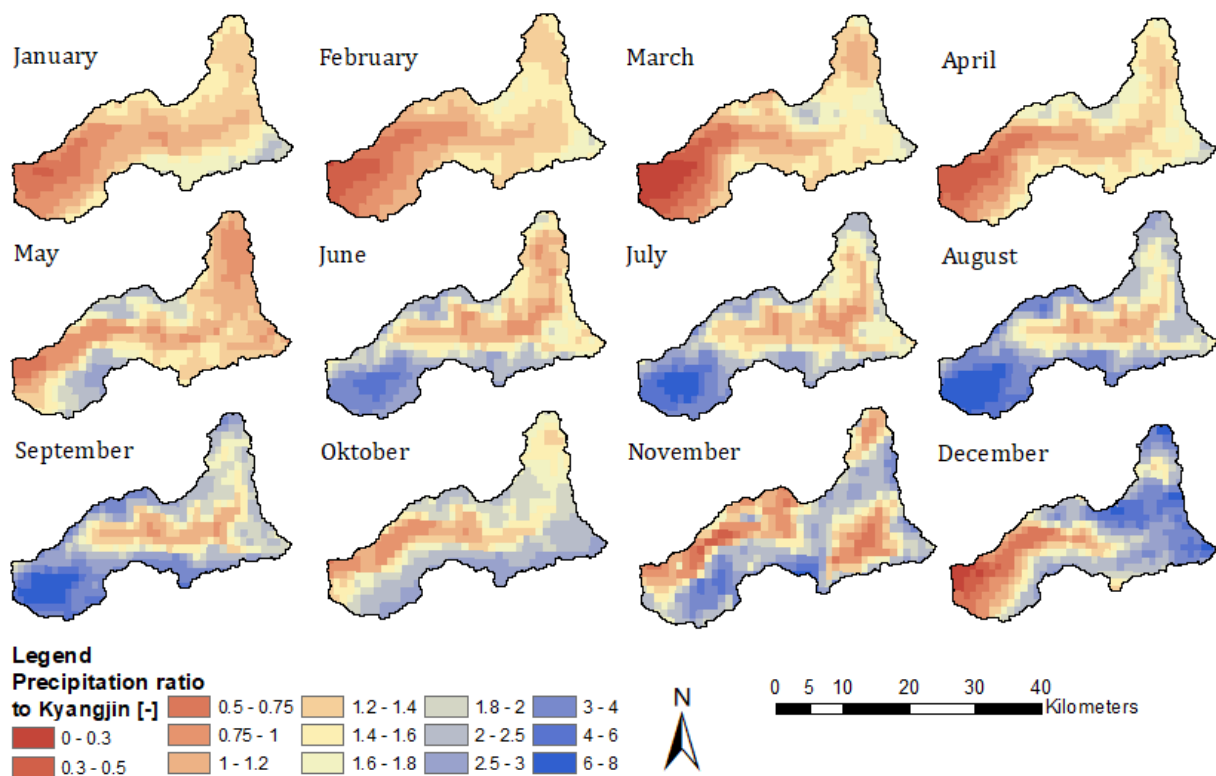
FIGURE 16 | Modelled monthly precipitation ratios to AWS Kyangjin.
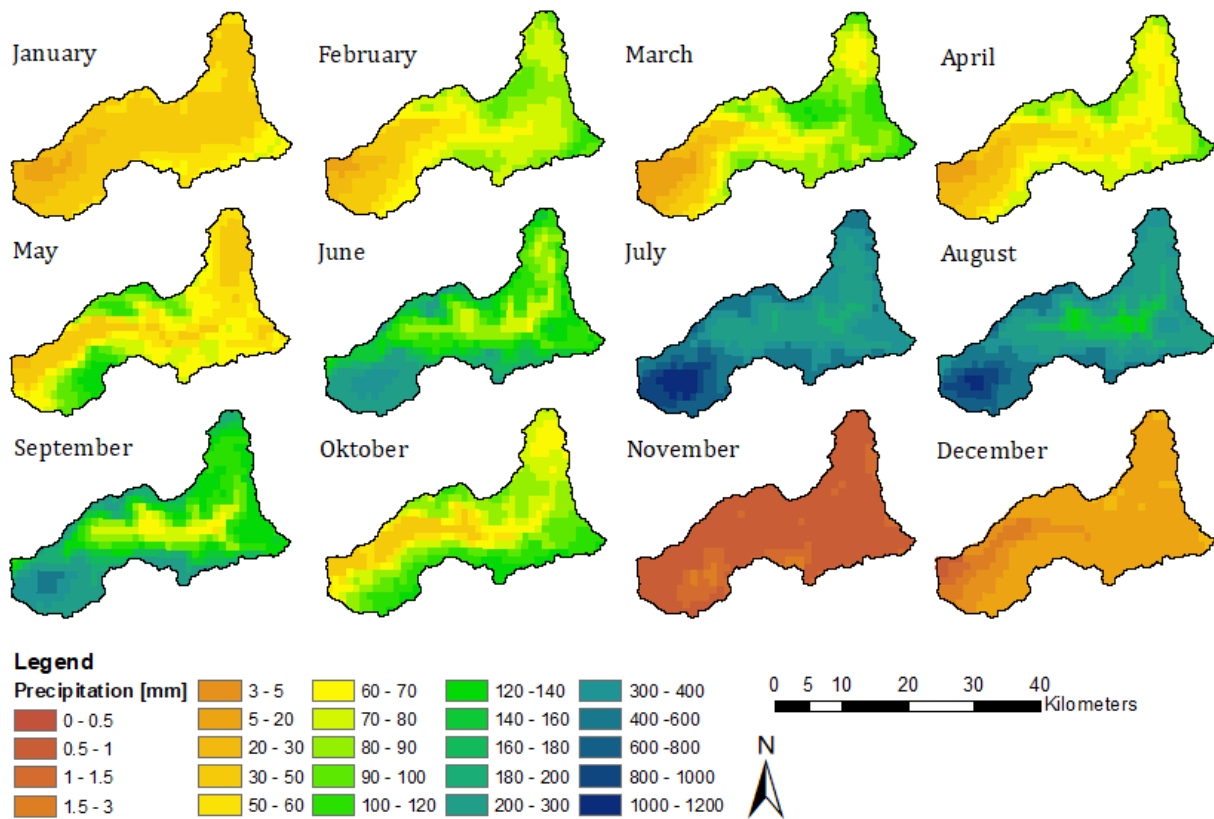
FIGURE 17 | Modelled monthly cumulative precipitation.
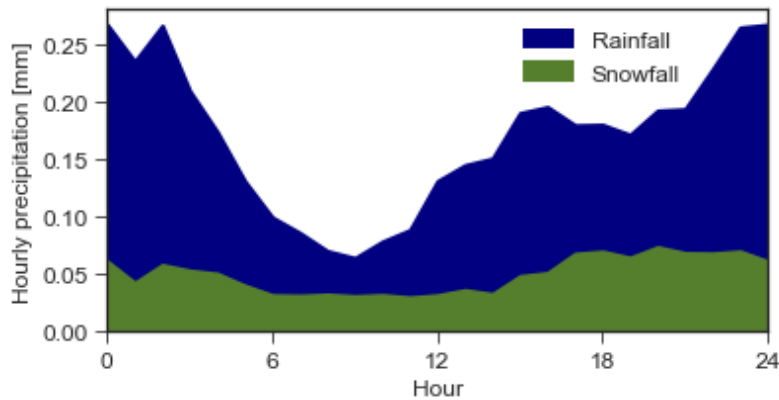
FIGURE 18 | Hourly average catchment-wide rainfall and snowfall.

3.1.3   Incoming shortwave radiation

Figure 19 shows the observed and modelled incoming shortwave radiation and the modelled clear-sky incoming shortwave radiation at all three AWSs where it was measured, which are located on a nearly horizontal (4°) south-facing (AWS Yala BC) and gentle (respectively 16° and 18°) southwest-facing (AWS Yala Glacier and AWS Kyangjin) slopes. The model captures the seasonal pattern reasonably well, with least incoming shortwave radiation during the monsoon season. However, especially for the months April-October, the model underestimates the amount of incoming shortwave radiation. Furthermore, the modelled values are highest in winter, while the observed values are highest in the pre and post-monsoon seasons.
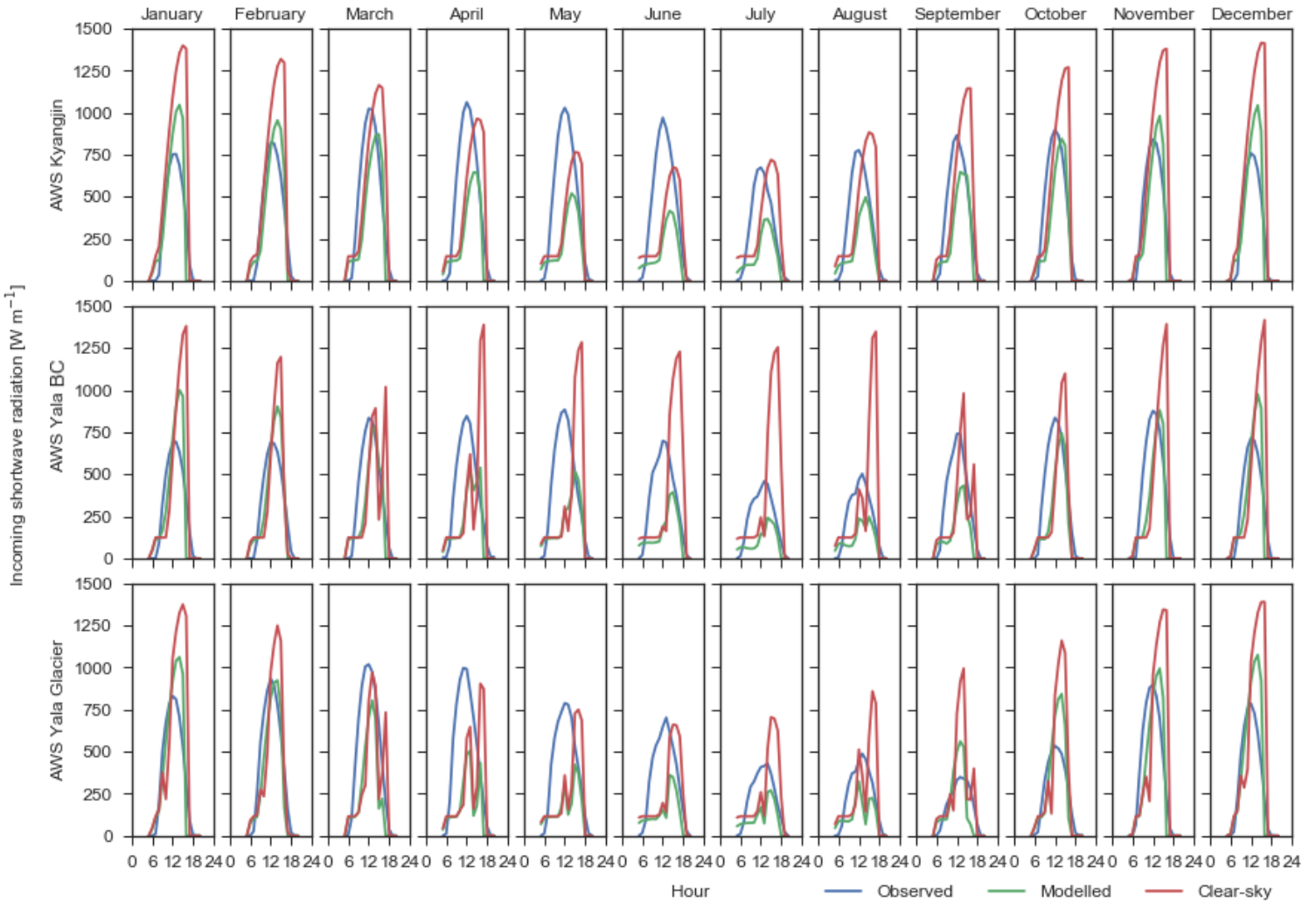
FIGURE 19 | Modelled (clear-sky) and observed monthly average hourly incoming shortwave radiation at all measuring sites.

The modelled clear-sky shortwave shortwave radiation at AWS Kyangijn and Yala Glacier is highest in the winter and lowest in the monsoon. This is because the inclined surfaces receive more radiation in the winter, as a result of the surface being positioned more perpendicular to the direction of the solar radiation beam. However, the measuring devices are positioned horizontally, which explains the disagreement between the modelled and observed shortwave radiation. Furthermore, at AWS Yala BC and AWS Yala Glacier, the clear-sky radiation has some significant dips, which are not visible in the observations (Figure 19). This may be caused by overestimated shading by the surrounding topography. The discrepancy between the modelled and observed shortwave radiation is further explained in the discussion.

Figure 19 shows that under- and overestimations are generally comparable for all sites. The modelled ratios are therefore in better agreement with the observed ratios (RMSD = 0.96; Figure 20). For the validation analysis values lower than 30 W m^{-2} were filtered, to reduce bias of extreme ratios with low incoming shortwave radiation. However, there are still some extreme high ratios, predominantly during the monsoon due to the low modelled values at AWS Kyangjin in comparison with AWS Yala BC, and also extreme low ratios, as a result of the dips at AWS Yala BC and AWS Yala Glacier. The scaling of the observed shortwave radiation at AWS Kyangjin with ratio fields of the model, therefore, resulted in unrealistic values throughout the catchment.
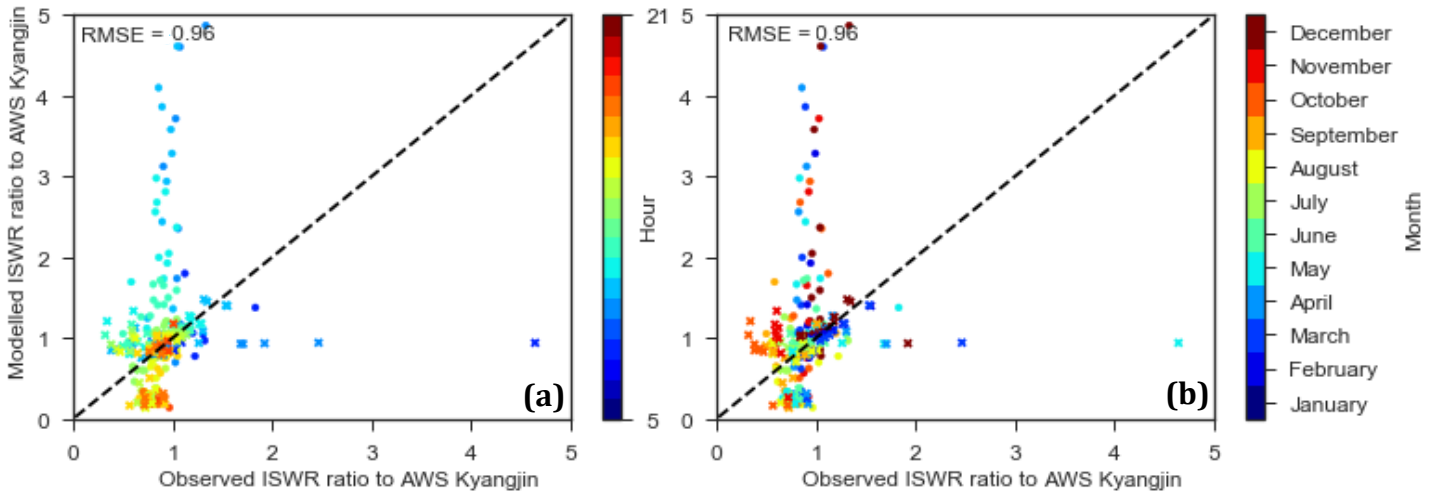
FIGURE 20 | Modelled against observed incoming shortwave radiation ratio (ISWR) to AWS Kyangjin **(a)** grouped by hour and **(b)** grouped by month. Circles indicate Yala AWS and crosses Yala AWS Glacier.

Hence, we chose to force the model only with the modelled incoming shortwave radiation (Figure 21). The outputs show a clear seasonal variation in incoming shortwave radiation pattern, with in the non-monsoon season, the highest values on the south-facing slopes and the lowest values on the north-facing slopes, while in the monsoon season the highest values are found in the upper part of the catchment and the lowest values in the lower part of the catchment. The pattern in the non-monsoon season is mainly driven by the pattern of the clear-sky incoming radiation, while the pattern in the monsoon season is mainly driven by differences in cloudiness.
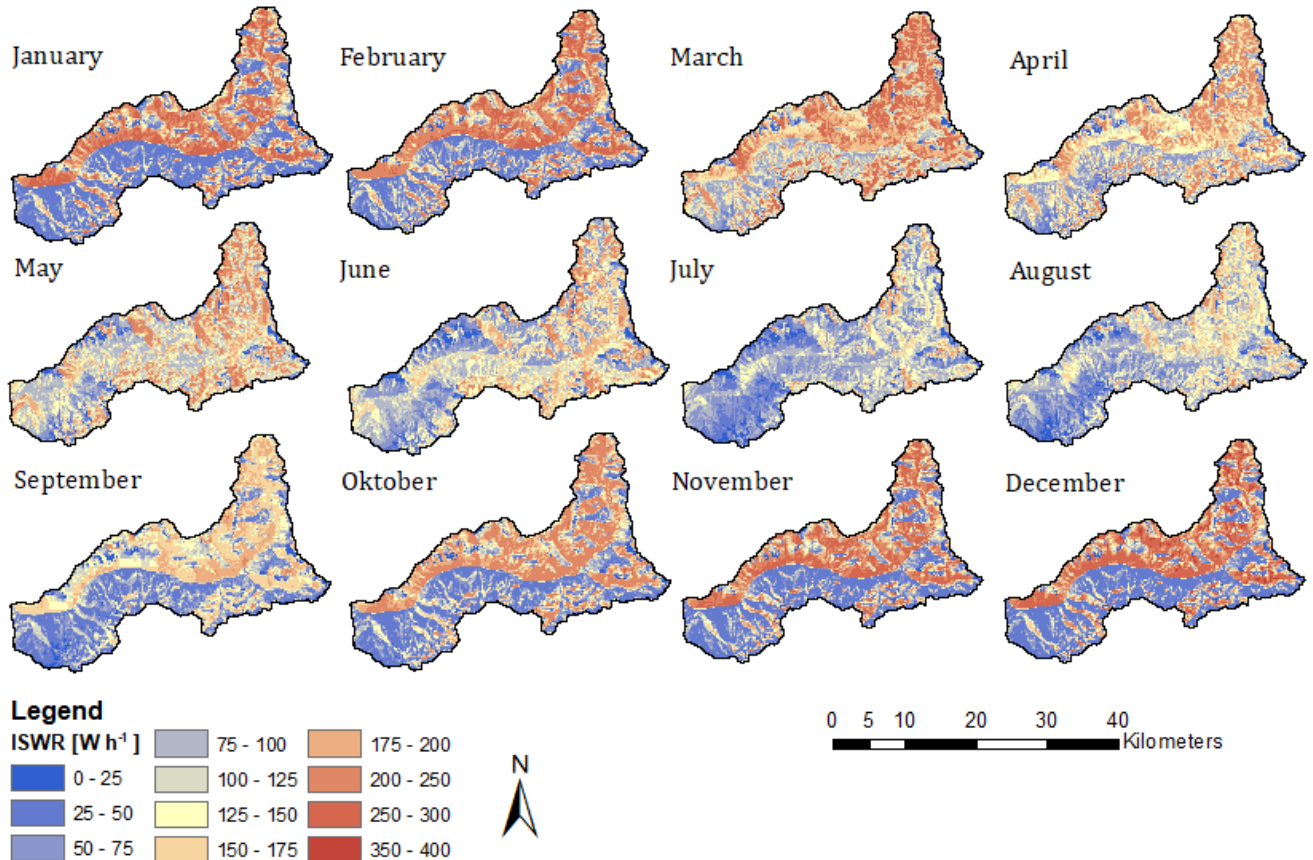
FIGURE 21 | Monthly average modelled incoming shortwave radiation.

The modelled clear-sky shortwave radiation at north-facing slopes is higher in the monsoon than in winter, while at south-facing slopes it is higher in winter than in the monsoon. As a result, the catchment-wide average modelled clear-sky shortwave shortwave radiation is fairly similar throughout the year, with values ranging from 189 W m^{-2} in May to 209 W m^{-2} in January. The difference between the clear-sky incoming shortwave radiation and the incoming shortwave radiation is largest in the monsoon season, due to the lower atmospheric transmissivity, due to high cloudiness. The monthly average modelled incoming shortwave radiation is listed in Table 5, with the highest values (143 W m^{-2}) in February and March, the lowest value (91 W m^{-2}) in July, due to higher cloudiness. The annual average modelled incoming shortwave radiation is 126 Wm^{-2}.

TABLE 5 | Monthly average catchment-wide modelled incoming shortwave radiation.

| Month	1	2	3	4	5	6	7	8	9	10	11	12
ISWR (Wm^{-2})	132	143	143	137	135	117	91	102	108	128	137	141

3.2 Validation

The meteorological data shown in the previous section, was used to force the refreezing model. To get a confirmation about the model performance, the corresponding model outputs are validated against MODIS and in situ snow depth and SWE observations. Model experiments with the simple degree-day and the improved refreezing approach with both an hourly and daily timestep were performed, to get a confirmation about the model performance. The daily and hourly runs of the simple degree-day approach, are referred to as respectively the daily old and hourly old runs, and the daily and hourly runs of the improved approach, are referred to as respectively the daily new and hourly new runs.

3.2.1 MOYDGL06 snow cover fraction

The MOYDGL06 MODIS snow cover fraction of the catchment is plotted together with the modelled 8-day maximum snow cover fractions of the catchment for the non-monsoon season in Figure 22. Figure 22 shows a reasonable fit between the observations and the model runs, with the daily model outputs having the best match. The model runs show a similar pattern for each year. The outputs of the daily runs are nearly identical and therefore not both visible, and generally yield higher snow cover fractions than the MODIS observations. The hourly runs yield snow cover fractions which are occasionally lower than the MODIS observations, mostly during the post-monsoon and winter. The high observed snow cover fractions in the post-monsoon season of 2013 in comparison with other years, is captured well by all the model runs.

3.2.2 In situ snow depth and SWE measurements

The observed snow depth and SWE are plotted together with the modelled snow depth and SWE in Figure 23. The model runs show similar patterns at all the stations. Figure 23 shows a reasonable fit between the observations and the model runs. However, the timing of the melt runoff onset during spring is somewhat later for all model runs than what is observed. The hourly model runs are in better agreement with the observations than the daily runs. The snow depth and SWE of the daily runs generally decrease later in time than the hourly runs. This is because when daily average temperatures are below zero, melt can occur during the day for the hourly runs. This also explains why the outputs of the daily run do not decrease after accumulation in the post-monsoon.
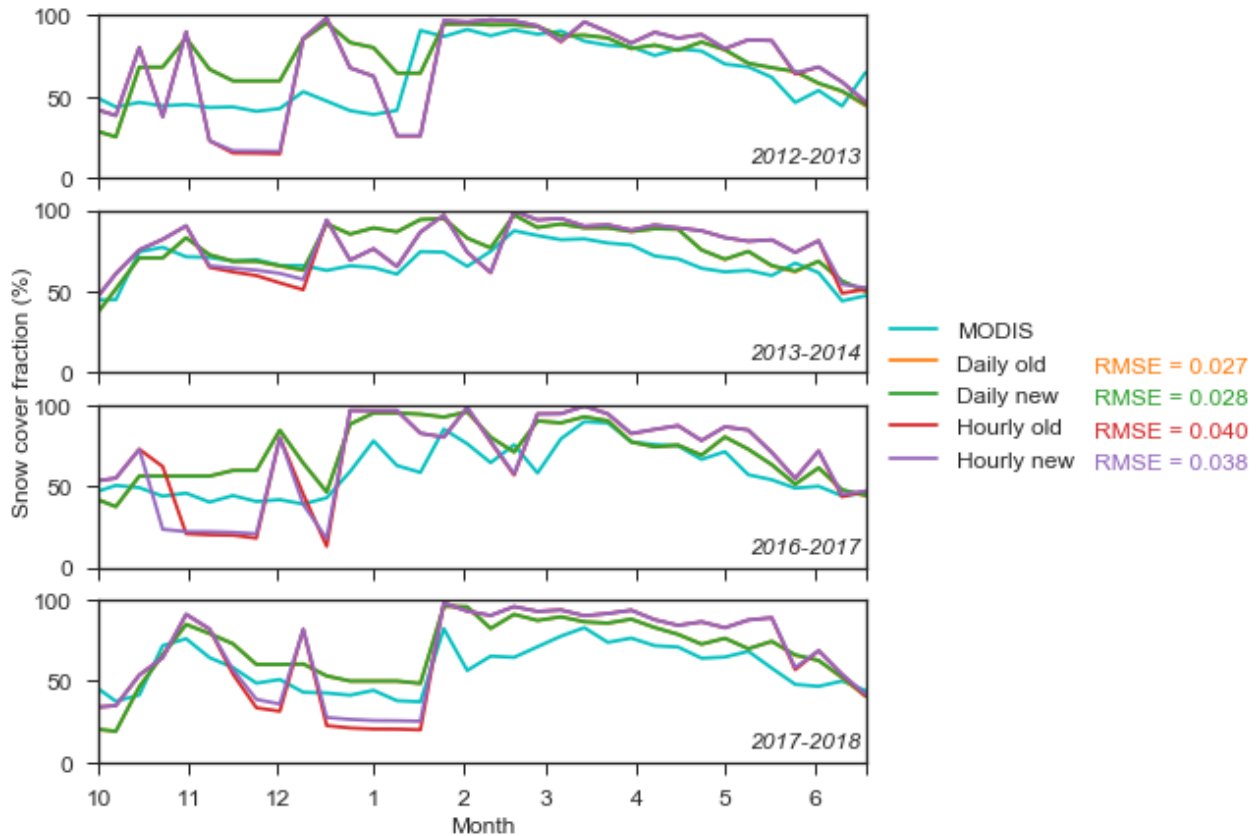
FIGURE 22 | MODGL06 MODIS and modelled 8-day maximum snow cover fraction of the catchment for the non-monsoon season for (i) the daily run with the old refreezing, (ii) the daily run with the new refreezing, (iii) the hourly run with the old refreezing and (iv) the hourly run with the new refreezing. The RMSE (%) is given for the match between the modelled runs and the MODIS observations.

The hourly old run has the best match with the observations. This is as expected, since the old model was calibrated. The hourly runs of the old model generally yield lower snow depths and SWE and an earlier timing of melt onset than the hourly run of the new model. This suggests that the simple degree-day approach of Stigter et al. (2017) yields a lower amount of refreezing than our approach. Since the refreezing is underestimated, the melt factor might be underestimated during calibration in order to compensate for the lack of refreezing and produce results that match the observations. This could explain the later onset of melt in our snow depth and SWE simulations with the improved refreezing compared to the observations. The hourly new run has improved performance in December, January and February at AWS Yala BC compared to the old hourly run. The hourly old snow depth decreases to zero, while the observed and hourly new snow depth is retained. This suggests that refreezing is important to retain SWE over the pre-monsoon and winter.
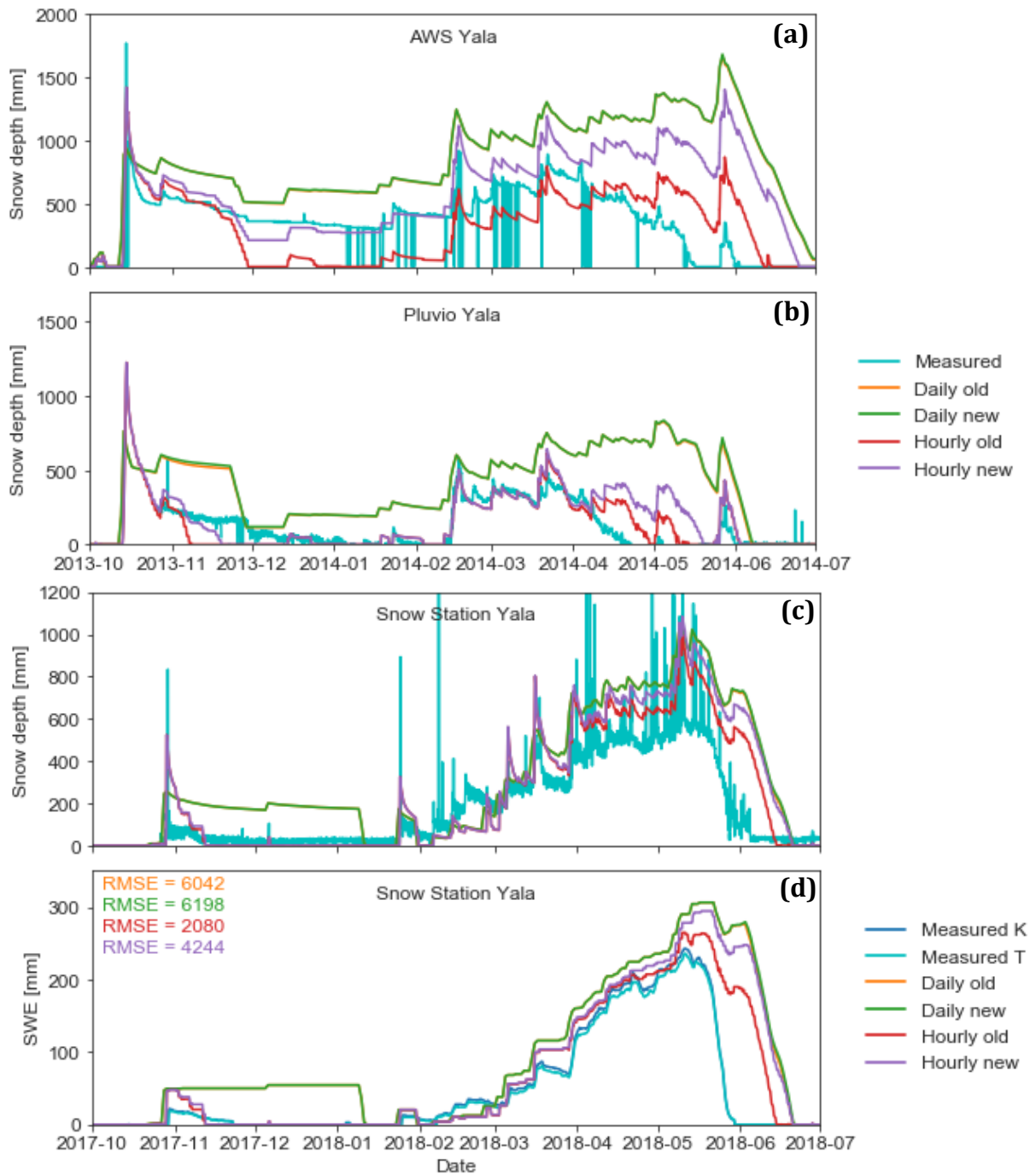
FIGURE 23 | Measured and modelled snow depth at **(a)** AWS Yala BC, **(b)** Pluvio Yala and **(c)** Snow Station Yala. **(d)** Measured SWE derived from Potassium (^{40}K) and Thallium (^{208}Tl) gamma rays and modelled SWE at Snow Station Yala for (i) the daily run with the old refreezing, (ii) the daily run with the new refreezing, (iii) the hourly run with the old refreezing and (iv) the hourly run with the new refreezing The RMSE (mm) is given for the match between the modelled runs and the observations. The RMSE are not derived for the snow depth as there are many spikes related to sensor limitation

3.3 Model results

3.3.1 Spatial patterns

The spatial patterns of the annual average melt runoff, rain runoff, refreezing and refreezing ratio are shown in Figure 24. The melt runoff increases with elevation up to 5,590 m a.s.l. after which it decreases, and reaches zero at 6,090 m a.s.l. This indicates that above 6,090 m a.s.l. all melt refreezes, is retained by the snowpack or that no melt occurs. The rain runoff is highest in the west and shows an increase in precipitation with elevation up to about 5,500 m a.s.l. in the eastern part of the catchment, after which is decreases, and reaches zero at 6,000 m a.s.l. The melt and rain runoff pattern correspond respectively to the temperature and precipitation forcing data. Refreezing increases with elevation up to 5,900 m a.s.l., with a peak around 4,800 m a.s.l. This is a small offset from the peak of the temperature fluctuations around the freezing point (Figure 11). The ratio between refreezing and the melt runoff, referred to as refreezing ratio henceforth, also increases with elevation, with a peak around 4,800 m a.s.l.

The mean annual catchment-wide refreezing is 131 mm, the melt runoff 368 mm and the rain runoff 1015 mm. This means that the snowmelt runoff contribution is 26% (excluding glacier melt) and that 35% of the melt runoff refreezes, which indicates the refreezing ratio. Since, part of the melt is recycled by melt-refreeze cycles, the total melt (482 mm) is higher than melt runoff. This means that 27% of the melt refreezes. Refreezing contributes 23% of the annual SWE accumulation, which mainly involves meltwater refreezing and only a small contribution (estimated 2.3% of the annual SWE accumulation) of rain refreezing.
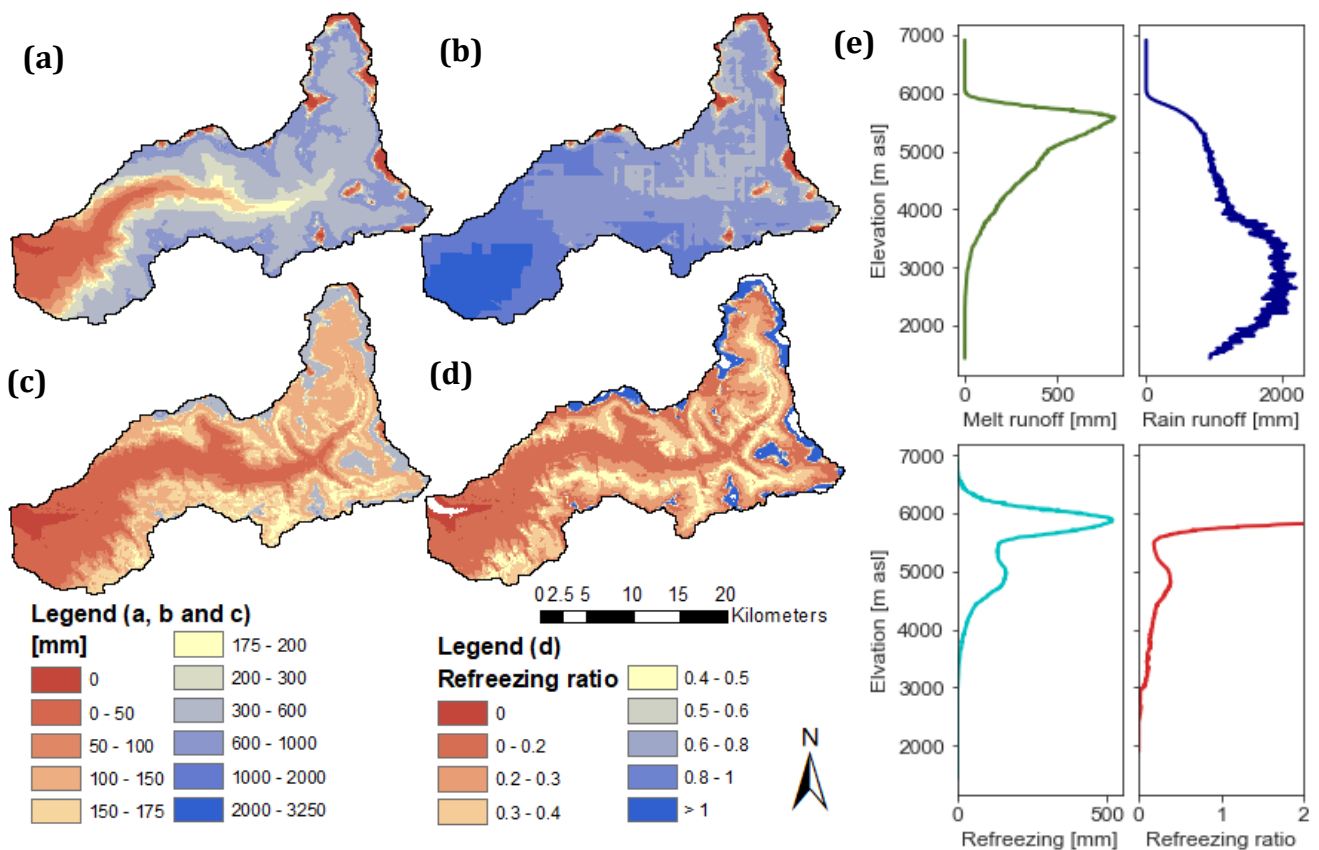
FIGURE 24 | Annual average **(a)** melt runoff, **(b)** rain runoff, **(c)** refreezing and **(d)** refreezing melt ratio. **(e)** Elevation profiles of melt runoff, rain runoff, refreezing and refreezing ratio averaged over 10-m elevation bins.

The snow water balance ($\Delta SWE = P - Q_p - Q_r$) reveals that on average 80 mm SWE erroneously accumulates annually. This only occurs above 5,500 m a.s.l., which is further illustrated in the following section, and is the result of a lack of redistribution of snow from higher to lower elevations (e.g. by wind or snow avalanches) and a lack of sublimation. The overestimation of SWE also results in overestimation of refreezing at these elevations. Hence, we focus on the output below 5,500 m a.s.l.

To study the spatial patterns in the catchment in more detail, we defined 11 elevation bands with areas ranging from 5.6% to 13.5% of the total catchment area (Table 6 and Figure 25). The annual average melt runoff, rain runoff, refreezing and refreezing ratio distribution by elevation band is shown in Figure 26a. It shows a similar patterns as discussed for Figure 24, with a notable peak of refreezing (157 mm) and the refreezing ratio (0.38) in the 4,750– 5,000 m a.s.l. elevation band. The ratio between temperature and solar melt shows no clear relation with elevation (Figure 26b).

There is a clear relation between aspect and the relative contribution of solar and

TABLE 6 | Elevation bands in the catchment.

Elevation (m a.s.l.)	Area (10^2 m^2)	Area (%)
> 5750	4158	7.1
5500 – 5750	5198	8.9
5250 – 5500	7451	12.7
5000 – 5250	8053	13.8
4750 – 5000	7870	13.5
4500 – 4750	5946	10.2
4250 – 4500	4194	7.2
4000 – 4250	3743	6.4
3500 – 4000	4994	8.5
3000 – 3500	3246	5.6
< 3000	3595	6.2
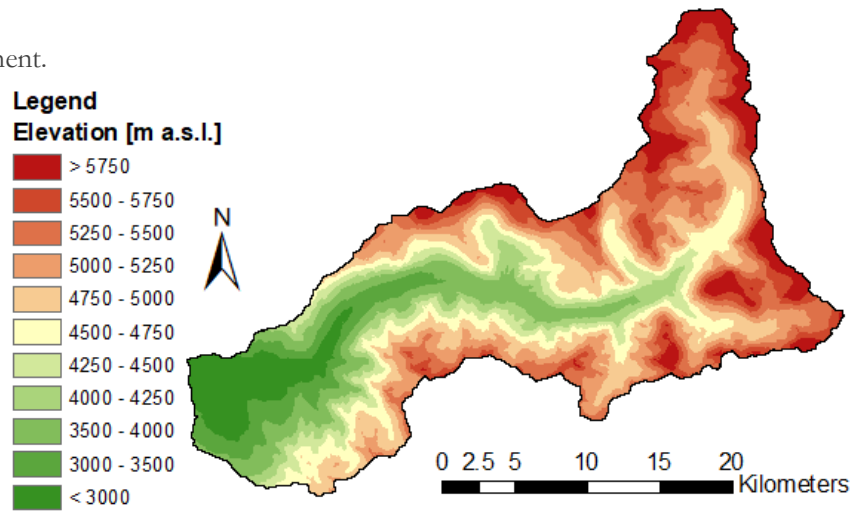
FIGURE 25 | Elevation bands in the catchment.
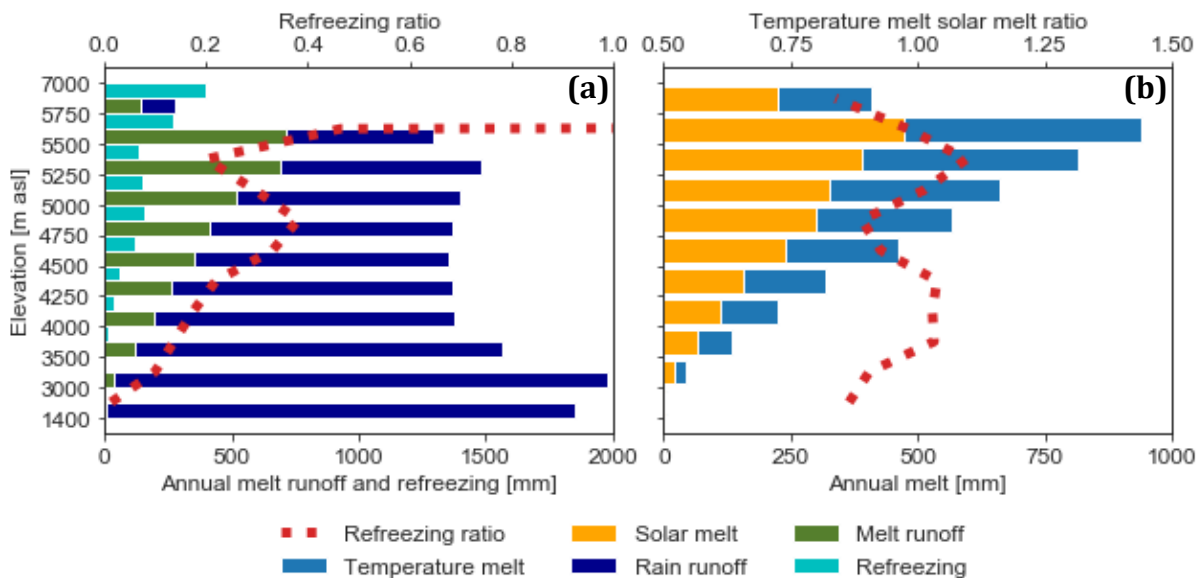
FIGURE 26 | Annual average **(a)** refreezing ratio, rain runoff, melt runoff and refreezing, **(b)** temperature melt, solar melt and temperature melt solar melt ratio distribution by elevation band.

temperature melt, with south-and west-facing slopes having more solar melt contribution and north- and east-facing slopes more temperature melt contribution (Figure 27b). This is related to a high amount of incoming shortwave radiation at south-facing slopes, and most incoming shortwave radiation at west facing slopes in the afternoon, when temperatures are highest. The net effect is that there is an earlier melt onset in the melt season at south- and west-facing slopes at equal elevation, which results in a lower average SWE (Figure 27c).

Figure 28 shows the annual average refreezing against elevation and aspect, and the associated relative refreezing anomaly, absolute refreezing anomaly and the refreezing ratio anomaly compared to the average of the 100-m elevation bin. Below 5,000 m a.s.l. and between 5,300 and 5,600 m a.s.l. refreezing is higher at north- and northeast-facing slopes than at west and southwest-facing slopes of similar elevation (Figure 28b). Between 4,000 and 4,500 m a.s.l. the absolute differences are largest (Figure 28c). Above 5,600 m a.s.l. and between 5,000 and 5,300 m a.s.l., refreezing is highest at the south- and southwest-facing slopes (Figure 28b).

The generally lower refreezing on south- and southwest-facing slopes is probably related to the earlier melt onset. The higher refreezing above 5,600 m a.s.l. on south and southwest-facing slopes is probably related to more total melt. The higher refreezing between 5,000 and 5,300 m a.s.l. might be related to enhanced melt-refreeze cycles. This is supported by Figure 28c, which reveals that the refreezing ratios are highest at south and southwest-facing slopes between 5,000 and 5,300 m a.s.l.
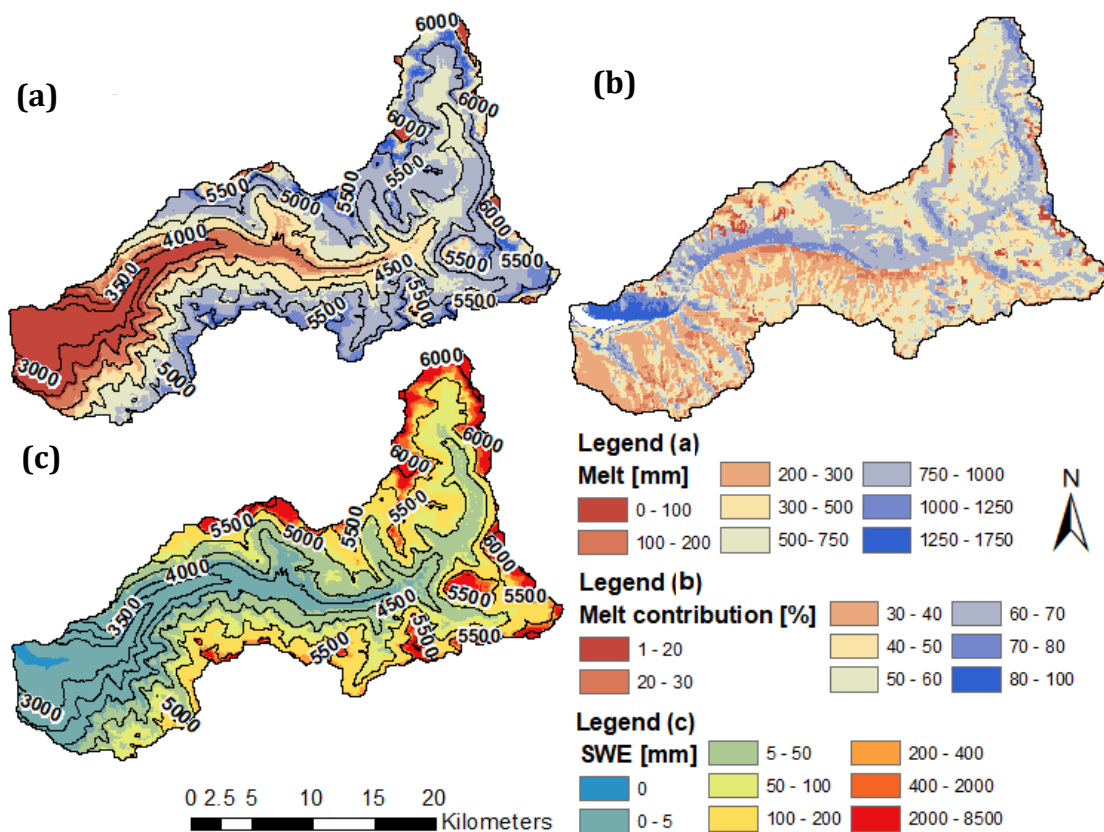
FIGURE 27 | Annual average (a) total melt, (b) solar melt contribution and (c) SWE.
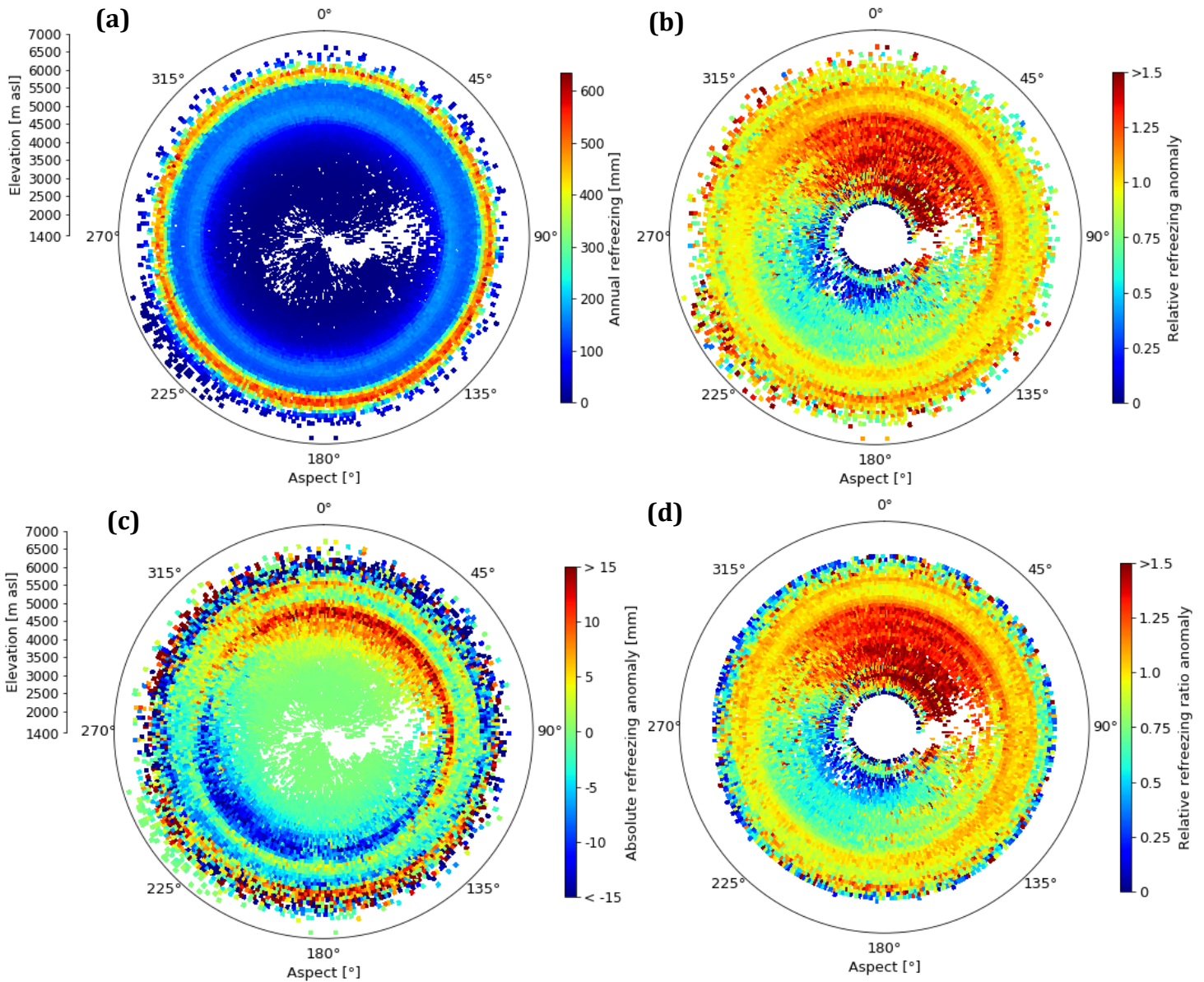
FIGURE 28 | Annual average **(a)** refreezing averaged over 100-m elevation bins, **(b)** relative refreezing anomaly **(c)** absolute refreezing anomaly, **(d)** relative refreezing ratio anomaly against elevation and aspect. The anomalies are calculated against the averages of the 100-m bins.

3.3.2 Temporal patterns

Figure 29 shows the spatial pattern and distribution of the monthly average refreezing. Most refreezing occurs in March, April, May and November, while during the monsoon and winter least refreezing occurs. During the non-monsoon season 67% of the melt runoff and 42% of the melt refreezes. The monthly average refreezing distribution by elevation band is shown in Figure 30. It reveals that during the pre-monsoon most refreezing occurs at relatively low elevations, with increasing elevation throughout the season. From July to February most refreezing occurs in the highest elevation band, but in October, November and February there is also substantial refreezing at lower elevation bands.

The two prerequisites for refreezing are availability of meltwater and below zero temperatures. These conditions are more likely to occur when there is substantial SWE in

40

combination with diurnal variability in temperatures and temperatures around freezing point. During the monsoon season, the temperatures are constant and generally above freezing point, and SWE is mostly absent (Figure 31), which explains the small amount of refreezing. Only above 5,500 m a.s.l., the amount of SWE is large enough and the night temperatures cold enough for substantial refreezing to occur. In winter, temperatures have a high diurnal variability and SWE is accumulating at lower elevations. However, as snow is accumulating throughout the winter, the temperatures also decrease, which limits the fluctuations around freezing point and shifts the 0°C line to lower elevations, where less SWE is present, which explains the low amount of refreezing.

In both the pre-monsoon and post-monsoon seasons, temperatures have a high diurnal variability and the temperatures fluctuate around freezing point at intermediate elevation. However, the refreezing elevation patterns are contrasting, with more refreezing on a lower elevation in the pre-monsoon, due to a substantial amount of SWE, while there is a low amount of SWE in the post-monsoon season at lower elevations (Figure 31). However, in November the amount of refreezing at lower elevation is also quite high, as a result of substantial SWE caused by extreme precipitation events in October, in combination with temperatures fluctuating around freezing point in November itself. In the pre-monsoon, post-monsoon and winter, there is negligible melt above 5,500 m a.s.l. as a result of low temperatures. However, in the post-monsoon season there is substantial refreezing above 5,500 m a.s.l., which is caused by the presence of melt and rainwater, which have been generated during the monsoon. However, as mentioned previously, the amount of SWE above 5,500 m a.s.l. is erroneously overestimated. As a result, an overestimated amount of
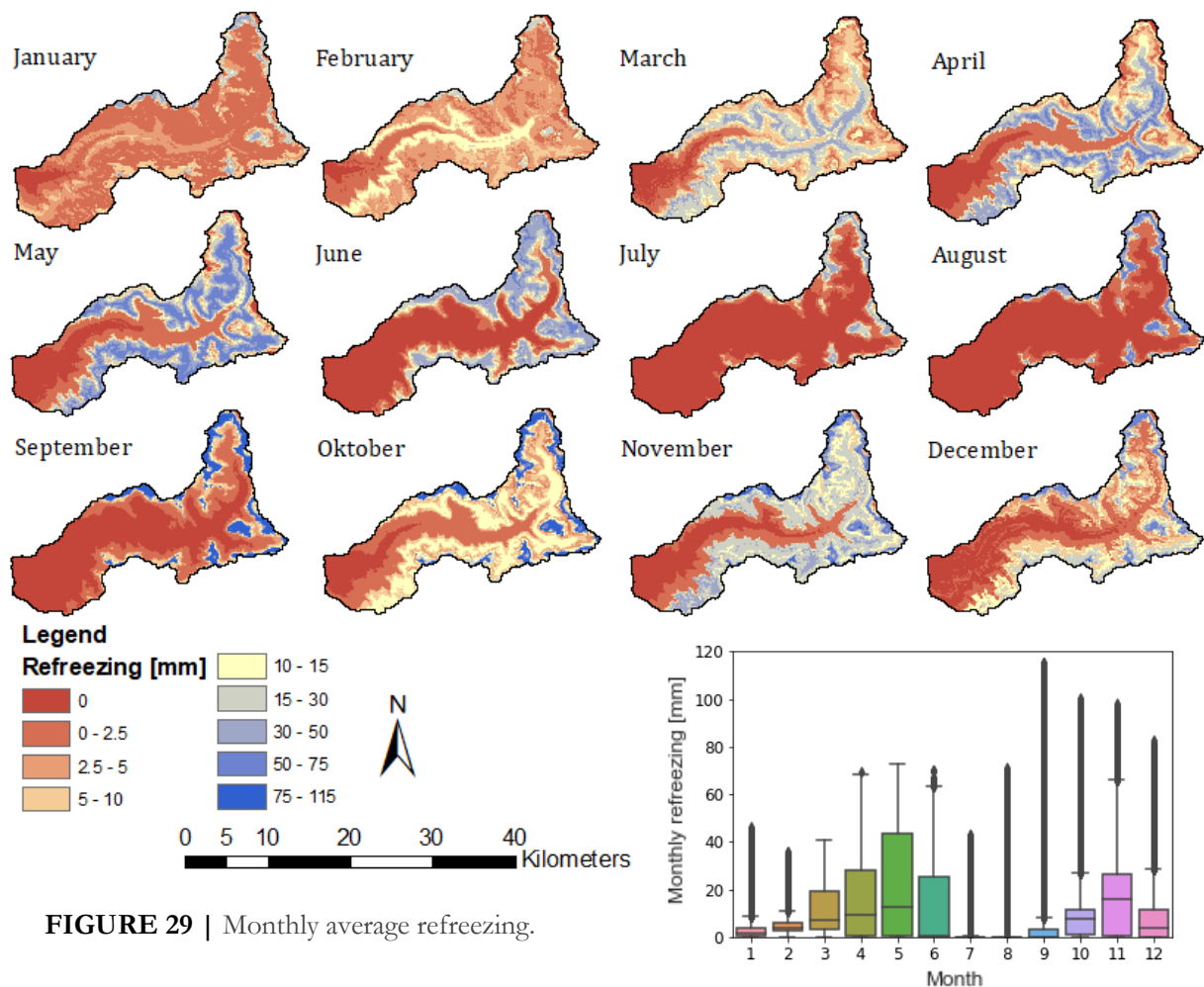

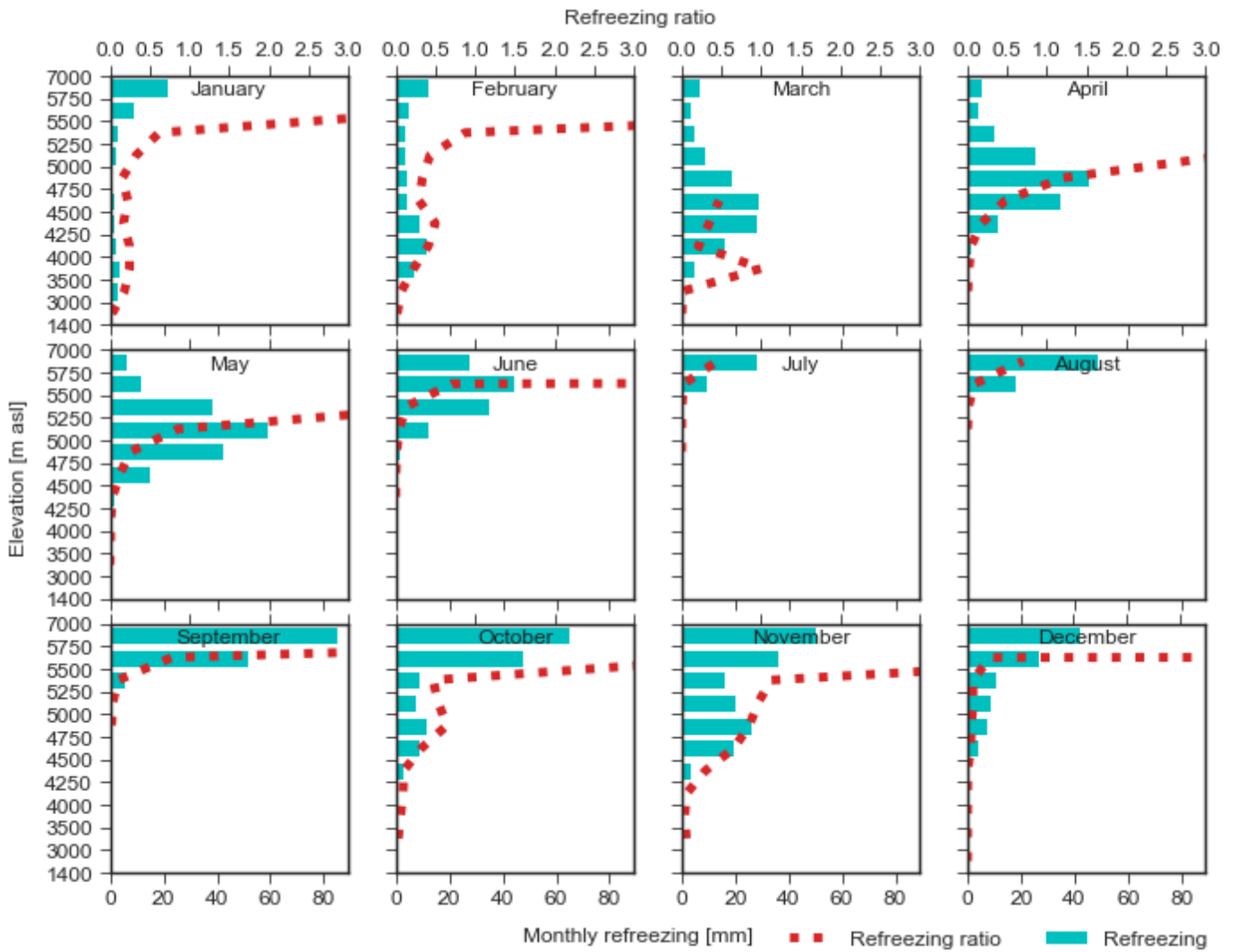**FIGURE 29 |** Monthly average refreezing.

FIGURE 30 | Monthly average refreezing melt ratio, runoff and refreezing distribution by elevation band.
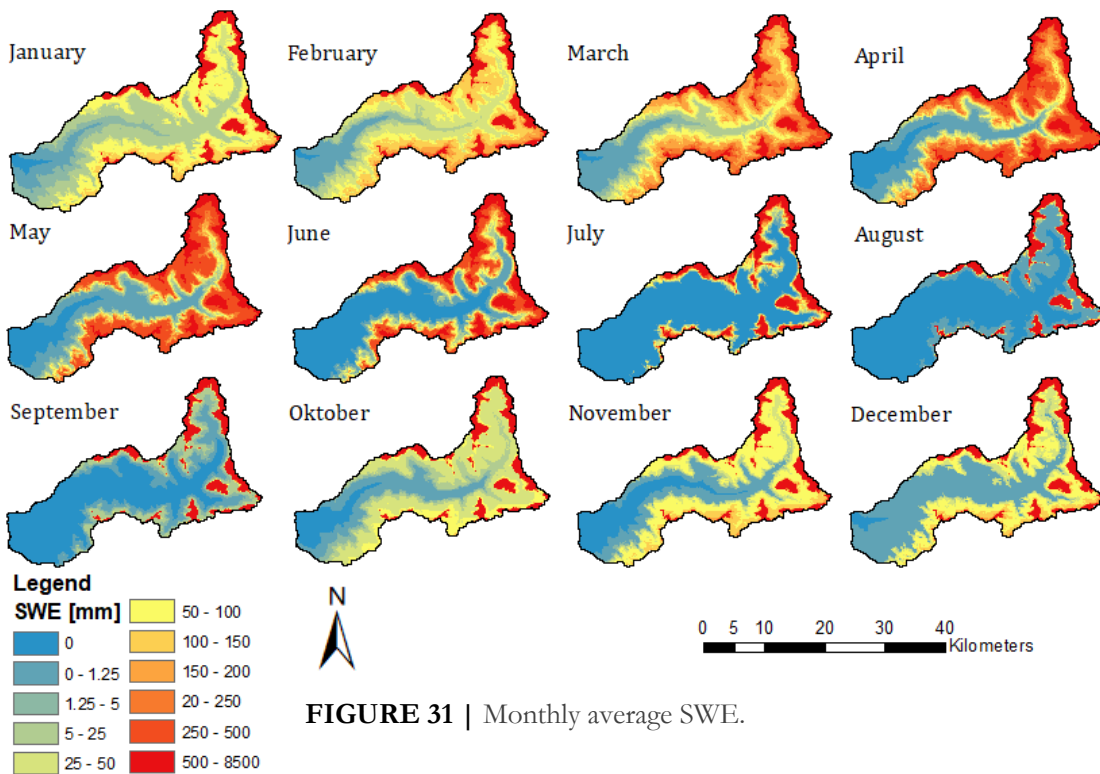

FIGURE 31 | Monthly average SWE.

melt is retained by the snowpack in the monsoon, which subsequently refreezes over the post-monsoon season. The high amount of refreezing above 5,5000 m a.s.l. during the post-monsoon is thus overestimated.

Figure 32 shows indeed that most refreezing occurs in April, May and November with highest refreezing ratios in April, October, November and December. The refreezing in April and May is mainly important for the timing of the melt onset, and the refreezing in November for the accumulation of SWE over the winter. Least refreezing occurs indeed in January, February, July and August. The solar melt contribution is higher than the temperature melt contribution in each month except for June, August and September, which coincides with the period of largest cloud cover and highest temperatures. The melt runoff has a large peak in June and August and a notable peak in March, after which melt runoff decreases again as refreezing increases in April. During the pre-monsoon, runoff consists mostly of melt runoff (85%), whereas it consists mostly of rain runoff (85%) during the monsoon. In October, runoff consists of a comparable amount of melt and rain runoff, whereas in winter there is only a limited amount of melt runoff. 85% of all runoff occurs during the monsoon, consisting of 94% of the total rain runoff and 60% of the total melt runoff (Figure 32).

Figure 33 reveals that most refreezing occurs from 18:00 to 06:00 with a peak around 19:00, while most melt and melt runoff occurs from 06:00 to 18:00. The solar melt is generally larger than the temperature melt during the day, with the expectation from May to August between approximately 10:00 to 15:00, which coincides with large cloud cover. In June to August, there is also substantial temperature melt during the night. The comparison between the total refreezing and diurnal refreezing is shown in Figure 34. Diurnal refreezing is the refreezing of meltwater that was produced in the same day (06:00 to 05:00). The results show that 87.9 mm (67.3%) of the annual average total refreezing is diurnal refreezing. This proves that there are significant diurnal melt-refreeze cycles and this emphasizes the importance of using sub-daily time steps to capture refreezing. The contribution of diurnal refreezing decreases with elevation, but has a similar elevation profile as the total refreezing (Figure 37). Below 5,500 m a.s.l. the diurnal refreezing contributes 85% of the total refreezing.

Besides the strong seasonal and diurnal variability of refreezing, there is also a moderate inter-annual variability. As discussed previously, there is erroneous accumulation of SWE above
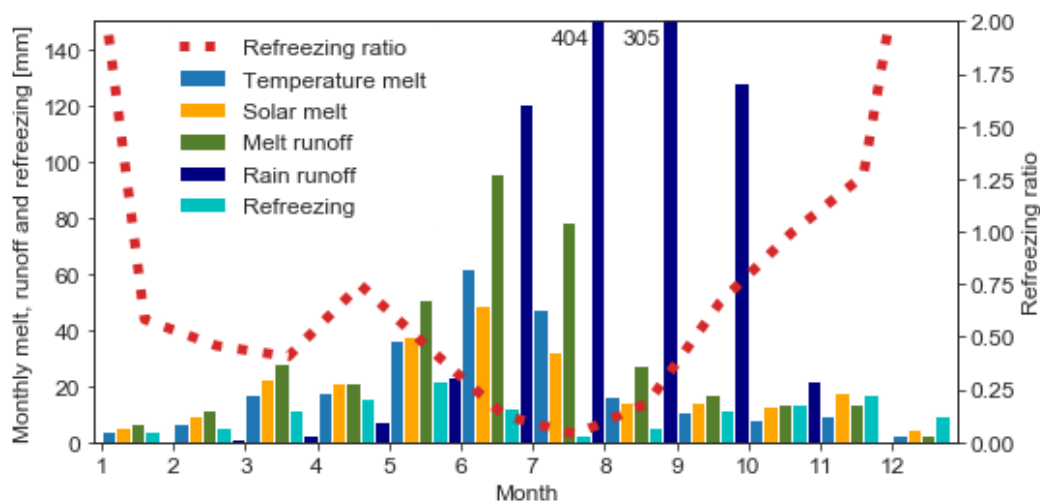
FIGURE 32 | Monthly average refreezing ratio, temperature melt, solar melt, melt runoff, rain runoff and refreezing.
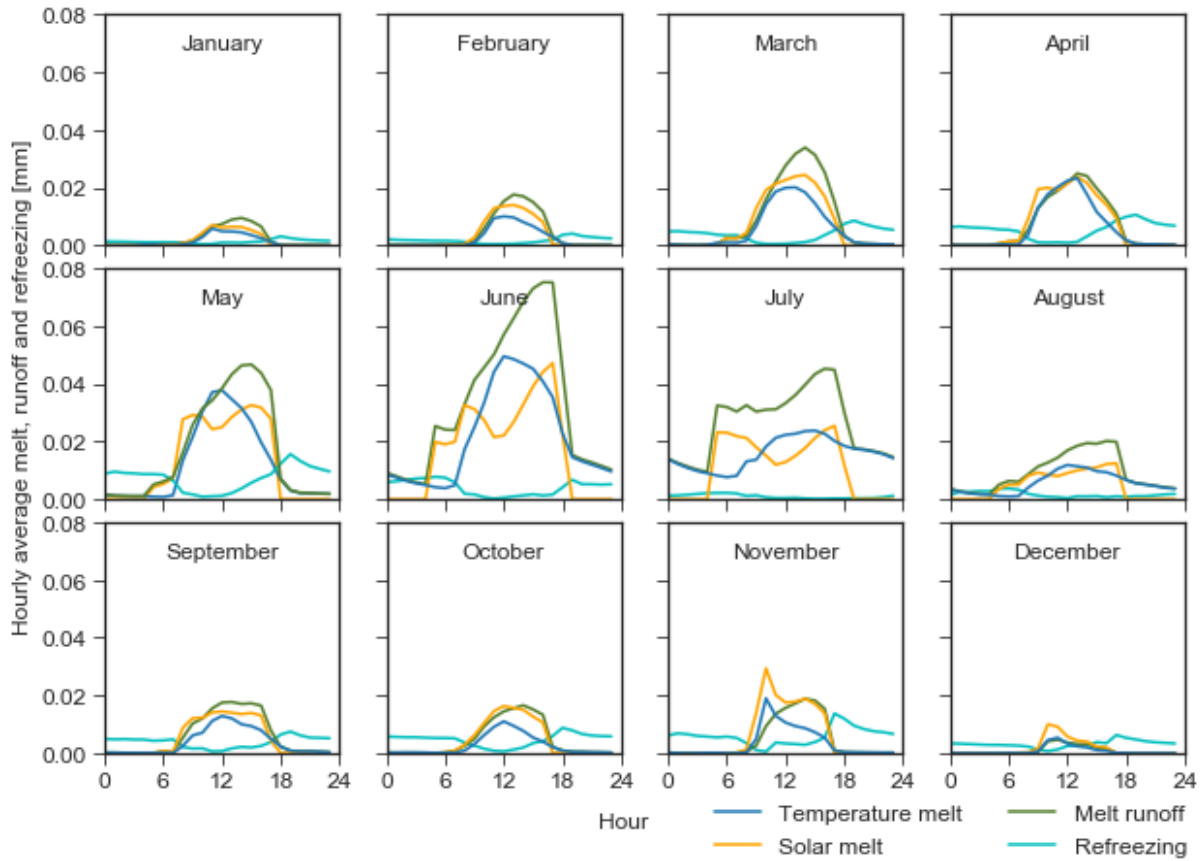
FIGURE 33 | Average hourly monthly temperature melt, solar melt, melt runoff and refreezing.
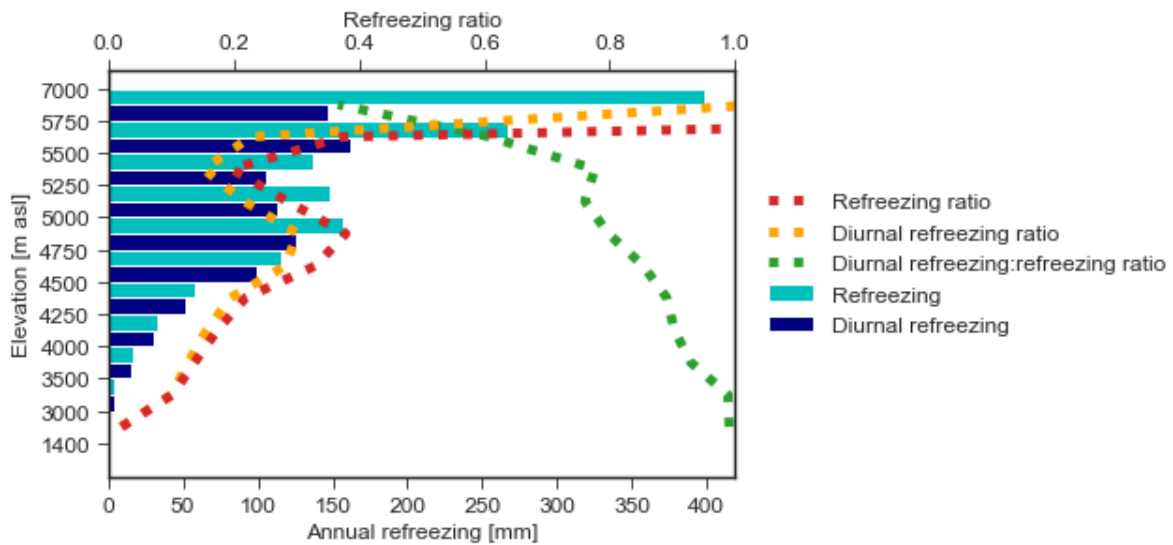
FIGURE 34 | Annual average refreezing ratio, diurnal refreezing ratio, diurnal refreezing:refreezing ratio, refreezing and diurnal refreezing distribution by elevation band.

5,500 m a.s.l. and therefore increasing overestimation of refreezing through time. This is illustrated by the monthly elevation profiles, which show increasing annual trends of SWE and refreezing above 5,500 m a.s.l. (Figure 35d). Based on these outputs, we estimate that above 5,500 m a.s.l., the SWE is annually overestimated with 400 mm and refreezing with 40 mm, which equates to an catchment-wide annual overestimation of 64 mm SWE and 6.4 mm refreezing. However, since redistribution of snow would result in more SWE accumulation at lower elevation, the SWE and refreezing are probably underestimated at lower elevation.
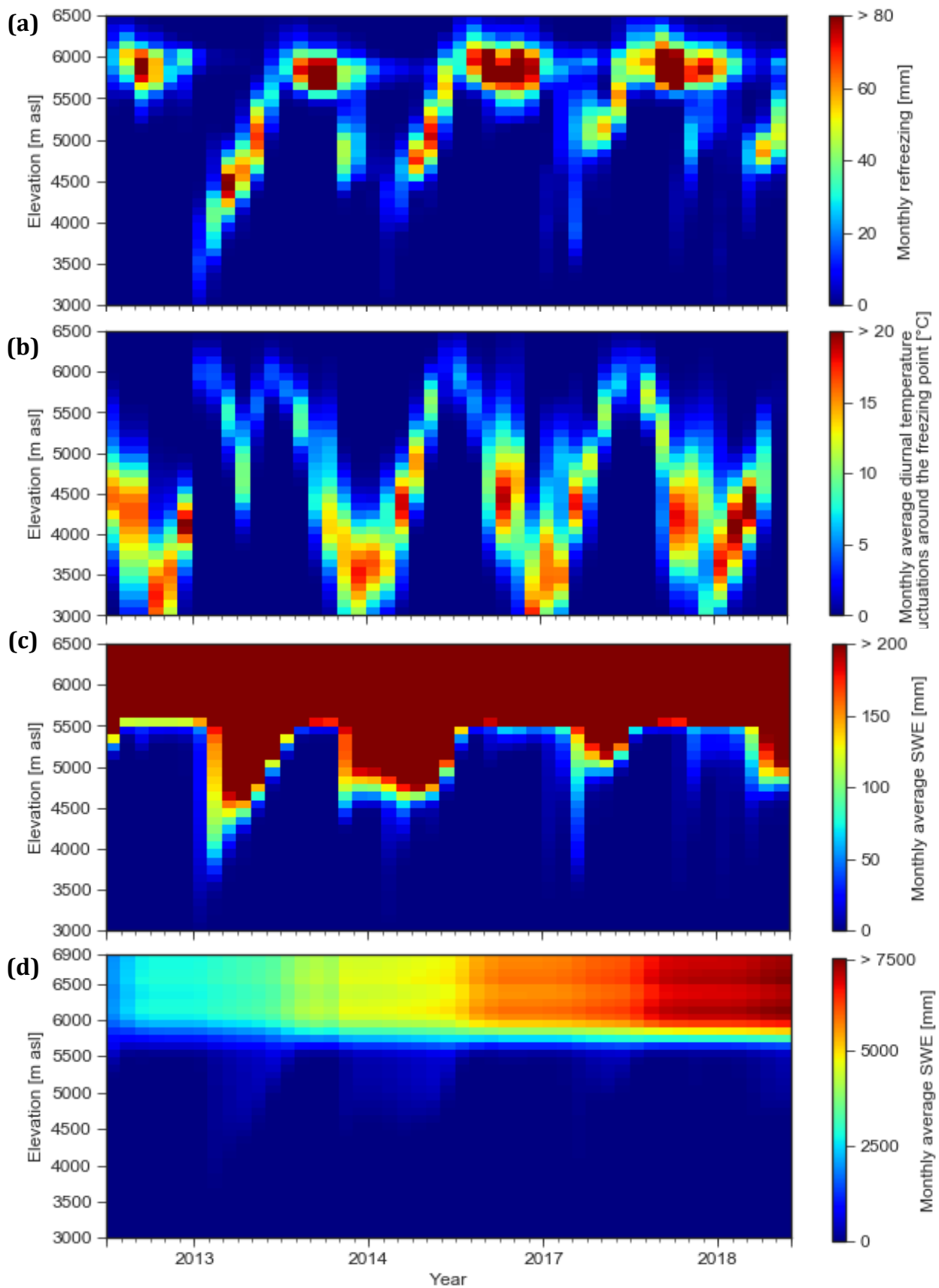
FIGURE 35 | Time-series elevation profiles of monthly **(a)** refreezing, average **(b)** diurnal cumulative hourly temperature fluctuations around the freezing point, **(c)** SWE trimmed to < 200 mm and **(d)** SWE averaged over 100-m elevation bins.

Below 5,500 m a.s.l. the inter-annual variability of refreezing is predominantly controlled by the amount of SWE (Figure 35a,c). The inter-annual variability is most pronounced in November 2013 and the pre-monsoon seasons of 2013 and 2014. Monthly average temperature fluctuations around the freezing point show a less clear relation with refreezing (Figure 35a,b). Figure 36 shows that the catchment average variability of refreezing is highest in the post-monsoon season, which correlates with snowfall and associated SWE accumulation in October. With a high amount of SWE in the post-monsoon season, the relative contribution of solar melt also increases. Apart from this, the relative contribution of solar melt shows no distinct inter-annual variability. The variability of refreezing in the pre-monsoon seems also correlated with snowfall and associated SWE accumulation (Figure 36a,b). The higher refreezing in January seems to be correlated with
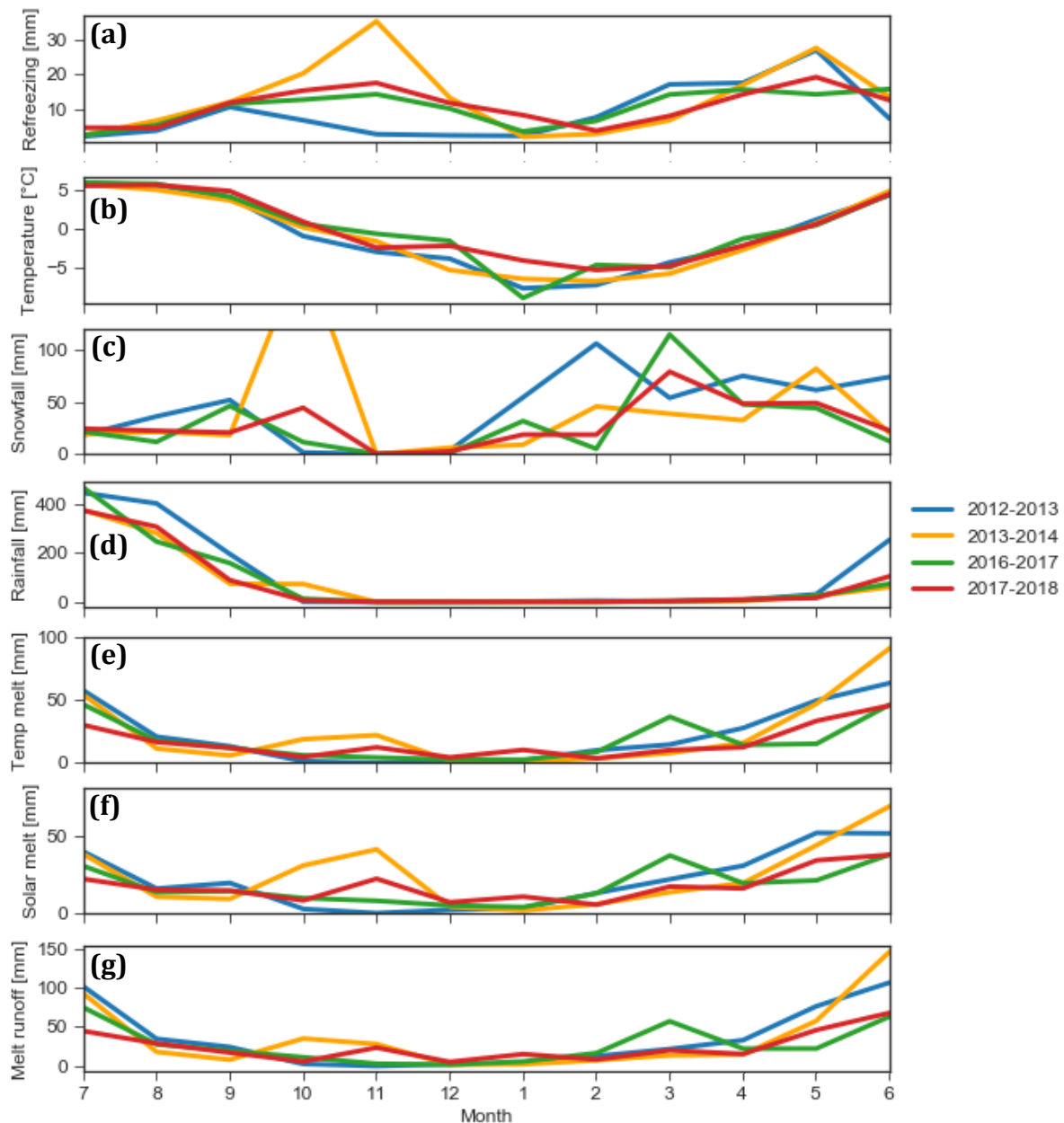
FIGURE 36| Monthly **(a)** refreezing, **(b)** average temperature **(c)** snowfall, **(d)** rainfall, **(e)** temperature melt, **(f)** solar melt and **(g)** melt runoff for each hydrological year.

higher temperatures (Figure 36c). The monthly temperatures and rainfall have a lower inter-annual variability than snowfall, with the temperatures in the post-monsoon and winter having the highest inter-annual variability. Table 7 shows that there are substantial variations in the annual refreezing and runoff.

TABLE 7 | Annual refreezing, melt runoff, rain runoff and refreezing ratio for each hydrological year.

Hydrological year	Refreezing (mm)	Melt runoff (mm)	Rain runoff (mm)	Refreezing ratio
2012-2013	107	420	1326	0.25
2013-2014	159	426	872	0.37
2016-2017	126	353	972	0.36
2017-2018	131	299	887	0.44

3.4 Daily run and run without refreezing

To examine the importance of an hourly time step and to study the impact of refreezing, two additional model experiments, one with a daily time step and one without refreezing, were performed. The results of these experiments are compared to the results of the main model run, with refreezing and with an hourly time step, shown in the previous section.

Figure 37a shows that refreezing is substantially lower at each elevation band with the daily run. Additionally, the melt is also lower at each elevation band with the daily run (Figure 37c). This suggests that sub-daily time steps are important to capture diurnal melt-freeze cycles. The refreezing is substantially lower in each month (Figure 38b). The snowfall is also lower at each elevation band, whereas rain and the rain runoff are higher at each elevation band (Figure 37b,e). This agrees with our previous finding that most precipitation occurs during the evening and night (18:00 – 06:00), when temperatures are lowest (Figure 18). Therefore, the temperature at which most precipitation occurs is lower than the average daily temperature, which results in more snowfall.

The daily run yields lower melt runoff below 5,500 m a.s.l. , due to less snowfall and thus less accumulated SWE (Figure 37d). Whereas above 5,500 m a.s.l. the melt runoff is higher, due to less refreezing, despite the higher melt and lower snowfall. Due to the lower melt, the daily run has a later timing of melt runoff onset, with more runoff concentrated in the monsoon (Figure 38a). As a result of the later melt runoff onset, the average SWE is higher below 5,500 m a.s.l. (Figure 37f), despite there being less snowfall and refreezing. This is in line with the validation model runs, which are located below 5,500 m a.s.l., and where the daily runs have longer snowpack persistency than the hourly runs. The effect of less melt is thus dominant over the effect of less refreezing (even in combination with less snowfall). Above 5,500 m a.s.l. the average SWE is lower, which is due to lower snowfall and lower refreezing, despite the lower melt.

The run without refreezing yields less melt, since there is no recycling of meltwater retained by the snowpack (Figure 37c). This also results in an earlier timing of melt onset (Figure 38a) and a lower average SWE (Figure 37f). Below 5,500 m a.s.l., there is slightly less melt runoff and slightly more rain runoff, since there is no refreezing of rain retained by the snowpack (Figure 37d,e) However, above 5,500 m a.s.l. both rain runoff and melt runoff are higher, as a result of no refreezing and therefore less SWE to retain rain or meltwater. The catchment average outputs of the model runs are listed in Table 7. Refreezing and melt are indeed substantially lower with the daily run (respectively -83% and -25%).
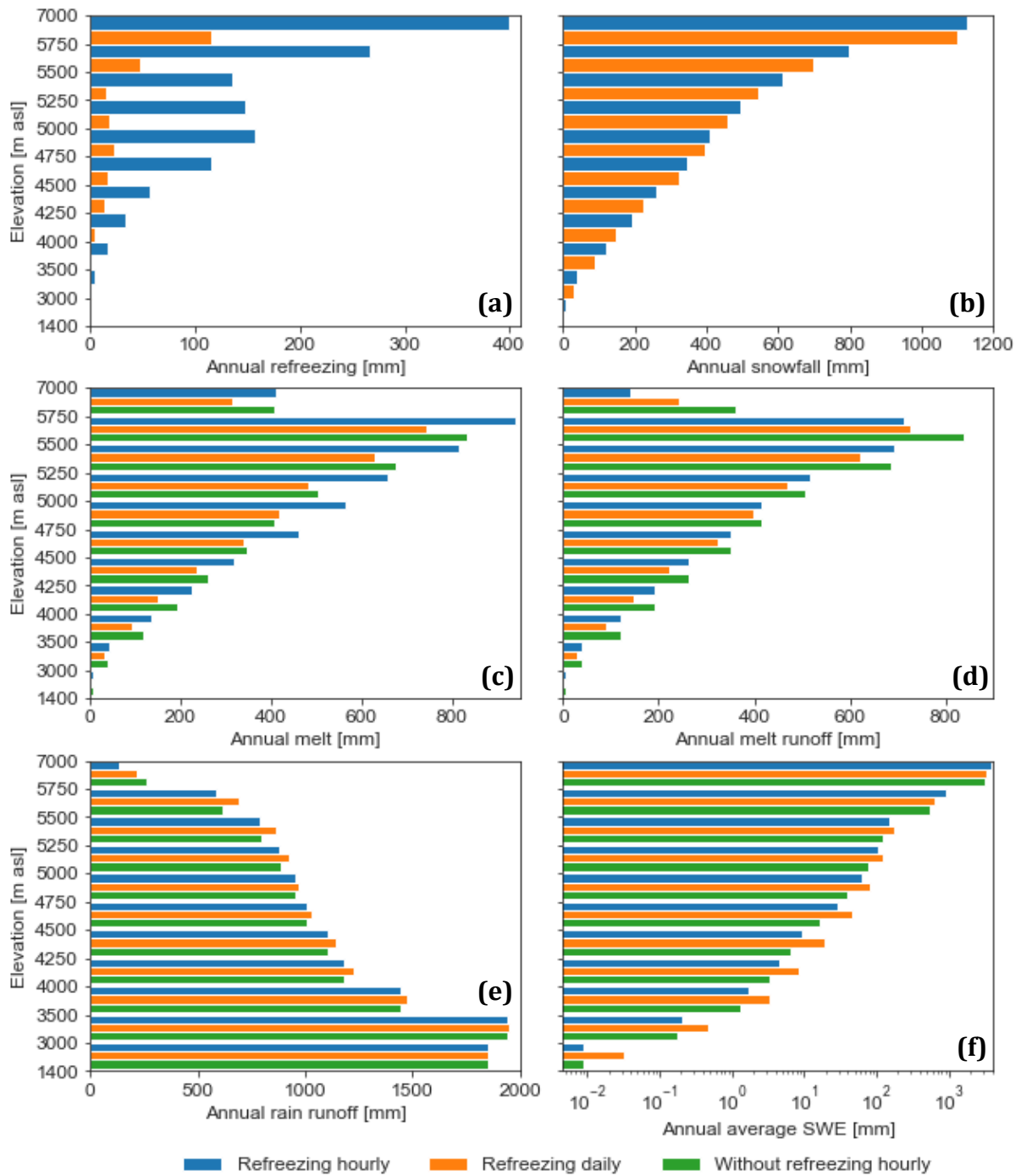
FIGURE 37 | Annual average **(a)** refreezing, **(b)** snowfall, **(c)** melt, **(d)** melt runoff **(e)** rain runoff and **(f)** average SWE distribution by elevation band, of the hourly and daily runs with refreezing and the hourly run without refreezing.
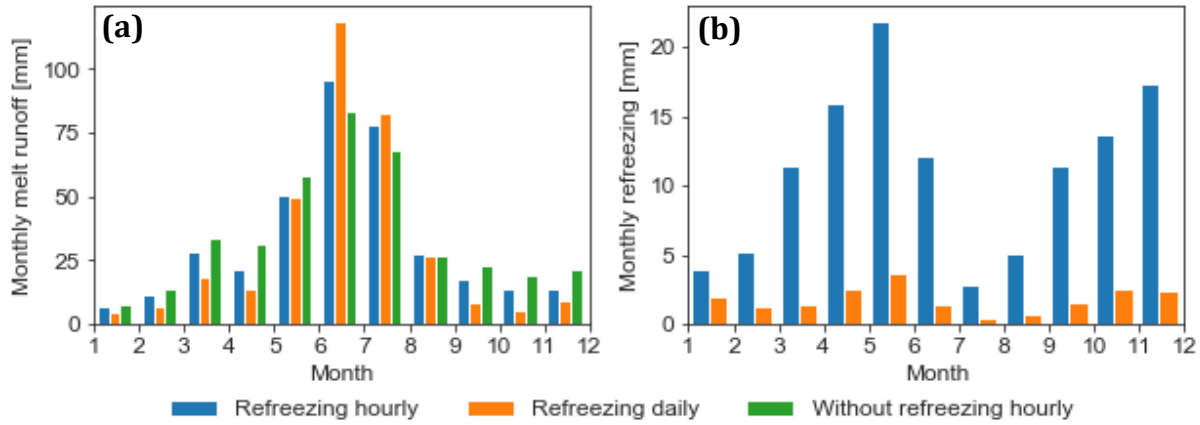
FIGURE 38 | Monthly average **(a)** melt runoff for the hourly and daily runs with refreezing and the hourly run without refreezing and **(b)** refreezing for hourly and daily runs with refreezing.

TABLE 7 | Annual average refreezing, SWE, snowfall, melt, melt runoff, rain runoff and the associated relative difference and the refreezing ratio for the reference run, daily run and run without refreezing.

		Refreezing hourly	Refreezing daily	Without refreezing
Refreezing	(mm)	131	23	-
Difference	(%)	-	-82	-
Snowfall	(mm)	431	394	431
Difference	(%)	-	-8.6	-
Melt	(mm)	482	362	392
Difference	(%)	-	-25	-19
Melt runoff	(mm)	368	347	392
Difference	(%)	-	-5.7	+6.5
Rain runoff	(mm)	1014	1058	1027
Difference	(%)		+4.3	+1.3
SWE	(mm)	405	355	312
Difference	(%)	-	-12	-23

3.5 Climate sensitivity analysis

In order to study the model sensitivity to climatic changes we performed multiple runs with changed temperature, precipitation and shortwave shortwave radiation. Four experiments were performed with changed temperature, four with changed precipitation, one with simultaneously changed temperature and precipitation and one with changed incoming shortwave radiation. The absolute and relative differences between the experiments and the main model run are calculated as a measure of sensitivity.

3.5.1 Temperature and precipitation sensitivity

Increased temperatures result in less snowfall and thus less SWE accumulation, which causes less refreezing below 6,000 m a.s.l. and less melt runoff below 5,700 m a.s.l. (Figure 39a). Increased temperatures result in more melt at high elevations, and therefore more refreezing above 6,000 m a.s.l. and more melt runoff above 5,700 m a.s.l. Increased temperatures also cause an seasonal shift in the melt runoff due to an earlier melt onset, with more melt runoff in the winter and pre-monsoon and less melt runoff in the monsoon (Figure 40a). A seasonal shift of the refreezing with

more refreezing in March and April and less refreezing in the other months occurs accordingly. The total refreezing is significantly lower (-34%) with a temperature rise of 2°C.

Decreased temperatures results in more snowfall, and thus more SWE accumulation, which causes more refreezing below 5,700 m a.s.l. and less melt runoff below 5,200 m a.s.l. (Figure 39a). Decreased temperatures result in less melt at higher elevations, and therefore less refreezing and melt runoff above 5,700 m a.s.l. Decreased temperature cause a later melt onset, with less melt runoff in the winter and pre-monsoon and more melt runoff in the monsoon (Figure 40a). A seasonal shift of the refreezing with less refreezing in March and April and more refreezing in the monsoon occurs accordingly.

The increase in precipitation results in more snowfall and thus more SWE accumulation, which causes a small increase in refreezing and melt runoff mainly in the post-monsoon and a small increase in the melt and rain runoff (Figures 39b and 40b). While a decrease in precipitation leads to less snowfall and thus less SWE accumulation and therefore less refreezing mainly in the post monsoon, and less melt and rain runoff (Figures 39b and 40b). The total refreezing is 6.9% higher with an increase in precipitation of 10%.
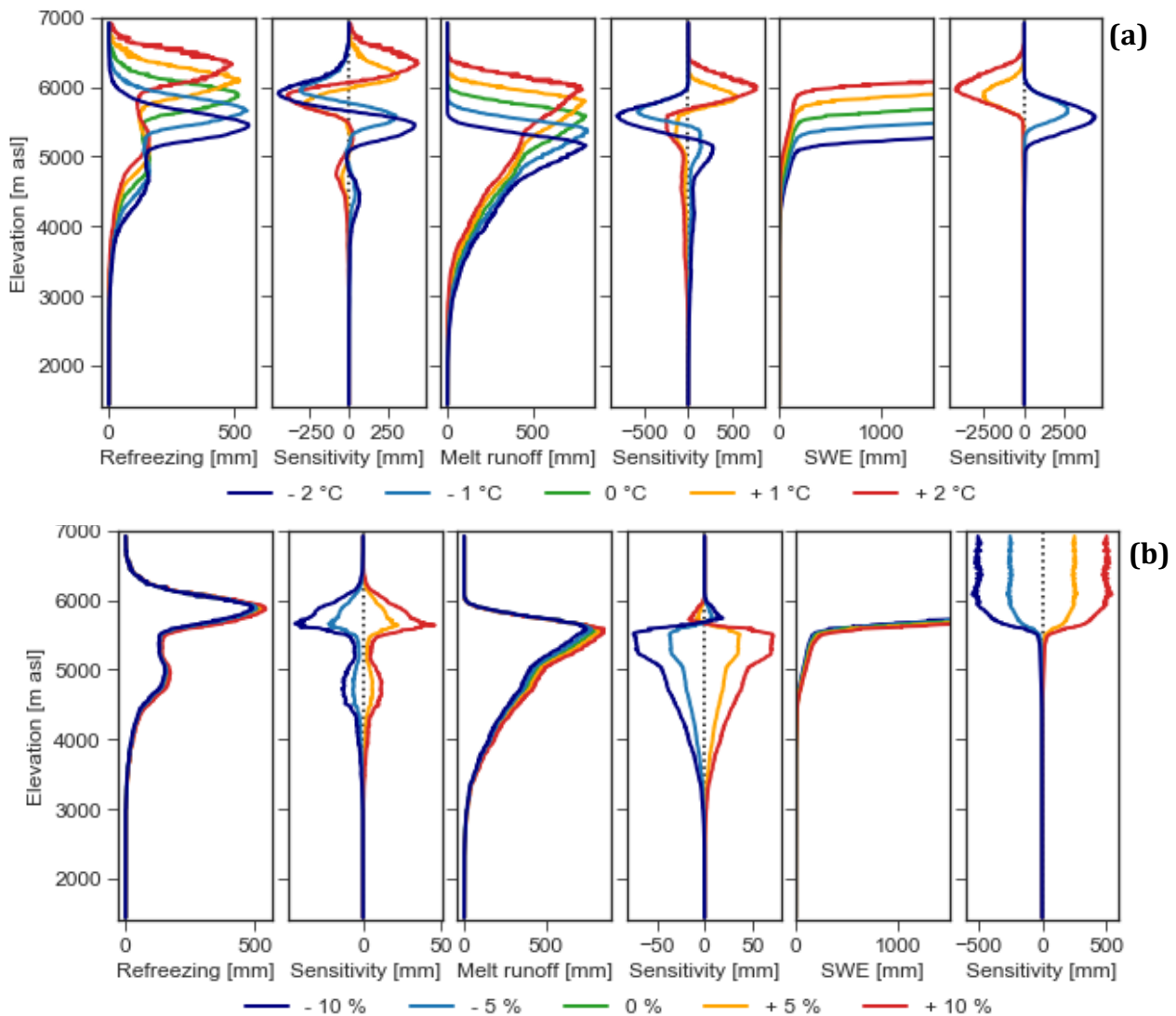
FIGURE 39 | Elevation profiles of refreezing, melt runoff and average SWE with **(a)** temperature and **(b)** precipitation changes and the associated absolute sensitivities averaged over 10-m elevation bins.

Figure 39 reveals that the model is mainly sensitive to temperature and precipitation variations above 5,500 m a.s.l. The model responds linearly, with opposite effects of equal magnitude to an increase and decrease in either temperature or precipitation. The model is highly sensitive to temperature changes and rather insensitive to precipitation changes.

Increasing temperature and precipitation thus have opposite effects on the SWE accumulation. This is confirmed by the results of the experiment with the simultaneous increase of temperature (+2°C) and precipitation (+10%), where the effect of increased temperature is partially compensated by increased precipitation (Figure 41). Therefore, the difference of refreezing (-30%)
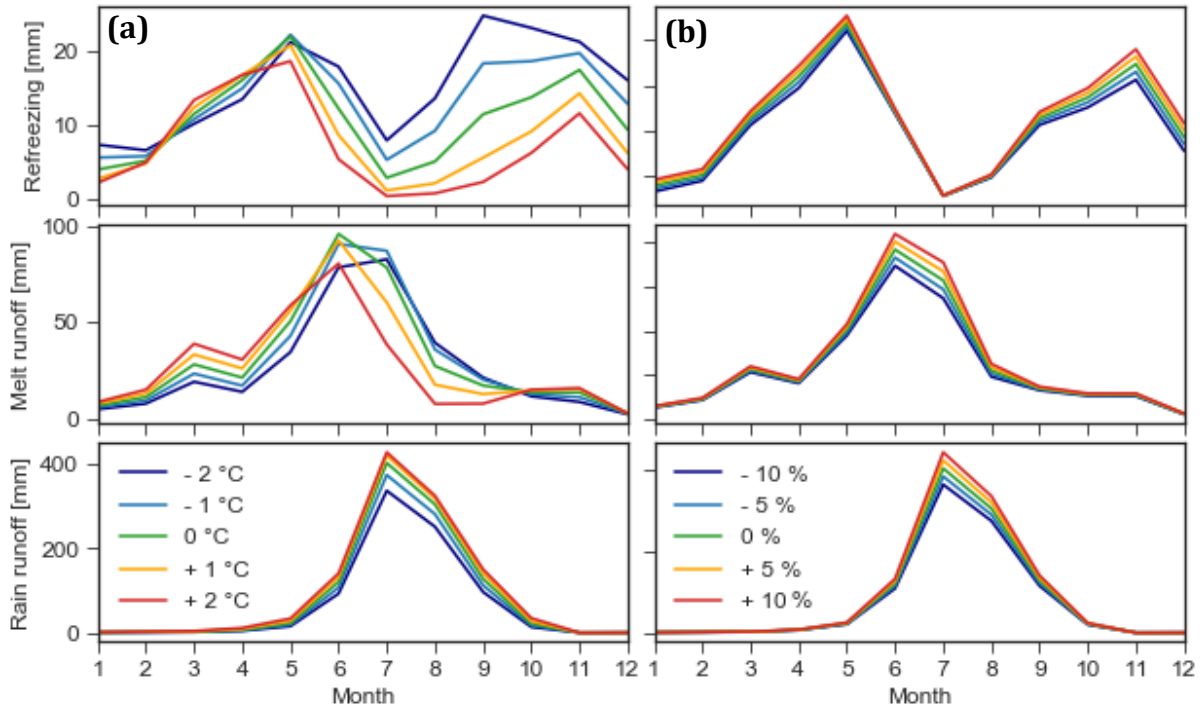
FIGURE 40 | Monthly average refreezing, melt runoff and rain runoff with the **(a)** temperature and **(b)** precipitation changes.
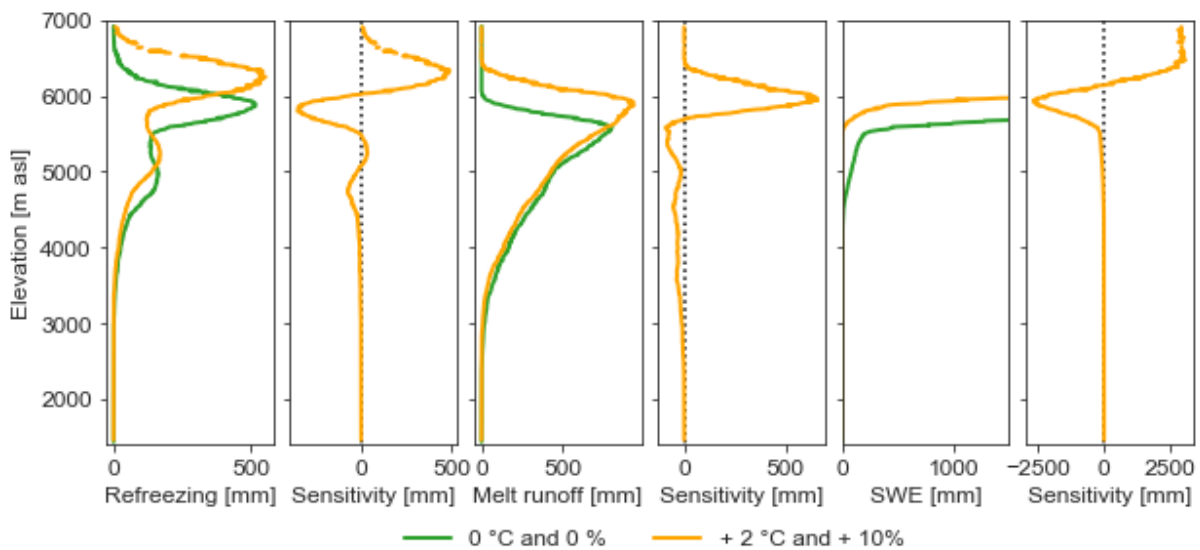
FIGURE 41 | Elevation profiles of refreezing, melt runoff and average SWE with simultaneously changed temperature (+2°C) and precipitation (+10%) and the associated absolute sensitivities averaged over 10-m elevation bins.
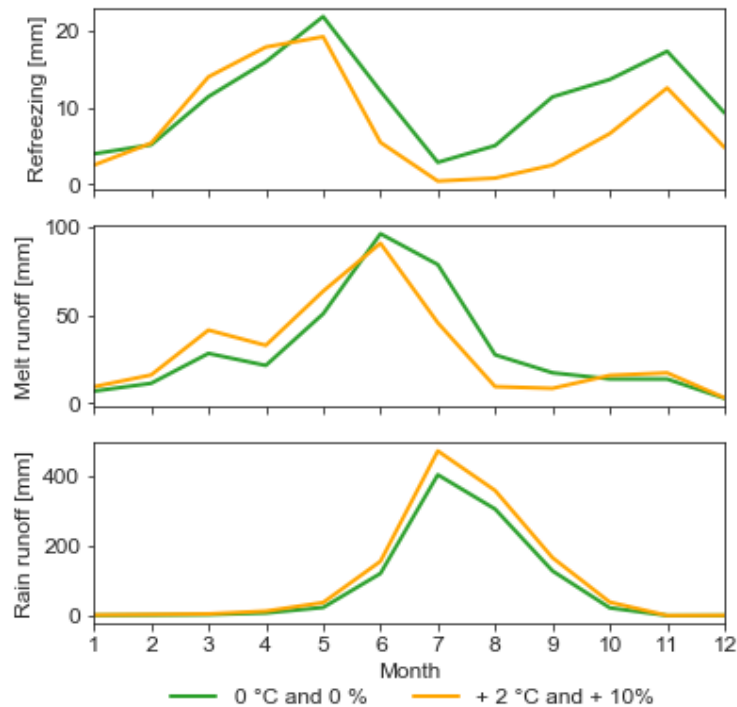
FIGURE 42 | Monthly average refreezing, melt runoff and rain runoff with simultaneously changed temperature (+2°C) and precipitation (+10%).

is smaller than for the +2°C temperature run (-34%). Accordingly, the seasonal shift in the melt runoff is also slightly less pronounced, with a higher peak in June (Figure 42). The model results, apart from the rain runoff, are more similar to the temperature run than to the precipitation run, which confirm the greater sensitivity to temperature changes than precipitation changes. This is illustrated by the fact that an temperature increase of 1°C and 2°C already results in respectively 17% and 35% less snowfall for the entire catchment. Additionally, air temperature intervenes with more processes than SWE accumulation, such as melt, refreezing and albedo decay. The catchment average refreezing, melt runoff and rain runoff output of the temperature and precipitation experiments are listed in Table 8, which indeed reveal that the model is more sensitive to temperature than precipitation changes.

TABLE 8 | Annual average catchment-wide refreezing, melt runoff and rain runoff and the associated relative sensitivities of the temperature, precipitation and incoming shortwave radiation experiments.

	Refreezing (mm)	Sensitivity (%)	Melt runoff (mm)	Sensitivity (%)	Rain runoff (mm)	Sensitivity (%)
Main run	131	-	368	-	1015	-
-2°C	182	+39	326	-11	816	-20
-1°C	158	+21	360	-2.2	923	-9.0
+1°C	105	-20	353	-4.1	1085	+7.0
+2°C	87	-34	321	-13	1136	+12
-10%	121	-7.6	335	-9.0	914	-9.9
-5%	126	-3.8	351	-4.6	964	-4.9
+5%	135	+3.1	384	+4.4	1065	+5.0
+10%	140	+6.9	400	+8.7	1115	+10
+2°C,+10%	93	-30	353	-4.1	1249	+23
500m	104	-21	399	+8.4	1025	+1.1

3.5.2   *Incoming shortwave radiation sensitivity*

The annual average catchment-wide incoming shortwave radiation derived from the 500-m DEM (272 W m^{-2}) is significantly higher than derived from the 90-m DEM (126 W m^{-2}). This is caused by less shading from the surrounding topography, and results in more solar melt, less temperature melt and an earlier melt onset and more melt runoff from September to November (Figures 43 and 44). As a result of increased solar melt, the refreezing, total melt and melt runoff are also higher above 5,700 m a.s.l. (Figure 43). The refreezing and total melt are lower below 5,700 m a.s.l., which indicate that there melt-refreeze cycles are reduced. The refreezing peak between 4,500 and 5,000 m a.s.l. is less pronounced and the total refreezing is significantly lower (-21%)(Table 8). As opposed to the +2°C experiment, there is no seasonal refreezing shift, and refreezing is lower in each month (Figure 44).

FIGURE 43 | Elevation profiles of refreezing, melt runoff, average SWE, solar melt, temperature melt and total melt with incoming shortwave radiation derived from a 90-m and 500-m DEM and the associated sensitivities averaged
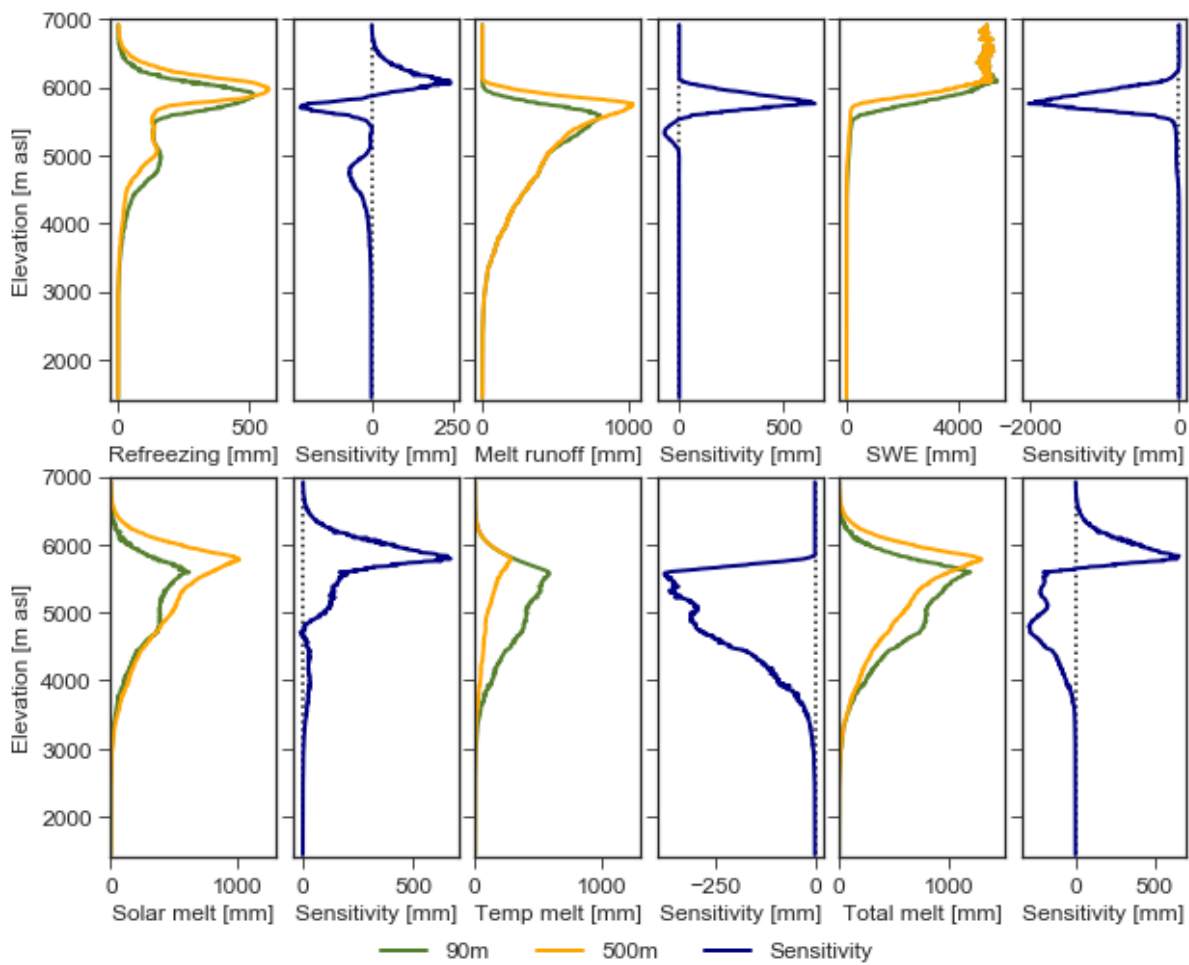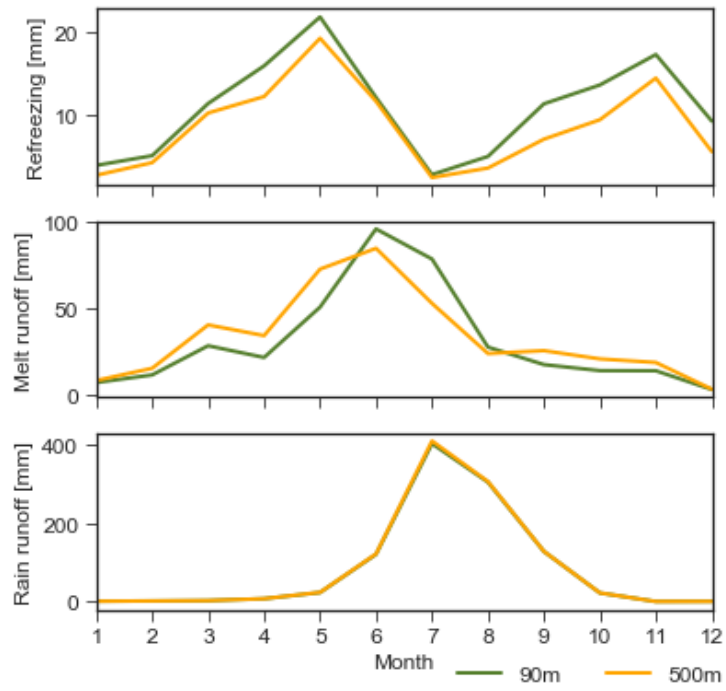
FIGURE 44 | Monthly average refreezing, melt runoff and rain runoff with incoming shortwave radiation derived from a 90-m and a 500-m DEM.

4   DISCUSSION

4.1   Forcing data

4.1.1   Air temperature

The annual average temperature of about 4°C at AWS Kyangjin is in line with meteorological observations obtained in the past and the associated temperature trends (Upreti et al. 2017). Also, the daily and monthly variability of the time-series at AWS Kyangjin is similar as observed in other studies, with highest and most constant temperatures during the monsoon (Immerzeel et al. 2014). The derived temperature lapse rates are also in line with values and patterns found by previous studies in the catchment (e.g. Immerzeel et al. 2014; Heynen et al. 2016) and Nepal (Kattel et al. 2013). Those studies found the same seasonal variability, with steepest lapse rates in the pre-monsoon season and shallowest in the monsoon season. The difference in relative humidity is the most important reason for this seasonal variability, since latent heat is released during the condensation of water droplets as water is lifted upwards (Immerzeel et al. 2014). Thick cloud cover during the monsoon therefore results in shallow lapse rates. The steepest lapse rates in the pre-monsoon season, might also be related to snow cover, which is more abundant at higher elevations and increase the albedo, which results in cooling (Kattel et al. 2013).

The lapse rates also have a high diurnal variability with also a seasonal variation in the diurnal cycle. In all seasons, the steepest lapse rates are found during the day. However, the diurnal cycle of both the temperature and the lapse rate are less pronounced during the monsoon since cloud cover limits incoming shortwave radiation during the day, while it increases the incoming longwave radiation during the night (Heynen et al. 2016). The correlation is lowest in the morning, due to differences in incoming shortwave radiation as the sun rises. Due to the shallower lapse rates during the night and steeper lapse rates during the day, the magnitude of the diurnal temperature fluctuations generally decrease with elevation. The result show that the lapse rates seem consistent over multiple years with R-squared values close to one. The highest inter-annual variability and the lowest correlations are found in the winter and the post-monsoon seasons, which are related to extreme infrequent snowfall events (Heynen et al. 2016). Some studies suggest that the lapse rates are constant within seasons (Kattel et al. 2013; Immerzeel et al. 2014). However, our results reveal that there are intra-seasonal differences in the pre-monsoon, winter and post-monsoon seasons, which are most pronounced in the pre-monsoon, which is in agreement with Heynen et al. (2016). These intra-seasonal differences are caused by transitions to either wetter or drier conditions and by snow cover transitions within seasons. The frequent temperature fluctuations around the refreezing point between 4,000 – 5,000 m a.s.l. is in line with Saloranta et al. (2019).

In many snow and glacier models a constant moist adiabatic lapse rate of -0.0065 °C m^{-1} is used, despite the evident seasonal and diurnal variability. This assumed lapse rate is steeper than most derived lapse rates in this study, expect for some pre-monsoon values during the day. The use of the moist adiabatic lapse rate would therefore mostly lead to underestimations (up to 7.5°C) and overestimations (up to 3.5°C) of the temperatures at elevations, respectively higher and lower than AWS Kyangjin.

In summary, our results show that the monthly and hourly variability of lapse rates in the catchment are high. The extreme topography leads to temperature variations of up to 40°C across the catchment, which strongly influences melt, refreezing and snowfall processes. Consequently, snow models are highly sensitive to even small temperature lapse rates changes (Stigter et al. 2017). The use of seasonal lapse rates results in shifts of several hundred meters of the 0°C isotherm

(Heynen et al. 2016). The use of sub-diurnal and seasonal lapse rates in snow models is therefore essential in catchments with extreme topography and hourly and monthly lapse rates are preferred. As is done in this study, temperature measurements covering a few years and at various elevations capture the variability of the lapse rates with R-squared values close to one.

Our analysis shows that the lapse rates seem relatively constant across the catchment, however several studies suggest that there is a complex spatial variability related to aspect, shading, proximity to debris covered glaciers and moraines and valley and katabatic winds (e.g. Kattel et al. 2015; Steiner and Pellicciotti, 2016; Heynen et al. 2018). None of the meteorological stations are located on debris covered glacier and only few in the proximity, while debris covered glacier area covers about 10% of the catchment (Collier and Immerzeel, 2014). The associated effects on lapse rates might therefore be significant but not captured. However, due to the thermal insulation effect of snow, this is not expected to have a large impact on snowmelt and refreezing processes.

While elevation is generally highly correlated with temperature, spatial variability could explain the lower correlation during sunrise and winter, when the incoming shortwave radiation spatial differences are highest. Since this is beyond the scope of this research and has not been investigated in-depth, further comprehensive research is encouraged to gain more understanding about the spatial variability of lapse rates. By developing distributed or multiple linear regression models, more accurate temperature distribution in catchments with extreme topography, could be provided. However, since many processes are involved which are not all completely known yet, this would entail a large uncertainty for now. Therefore, in this study the use of lapse rates based on elevation alone suffices.

4.1.2 Precipitation

The annual cumulative precipitation at AWS Kyangjin is in line with meteorological observations obtained in the past (Upreti et al. 2017). The seasonal variability of the time-series at AWS Kyangjin is likewise similar as observed in other studies, with (i) most frequent events and most precipitation in the monsoon season, (ii) more extreme but less events in winter and (ii) less precipitation in pre- and post-monsoon seasons (Immerzeel et al. 2014). The WRF simulations, overestimate precipitation compared to the observations, especially for the months January-May. Since no wind measurements were available at Pluvio Morimoto and Pluvio Yala, they could not be corrected for undercatch, which contributes to the disagreement. (e.g. Goodison et al. 1997). However, the undercatch of snow from precipitation winter events is estimated to be 20-40% in the catchment (Collier and Immerzeel, 2015; Kirkham et al. 2019) and thus only partly explains this disagreement. While the WRF simulations overestimate precipitation, the spatial patterns of precipitation seems to be captured reasonable well with WRF. The spatial precipitation patterns agree with previous findings based on WRF simulations, with peak values found around 3,000 m a.s.l. where the topography blocks the large-scale winds during the monsoon, and above 5,000 m a.s.l. in the non-monsoon seasons (Collier and Immerzeel, 2015). The increase in precipitation with elevation above 3,862 m a.s.l. is also in line with meteorological observations in the catchment obtained in the past (Baral et al. 2014; Fujita et al. 1997; Seko, 1987). Rainfall and snowfall predominantly occur after 15:00 and before 08:00, as is confirmed in other studies (Baral et al. 2014), which is caused by downslope winds due to radiative cooling (Ohata et al. 1981).

The average catchment-wide snowfall of 431 mm year^{-1} (29% of the annual precipitation) is considerably lower than the value of 1222 mm in about 1.5 year found by Stigter et al. (2017). The relative contribution is somewhat lower than the 42% of Bonekamp et al. (2019), while it is

higher than the estimate of 211 mm year^{-1} (17% of the annual precipitation) of Immerzeel et al. (2014). However, as is evident from the time-series at AWS Kyangjin there are substantial intra-annual precipitation variations, which together with differences in methodology could explain the disagreement. The comparison of the precipitation at AWS Kyangjin in the study of Stigter et al. (2017) with a dataset from 1988 to 2009 indeed revealed that the precipitation was exceptionally high during that study period. The overestimated WRF simulations could also be related to intra-annual differences.

The total precipitation estimate of 1241 mm year^{-1} of Immerzeel et al. (2014) is comparable to our modelled value of 1463 mm year^{-1}. The amount of precipitation that falls during the monsoon (85%) is also in line with previous observations (Immerzeel et al. 2014). Bonekamp et al. (2018) found that 52% of the annual precipitation falls between December and May, which is close to the 59% of our results. The lower intensities but similar cumulative precipitation of the scaled precipitation from Langshisha indicate that there might be a spatial pattern of precipitation intensities, with decreasing intensities towards the east or with elevation. However, no clear spatial trends in precipitation intensities have yet been observed above 3,000 m a.s.l. (Immerzeel et al. 2014; Bharti et al. 2016). As is done in this study, the combination of high-resolution WRF simulations with precipitation observations captures the seasonal and spatial precipitation patterns in the catchment. This method is therefore a promising alternative to the commonly used uniform catchment-wide precipitation lapse rates, which are unable to capture the complex spatial variability (Immerzeel et al. 2014).

4.1.3   Incoming shortwave radiation

The annual average modelled shortwave radiation at AWS Yala Glacier (153 W m^{-2}) is similar to other observations (177 W m^{-2}) (Yoshimura, 1993). The seasonal variability with least shortwave radiation during the monsoon, due to cloudiness, also agrees with previous findings (Adhikari, 2012; de Kok et al. 2019). The disagreement between the modelled and observed shortwave radiation at AWS Yala BC during the monsoon seems to be the result of overestimated transmissivity, however the transmissivity of that specific pixel was exceptionally high. As touched upon in the results, the disagreement between the observed clear-sky shortwave radiation and the observed shortwave radiation of AWS Kyangjin and AWS Yala Glacier is probably caused by the measuring device being positioned horizontally, while the surfaces of the pixels have a slope of 16 - 18°. This results in different values, with the inclined surface receiving more radiation in the winter as a result of the surface being positioned more perpendicular to the direction of the solar radiation beam. Less radiation is received in the summer when the sun is high and the surface is being positioned more oblique to the direction of the solar radiation beam. When the direction of the solar beam is more oblique to the surface, the received solar radiation is spread over a larger area. This also explains that the pattern is present at AWS Kyangjin and AWS Yala Glacier, which are located on gentle slopes (respectively 18° and 16°), and not at Yala, which is located on a more horizontal slope (4°). It also explains that the peak values in winter at AWS Kyangjin are slightly higher than at AWS Yala Glacier. Accordingly, the modelled pattern at the AWSs is similar as observed at inclined surfaces at similar latitude with similar aspect and slope (Allen et al. 2006; Shyam and Rajeev, 2011). Therefore, the modelled incoming shortwave radiation is considered to be reliable forcing data, despite the discrepancy with the observations. For the scaling of the observed incoming shortwave radiation with modelled ratio fields, it is recommended that the solar

radiation should be measured parallel to the slope of the pixel, as previously suggested by Buri et al. (2016). Buri et al. (2016) also suggests that on north-facing inclined surfaces, the direct radiation is low due to self-shading. Sakai et al. (1998) also observed that south-facing slopes receive most shortwave radiation in horizontal unit area.

The solar altitude angle is highest at 12:00 throughout the year, which is somewhat earlier than the modelled peak values. For AWS Yala Glacier and AWS Kyangjin, this can be explained by their south-western aspect. For Yala, this might be the result of shading from the surrounding topography. In winter the maximum altitude angle of the sun is 38°, while in the monsoon the maximum latitude angle is 89° (suncalc.org). This explains that during the monsoon the incoming shortwave radiation is evenly distributed in the catchment. On average, south-facing slopes receive most and north-facing slopes receive least radiation. West-facing and east-facing slopes receive a similar amount of incoming shortwave radiation, with west-facing slopes receiving most radiation in the afternoon and east-facing slopes in the morning. Temperatures in the afternoon are generally higher than in the morning, which is expected to enhance melt processes at west-facing slopes compared to east-facing slopes.

The peak values of the clear-sky radiation at the AWSs are close to the solar constant of 1362 Wm^{-2}. This can be attributed to the high elevation and low latitude, and therefore negligible depletion of radiation within the atmosphere (Adhikari, 2012). The extreme topography and the common presence of snow surfaces, which have a high albedo, result in a high amount of received reflected shortwave radiation (Lee et al. 2011), however this is not possible to take into account with the methodology used in our study. The extreme topography also results in considerable shading, which seems to be exacerbated at AWS Yala BC and AWS Yala Glacier based on the comparison with the observations. To conclude, the complex topography, the uncertainty in cloudiness, and variety in reflectance of the surface makes quantifying incoming shortwave radiation in the catchment challenging.

4.2   Model results

The snow cover fraction, snow depth and SWE outputs are generally in good agreement with the observations, which gives a useful confirmation about the model performance. The model captures the seasonal, inter-annual and spatial variability of the snowpack. The better agreement of the daily runs than the hourly runs with the MODIS observations, is probably caused by overestimation of the snow cover by the MODIS observations (Stigter et al. 2017; Kirkham et al. 2019) and the daily runs, which is also supported by better agreement of the hourly runs with the snow depth and SWE observations.

Refreezing significantly influences the snow mass balance, with a contribution of 131 mm $year^{-1}$ (35% of the melt runoff). Refreezing is most pronounced in the non-monsoon season, which coincides with findings of Saloranta et al. (2019). 27% of the total melt refreezes and 42% of the non-monsoon melt, which is somewhat lower but in reasonable agreement with the estimates of respectively 36% and 48% of Saloranta et al. (2019). For the overlapping two years (July 2016- June 2018) the results are more similar, with 30% of the total melt and 44% of the non-monsoon melt that refreezes. The modest discrepancies could be related to differences in model forcing and parameter values, such as the use of daily average lapse rates and the use of a threshold temperature for onset of melt of -3°C, which is substantially lower than our value of 0°C. Since the lapse rates are shallower during the night and steeper during the day, using average daily lapse rates overestimates the temperatures during the day and underestimate the temperatures during the night

above the elevation of the location (4200 m a.sl. for their study and 3,862 m a.s.l. for our study) from which is extrapolated. Most refreezing occurs above these elevations. Therefore, refreezing is overestimated with the use of daily lapse rates. Based on residual energy flux calculations Bonekamp et al. (2019) found that refreezing could amount to 60% of the total melt in the catchment. However, this is almost certainly overestimated as this study assumes unlimited liquid water availability for refreezing, which explains the discrepancy with our results. Surface energy balance calculations at AWS Yala BC show that 31% of the total melt refreezes (Stigter, 2020 *personal communication*), which is also somewhat higher than our modelled value of 25% at that location. However, surface energy balance calculations include longwave radiation and turbulent fluxes of sensible and latent heat, which also have a clear diurnal cycle and might contribute to diurnal melt and refreeze cycles (Stigter et al. 2018; de Kok et al. 2019).

Refreezing contributes 23% of the annual SWE accumulation, which is line with findings in the Arctic of Pelt et al. (2016). This mainly involves meltwater refreezing and only a small contribution (estimated 2.3% of the accumulated SWE) of rain refreezing. Kirkham et al. (2019) estimated, based on field observations, that refreezing of rainwater contributes 10-15% of the accumulated SWE at a single location at an elevation of 4,962 m a.s.l. very close to the Langtang catchment, while in the 4,750 – 5,000 m a.s.l. elevation band of our results, rainfall only contributes 4.0% of the annual SWE accumulation. However, the refreezing of rainwater in their study mainly occurred during mixed precipitation events below -2°C, while our rain-snow temperature threshold is 0°C, which explains this disagreement.

Most studies focus on the ratio between refreezing and melt (Saloranta et al. 2019; Fujita et al. 1996). However, in our study, we focus on the ratio between refreezing and melt runoff, referred to as the refreezing ratio, since the melt runoff is a measure of the accumulated SWE that has melted whereas the melt increases due to recycling in melt-refreezing cycles, which reduces the significance of refreezing.

4.2.1   Spatial patterns

The main model run yields highest refreezing above 5,750 m a.s.l. followed by the 5,500 – 5,750 m a.s.l. elevation band. The elevation of 5,500 m a.s.l. matches the equilibrium line altitude (5,455 m a.s.l. and 5,400 m a.s.l.) in the catchment (Baral et al. 2014; Ragettli et al. 2015). However, although this is certainly overestimated due to substantial overestimation of SWE, previous studies also observed highest refreezing in the accumulation zone of glaciers (Fujita et al. 1996; Van Pelt et al. 2012; Ayala et al. 2017b). It is therefore possible that also without the overestimation, the refreezing is highest above 5500 m a.s.l. However, it should be noted that the lack of redistribution also results in an underestimation of SWE and therefore underestimation of refreezing, at lower elevation.

Refreezing and the refreezing ratio both have a strong relation with elevation, with increasing refreezing with elevation until 5,900 m a.sl. and a prominent peak (respectively 157 mm and 0.38) in the 4,750 - 5,000 m a.s.l. elevation band (Figure 26). A similar pattern has been found at a similar latitude in the Andes, with a peak value of 610 mm (~50% of the melt) between 4,500 – 5,000 (Ayala et al. 2017b). The absence of melt runoff above 6090 m a.sl. indicates that all meltwater that is generated, either refreezes or is retained by the snowpack. This elevation is higher than the elevation (> 5,500 m a.sl.) assumed by Ragettli et al. (2015). The two prerequisites for refreezing are availability of meltwater and below zero temperatures, and the primary drivers of the spatial pattern are therefore, the amount of SWE and the magnitude of the diurnal fluctuations around the freezing point. A higher amount of SWE supplies and retains more meltwater, which

potentially refreezes and fluctuations around the freezing point generate and consequently refreeze meltwater.

The peak of refreezing and refreezing ratio in the 4,750 – 5,000 m a.s.l. elevation band is at a slightly higher elevation than the peak of the temperature fluctuations around the freezing point, which is the result of increasing SWE with elevation. Besides the amount of SWE and the magnitude of diurnal temperature fluctuations around the freezing point, refreezing and refreezing ratio also have a clear relation with aspect, with generally less refreezing and a lower refreezing ratio on south- and southwest-facing slopes at equal elevation than on north- and northeast-facing slopes. This is related to more incoming shortwave radiation at the south-facing slopes and most during the afternoon at southwest-facing slopes when temperatures are highest. This results in a quicker generation of meltwater during the day with temperatures above the freezing point. Therefore, more meltwater is released by the snowpack, and less meltwater is available for refreezing during the night. On the contrary, above 5,600 m a.s.l. the refreezing is higher on south-facing slopes, which can be explained by more total melt. Remarkably, the refreezing and refreezing ratio are higher on south-facing slopes between respectively 5,000 – 5,300 m a.s.l., indicating that higher incoming shortwave radiation enhances the melt-refreeze cycles. This can probably be explained by the relatively high amount of SWE, which can retain more meltwater, in combination with the fact that there is more melt at close to zero temperatures, which subsequently refreezes when the temperature drops below zero (Bookhagen and Burbank, 2010). This is also supported by the fact that the solar melt and refreezing peak coincides in the 4,750 – 5,000 m a.s.l. elevation band.

4.2.2   Temporal patterns and effects on runoff

The amount of SWE and the magnitude of diurnal fluctuations around the freezing point also govern the seasonal pattern of refreezing, with most refreezing in the pre-monsoon and post-monsoon seasons. The refreezing in the pre-monsoon season is important for the timing of the melt onset. This is illustrated in Figures 23, whereby different refreezing approaches yield different timings of the melt onset. Refreezing in the post-monsoon season is mainly important for the accumulation of SWE over the winter. This is especially important when there is much snowfall in the post-monsoon, as in October 2013. Refreezing in the winter and pre-monsoon is important for retaining SWE. These effects of refreezing are supported by the results of the run without refreezing, where more melt runoff, and an earlier onset of melt runoff, with more melt in the non-monsoon seasons and less melt in the monsoon is modelled, which indicates that refreezing delays runoff and retains SWE.

Refreezing also has a clear diurnal pattern, which is associated with temperature and incoming shortwave radiation fluctuations and meltwater availability (Figure 33). Refreezing is generally highest from 18:00 – 20:00, although temperatures and incoming shortwave radiation are lower after 20:00. This is caused by more availability of meltwater within the snowpack, which diminishes due to the refreezing. The melt and melt runoff also have a clear diurnal pattern, associated with temperature and incoming shortwave radiation fluctuations. The results show that both temperature and solar melt are generally higher in the afternoon (12:00-18:00) than in the morning (06:00-12:00), which is caused by higher temperatures.

The high "diurnal" refreezing contribution of the total refreezing (67% catchment-wide and 85% below 5,500 m a.s.l.) emphasizes the importance of modelling with a sub-daily time step to capture melt-refreeze cycles. This is illustrated by the outputs of the daily run, whereby melt (-

120 mm; -25%) and refreezing (-108 mm; -82%) are substantially lower. This generally results in a later melt onset, with more melt runoff during the monsoon and a less melt runoff during the non-monsoon seasons. Modelling with a sub-daily time step is also important to account for the diurnal precipitation pattern. Most precipitation occurs during the evening and night (18:00 – 06:00), when temperatures are generally lowest (Figure 9; Figure 18). Thus, the temperature at which most precipitation occurs is lower than the average daily temperature, which results in more snowfall. If most precipitation would have occurred during the day, this would have resulted in less snowfall.

Intra-annual differences in refreezing are primarily caused by fluctuations in snowfall, especially during the post-monsoon and pre-monsoon, which result in more SWE accumulation. This is in particular evident for the high amount of snowfall during the post-monsoon season of 2013. Monthly average temperature and diurnal temperature fluctuations around the freezing point have a lower inter-annual variability, which is in line with previous observations (Stigter et al. 2017) and generally show a less clear relation with refreezing. This agrees with other studies, who found that there is a substantial inter-annual variability of snow dynamics in the Langtang catchment, which is predominantly controlled by the large inter-annual variability of snowfall (Seko and Takahashi, 1991; Girona-Mata et al. 2019). However, uncertainties in undercatch, the rain-snow temperature threshold and the spatial variability of precipitation make quantifying snowfall challenging. The inter-annual variability of both the refreezing (107 -159 mm) and the refreezing ratio (0.25 - 0.44) stresses the importance of using multiple year time-series to quantify refreezing.

4.3 Climate sensitivity analysis

The climatic sensitivity experiments reveal that the model is highly sensitive to temperature changes and rather insensitive to precipitation changes. The model responds reasonable linearly with opposite effects of increasing and decreasing temperature or precipitation.

Increasing temperatures (+2°C) lead to significantly less refreezing (-44 mm; -34%), due less snowfall and thus less accumulation of SWE. It also causes an earlier melt runoff onset, and accordingly more refreezing in March and April. The higher amount of refreezing in March and April counteracts the earlier melt onset, which reveals that refreezing influences the melt runoff timing response to temperature changes. Excluding refreezing therefore results in an exaggerated seasonal shift. This seasonal refreezing shift and the high sensitivity shows that including refreezing is highly relevant for the modeling of snow dynamics and runoff a changed future climate.

An increase in precipitation (+10%) results in more refreezing (+9 mm; +6.9%), due to more snowfall and thus more SWE accumulation. The results of the sensitivity analysis are in good agreement with previous Arctic refreezing studies (Van Pelt et al. 2012). Van Pelt et al. (2016) also observed a seasonal shift of refreezing to earlier in the year with increased temperature. The higher sensitive to temperature changes is illustrated by the fact that 2°C temperature increase already results in a 35% decrease of snowfall. Additionally, temperature intervenes with more processes than SWE accumulation, such as melt, refreezing and albedo decay.

Since increased temperature and precipitation have opposite effects, the model is less sensitivity to the run with simultaneously changed temperature (+2°C) and precipitation (+10%) to the run with changed temperature (+2C°). The run with simultaneously increased temperature and precipitation also results in a seasonal melt runoff shift, with decreased monsoon melt runoff and increased pre-monsoon melt runoff. Accordingly, similar seasonal shifts are projected in several other Himalayan studies with increased temperature and precipitation (e.g. Jeelani et al. 2012; Lutz et al. 2016; Stigter et al. 2017).

The model is also highly sensitive to the shortwave incoming radiation change. Incoming shortwave radiation derived from the 500-m DEM, yields substantially higher annual average catchment-wide incoming shortwave radiation (277 Wm^{-2}) than derived from the 90-m DEM (126 W m^{-2}), as a result of less shading. This agrees with Olsen et al. (2019), which shows that with a 500-m DEM resolution, there is a overestimation of over 100 W m^{-2}. This higher incoming shortwave radiation results in substantial less refreezing (-27 mm; -21%) and an earlier melt onset. This stresses the importance of using accurate incoming shortwave radiation forcing data when modelling refreezing or melt runoff.

The model is thus most sensitive to the temperature and incoming shortwave radiation changes. As discussed in previously, there is a higher uncertainty related to the incoming shortwave radiation than the temperature input data. Therefore, incoming shortwave radiation is presumably the largest source of error.

4.4 Limitations and proposed further research

An important limitation of our study is that the model is not calibrated. Therefore, the next step should be to calibrate the model. In addition, it is proposed to validate the refreezing parameterization with field measurements, such as with multiple temperature measurements at different depths in the snowpack to obtain temperature profiles (Wright et al. 2007), or with Time Domain Reflectometry (TDR) probes, which measure snow water content (Samimi and Marshall, 2017) or by measuring ice layers within a snow pit. However, despite that the model is not calibrated, the results are in reasonable agreement with the observations and results of other studies, as has been discussed previously. Moreover, this study aims to explore the importance, and reveal patterns and effects of refreezing, which have been unknown so far. Thereby the focus was on process-understanding and providing a setup for and giving direction to future research.

There are various uncertainties related to model input and model parameters, from which the meteorological forcing data, as is discussed previously, is likely the most important one. In addition to our climate sensitivity analysis, future work could focus on quantifying the sensitivity of the model to the lapse rate uncertainty. Another important uncertainty is the threshold temperature for onset of melt, which we assumed to be 0°C, which is in line with most studies (Ragettli et al. 2015). However, no clear consensus about this parameter exists and consequently varying values are used (Pellicciotti et al. 2012; Ragettli et al. 2015). Changing this parameter influences the model's outputs, which certainly deserves attention in future work.

There are also various model simplifications, from which the excluding of snow redistribution and sublimation are likely the most important ones. Ignoring the redistribution of snow from higher to lower elevation by wind and snow avalanches, and ignoring sublimation results in increasingly accumulation of SWE and overestimation of refreezing above 5,500 m a.s.l. This overestimation is in agreement with Saloranta et al. (2019) who found that the exclusion of sublimation and avalanching results in a 73% higher SWE between 5,500 and 6,000 m a.s.l. However, the lack of redistribution results in a lower SWE and thus underestimation of refreezing at lower elevation. In Saloranta et al. (2019), the excluding of avalanching resulted in a 25% lower SWE between 4,500 m a.s.l. and 5,000 m a.s.l. Stigter et al. (2017) found that 31% of the snowfall is transported to lower elevation due to avalanching in the catchment. Additionally, it has been observed that wind-induced snow transport is substantial, and mostly occurs from convex areas such as ridges to concave areas such as valley bottoms, thereby contributing to the redistribution of snow from higher to lower elevations (Winstral et al. 2002).

Observations revealed that sublimation is a significant component of the water balance (21% of the annual snowfall) on Yala Glacier at 5,350 m a.s.l. in the Langtang catchment (Stigter et al. 2018). The results show that sublimation increases with elevation as drier and more wind-exposed conditions prevail. This is in agreement with the results of a study in the Andes, which show the importance of sublimation increases with elevation due to a lower humidity, higher wind speeds and higher incoming solar radiation (Ayala et al. 2017a). Ignoring sublimation therefore also contributes to the overestimation of SWE at higher elevations. Ayala et al. (2017a) argues that enhanced-temperature index models are unable to capture the melt and refreezing well at high elevation, sublimation-favourable conditions. Since we used an enhanced temperature-index model, we did also not include the influence of longwave radiation on melt. However, longwave radiation is an important energy source for melt especially in cloudy conditions during the monsoon (de Kok et al. 2019). Surface energy balance models include longwave radiation, and in addition make it possible to include a physically based parameterization of sublimation. This requires distributed fields of wind speed, relative humidity, actual vapor pressure and surface temperature, which are challenging to quantify. This is beyond the scope of this research, but encouraged for future work, as it is expected to increase model's performance.

Another simplification is that, this study focuses on the mass-retaining effect of refreezing, while refreezing also has indirect effects on the snowpack. After refreezing, the release of latent heat and solid mass retention affects the conductive heat flux, snow density and snow surface albedo which in turn enhance melt and runoff. The effect of refreezing on the mass balance of a glacier in the Arctic is therefore -31% smaller than the amount of refreezing itself (Van Pelt et al. 2016). The effect of refreezing on conductive heat flux and snow surface albedo are not taken into account in this study, however did include the effect of refreezing on snow density.

Some studies, predominantly in the Arctic and Antarctica (e.g. Jonsell et al. 2012), also include the effect of the solar angle on the albedo, which is beyond to scope of this research. However, the effect is expected to be minor in alpine catchments (Van Angelen et al. 2012). Future work could focus on the sensitivity of the simulated diurnal melt-refreeze cycles to albedo changes. We did also not include vegetation in our model, as opposed to some other snow models (e.g. Kumar et al. 2013), however substantial vegetation is only present at low elevation, where refreezing is negligible. Additionally, since the model is a simplified one-layer model, this study has not attempted to address the role of preferential flow paths, the formation of water lenses and the cold content of snowpacks.

4.5   Contribution to science and society

The motivation of this study arose from the lack of understanding of the importance and role of refreezing, and the ignoring of refreezing by most studies. While a number of limitations and uncertainties and exists, the results are found promising. The results show that refreezing significantly influences the snow mass balance and plays an important role in snow persistence and melt runoff timing. This points out that it has been wrongly ignored by previous studies, while it can be modelled with temperature, precipitation and incoming shortwave radiation forcing only.

We have characterize, for the first time to our knowledge, the spatial and temporal patterns, and the effect on melt runoff of refreezing in the current and a changed future climate at a catchment-scale in the Himalaya. The revealed spatial and temporal patterns and effects on melt runoff of refreezing enhance our understanding about snow dynamics in the Himalaya. This hydrological understanding is important for the prediction of the effects of climate change on snow

dynamics. Since climate change will cause seasonal runoff changes, it is especially important that we understand the processes involved in snow persistence and melt runoff timing, such as refreezing, in order to make reliable runoff projections. By providing first insights of the importance and role of refreezing, this study also serves as a setup and motivation for future research in the Himalaya to further investigate and account for refreezing.

The increased understanding about refreezing thus improves the prediction of timing and volume of melt runoff in the current and a changed future climate. This is extremely valuable for the long-term planning of hydropower and irrigation reservoirs, which are required to secure enough water supply in this vulnerable region. The timing and volume of melt runoff are especially important for the high irrigation water demands in the pre-monsoon, when melt runoff is the predominant component of runoff (Bookhagen and Burbank, 2010). Melt runoff in the non-monsoon seasons is also important to sustain enough runoff for hydropower generation, which meets about 95% of electric demand in Nepal (Sharma and Shakya, 2006). It is important to have knowledge about changing water availability well in advance, such that there is enough time to find fair and effective solutions in this political instable region with many large transboundary rivers. In addition, more accurate hydrological forecasting will improve short-term water management and flood forecasting.

5   CONCLUSION

The aim of this study was to gain insight in the importance and role of snowmelt refreezing in the Himalaya. This was done by using the modified seNorge model (v2.0), which includes a physically based parameterization of refreezing based on Stefan's Law. We have characterized, for the first time to our knowledge, the spatial and temporal patterns, and the effect on melt runoff of refreezing in the current and a changed future climate at a catchment-scale in the Himalaya. The validation shows a good correspondence between the snow satellite imaginary and in-situ snow depth and SWE observations, which provides confidence about the model performance.

We found that refreezing significantly influences the snow mass balance in the Langtang catchment, with a contribution of 131 mm year^{-1} (35% of the melt runoff). The spatial and temporal pattern of refreezing are predominantly controlled by the amount of SWE and the magnitude of the diurnal temperature fluctuations around the freezing point. Therefore, refreezing has a strong relation with elevation and increases up to 5,900 m a.s.l. with a peak between 4,750 – 5,000 m a.s.l. Refreezing also has a relation with aspect, with generally less refreezing on south-facing and southwest-facing slopes, related to earlier melt. Refreezing mostly occurs in the pre- and post-monsoon seasons. Intra-annual variability is primarily caused by variations of snowfall in the post-monsoon and winter. 67% of the refreezing occurs during the same day (05:00 – 06:00) that the melt is generated, which emphasizes the importance of using sub-daily temporal resolution to capture melt-refreeze cycles. This is supported by the outputs of the daily run, which yield substantially lower refreezing (-82%) and melt (-25%) compared to the hourly run. The results show that refreezing is important for snow persistence and the timing of melt runoff, and excluding it in models consequently results in an earlier melt runoff onset. Refreezing thus has been wrongly ignored by previous studies.

Sensitivity tests reveal that the model is highly sensitive to temperature changes, as refreezing is significantly lower (-34%) with a 2°C temperature increase. Future climate change will cause a seasonal runoff shift, with predominantly more runoff in the pre-monsoon and less in the monsoon. The results reveal that refreezing influences the response of the snowpack to future climate change, as it moderates this seasonal runoff shift. The model is also highly sensitive to changes in incoming shortwave radiation, as refreezing is substantially lower (-21%) with incoming shortwave radiation derived from a coarser DEM.

The results enhance our understanding about snow dynamics in the Himalaya. This hydrological understanding is important for the prediction of the effects of climate change. The study also illustrates the importance and need to account for refreezing in order to provide reliable melt runoff timing. This knowledge therefore contributes to hydrological forecasting and effective watershed management in the current and a changed future climate in this vulnerable region. This is highly important for the irrigation and hydropower water demand, especially in the pre-monsoon, when melt runoff is the predominant component of runoff. By providing first insights, the results also serve as a setup and motivation for future research in the Himalaya to further investigate and include refreezing. We conclude that including refreezing with a sub-daily time step is required for a detailed assessment of snow and is highly relevant for the modeling of runoff in the current and a changed future climate in the Himalaya.

ACKNOWLEDGEMENTS

REFERENCES

Adhikari, S. (2012). Seasonal and spatial variation of solar radiation in Nepal Himalayas. Journal of Hydrology and Meteorology, 8(1), 1-9.

Alfnes, E. 2008 Snow depth algorithms – compaction of snow. NVE internal report.

Allen, R. G., Trezza, R., & Tasumi, M. (2006). Analytical integrated functions for daily solar radiation on slopes. Agricultural and Forest Meteorology, 139(1-2), 55-73.

Anders, A. M., Roe, G. H., Hallet, B., Montgomery, D. R., Finnegan, N. J., & Putkonen, J. (2006). Spatial patterns of precipitation and topography in the Himalaya. *Special Papers-Geological Society of America*, *398*, 39.

Armstrong, R. L., & Brun, E. (Eds.). (2008). *Snow and climate: physical processes, surface energy exchange and modeling.* Cambridge University Press.

Avanzi, F., De Michele, C., Morin, S., Carmagnola, C. M., Ghezzi, A., & Lejeune, Y. (2016). Model complexity and data requirements in snow hydrology: seeking a balance in practical applications. *Hydrological processes*, *30*(13), 2106-2118.

Ayala, A., Pellicciotti, F., MacDonell, S., McPhee, J., & Burlando, P. (2017a). Patterns of glacier ablation across N orth-C entral C hile: Identifying the limits of empirical melt models under sublimation-favorable conditions. Water Resources Research, 53(7), 5601-5625.

Ayala, A., Pellicciotti, F., Peleg, N., & Burlando, P. (2017b). Melt and surface sublimation across a glacier in a dry environment: distributed energy-balance modelling of Juncal Norte Glacier, Chile. Journal of Glaciology, 63(241), 803-822.

Baral, P., Kayastha, R. B., Immerzeel, W. W., Pradhananga, N. S., Bhattarai, B. C., Shahi, S., ... & Mool, P. K. (2014). Preliminary results of mass-balance observations of Yala Glacier and analysis of temperature and precipitation gradients in Langtang Valley, Nepal. *Annals of glaciology*, *55*(66), 9-14.

Bengtsson, L. (1982). The importance of refreezing on the diurnal snowmelt cycle with application to a northern Swedish catchment. Hydrology Research, 13(1), 1-12.

Beniston, M. (2003). Climatic change in mountain regions: a review of possible impacts. In Climate variability and change in high elevation regions: Past, present & future (pp.5-31). Springer, Dordrecht.

Bharti, V., Singh, C., Ettema, J., & Turkington, T. A. R. (2016). Spatiotemporal characteristics of extreme rainfall events over the Northwest Himalaya using satellite data. International journal of climatology, 36(12), 3949-3962.

Bhatt, B. C., & Nakamura, K. (2005). Characteristics of monsoon rainfall around the Himalayas revealed by TRMM precipitation radar. Monthly weather review, 133(1), 149-165.

Biemans, H., Siderius, C., Lutz, A. F., Nepal, S., Ahmad, B., Hassan, T., ... & Immerzeel, W. W. (2019). Importance of snow and glacier meltwater for agriculture on the Indo-Gangetic Plain. Nature Sustainability, 2(7), 594-601.

Bolch, T., Kulkarni, A., Kääb, A., Huggel, C., Paul, F., Cogley, J. G., & Bajracharya, S. (2012). The state and fate of Himalayan glaciers. Science, 336(6079), 310-314.

Bonekamp, P. N. J., Collier, E., & Immerzeel, W. W. (2018). The impact of spatial resolution, land use, and spinup time on resolving spatial precipitation patterns in the Himalayas. *Journal of Hydrometeorology*, *19*(10), 1565-1581.

Bonekamp, P. N., de Kok, R. J., Collier, E., & Immerzeel, W. W. (2019). Contrasting meteorological drivers of the glacier mass balance between the Karakoram and central Himalaya. *Frontiers in Earth Science*, *7*, 107.

Bookhagen, B., & Burbank, D. W. (2010). Toward a complete Himalayan hydrological budget: Spatiotemporal distribution of snowmelt and rainfall and their impact on river discharge. *Journal of Geophysical Research: Earth Surface*, *115*(F3).

Bras, R. L. (1990). Hydrology: an introduction to hydrologic science. Addison Wesley Publishing Company.

Brock, B. W., Willis, I. C., & Sharp, M. J. (2000). Measurement and parameterization of albedo variations at Haut Glacier d'Arolla, Switzerland. Journal of Glaciology, 46(155), 675-688.

Buri, P., Miles, E. S., Steiner, J. F., Immerzeel, W. W., Wagnon, P., & Pellicciotti, F. (2016). A physically based 3-D model of ice cliff evolution over debris-covered glaciers. Journal of Geophysical Research: Earth Surface, 121(12), 2471-2493.

Colli, M., Rasmussen, R., Thériault, J. M., Lanza, L. G., Baker, C. B., & Kochendorfer, J. (2015). An improved trajectory model to evaluate the collection performance of snow gauges. *Journal of Applied Meteorology and Climatology*, *54*(8), 1826-1836.

Collier, E., & Immerzeel, W. W. (2015). High-resolution modeling of atmospheric dynamics in the Nepalese Himalaya. *Journal of Geophysical Research: Atmospheres*, *120*(19), 9882-9896.

de Kok, R. J., Steiner, J. F., Litt, M., Wagnon, P., Koch, I., Azam, M. F., & Immerzeel, W. W. (2020). Measurements, models and drivers of incoming longwave radiation in the Himalaya. International Journal of Climatology, 40(2), 942-956.

Eeckman, J., Chevallier, P., Boone, A., Neppel, L., De Rouw, A., Delclaux, F., & Koirala, D. (2017). Providing a non-deterministic representation of spatial variability of precipitation in the Everest region.

Elalem, S., & Pal, I. (2015). Mapping the vulnerability hotspots over Hindu-Kush Himalaya region to flooding disasters. Weather and Climate Extremes, 8, 46-58.

Essery, R., Morin, S., Lejeune, Y., & Ménard, C. B. (2013). A comparison of 1701 snow models using observations from an alpine site. Advances in water resources, 55, 131-148.

Fu, P., & Rich, P. M. (2002). A geometric solar radiation model with applications in agriculture and forestry. Computers and electronics in agriculture, 37(1-3), 25-35.

Fujita, K., Sakai, A., Chhetri, T. B., & Fujita, K. S. A. C. T. B. (1997). Meteorological observation in Langtang Valley, Nepal Himalayas, 1996. *Bull. Glacier Res*, *15*, 71-78.

Fujita, K., Seko, K., Ageta, Y., Jianchen, P., & Tandong, Y. (1996). Superimposed ice in glacier mass balance on the Tibetan Plateau. Journal of Glaciology, 42(142), 454-460.

Girona-Mata, M., Miles, E. S., Ragettli, S., & Pellicciotti, F. (2019). High-resolution snowline delineation from Landsat imagery to infer snow cover controls in a Himalayan catchment. Water Resources Research, 55(8), 6754-6772.

Goodison, B. E., Louie, P. Y., & Yang, D. (1998). *WMO solid precipitation measurement intercomparison* (p. 212). Geneva, Switzerland: World Meteorological Organization.

Heynen, M., Miles, E., Ragettli, S., Buri, P., Immerzeel, W. W., & Pellicciotti, F. (2016). Air temperature variability in a high-elevation Himalayan catchment. *Annals of Glaciology*, *57*(71), 212-222.

Hock, R., G. Rasul, C. Adler, B. Cáceres, S. Gruber, Y. Hirabayashi, M. Jackson, A. Kääb, S. Kang, S. Kutuzov, A. Milner, U. Molau, S. Morin, B. Orlove, and H. Steltzer, (2019). High Mountain Areas. In: IPCC Special Report on the Ocean and Cryosphere in a Changing Climate.

Hopkinson, C., Chasmer, L., Munro, S., & Demuth, M. N. (2010). The influence of DEM resolution on simulated solar radiation-induced glacier melt. Hydrological Processes: An International Journal, 24(6), 775-788.

Immerzeel, W. W., Droogers, P., De Jong, S. M., & Bierkens, M. F. P. (2009). Large-scale monitoring of snow cover and runoff simulation in Himalayan river basins using remote sensing. Remote sensing of Environment, 113(1), 40-49.

Immerzeel, W. W., Lutz, A. F., Andrade, M., Bahl, A., Biemans, H., Bolch, T., ... & Emmer, A. (2019). Importance and vulnerability of the world's water towers. *Nature*, 1-1.

Immerzeel, W. W., Petersen, L., Ragettli, S., & Pellicciotti, F. (2014). The importance of observed gradients of air temperature and precipitation for modeling runoff from a glacierized watershed in the Nepalese Himalayas. *Water Resources Research*, *50*(3), 2212-2226.

Immerzeel, W. W., Van Beek, L. P., & Bierkens, M. F. (2010). Climate change will affect the Asian water towers. Science, 328(5984), 1382-1385.

Immerzeel, W. W., Van Beek, L. P. H., Konz, M., Shrestha, A. B., & Bierkens, M. F. P. (2012). Hydrological response to climate change in a glacierized catchment in the Himalayas. Climatic change, 110(3-4), 721-736.

Jain, S. K., Goswami, A., & Saraf, A. K. (2010). Snowmelt runoff modelling in a Himalayan basin with the aid of satellite data. International Journal of Remote Sensing, 31(24), 6603-6618.

Jeelani, G., Feddema, J. J., van der Veen, C. J., & Stearns, L. (2012). Role of snow and glacier melt in controlling river hydrology in Liddar watershed (western Himalaya) under current and future climate. Water Resources Research, 48(12).

Jonsell, U. Y., Navarro, F. J., Bañón García, M., Lapazaran, J. J., & Otero, J. (2012). Sensitivity of a distributed temperature-radiation index melt model based on AWS observations and surface energy balance fluxes, Hurd Peninsula glaciers, Livingston Island, Antarctica.

Karki, R., ul Hasson, S., Schickhoff, U., Scholten, T., Böhner, J., & Gerlitz, L. (2019). Near surface air temperature lapse rates over complex terrain: a WRF based analysis of controlling factors and processes for the central Himalayas. *Climate Dynamics*, 1-21.

Karssenberg, D., Burrough, P. A., Sluiter, R., & de Jong, K. (2001). The PCRaster software and course materials for teaching numerical modelling in the environmental sciences. Transactions in GIS, 5(2), 99-110.

Kattel, D. B., Yao, T., Yang, W., Gao, Y., & Tian, L. (2015). Comparison of temperature lapse rates from the northern to the southern slopes of the Himalayas. *International Journal of Climatology*, *35*(15), 4431-4443.

Kattel, D. B., Yao, T., Yang, K., Tian, L., Yang, G., & Joswiak, D. (2013). Temperature lapse rate in complex mountain terrain on the southern slope of the central Himalayas. *Theoretical and applied climatology*, *113*(3-4), 671-682.

Kirkham, J. D., Koch, I., Saloranta, T. M., Litt, M., Stigter, E., Møen, K., ... & Immerzeel, W. W. (2019). Near real-time measurement of snow water equivalent in the Nepal Himalayas. Frontiers in Earth Science, 7, 177.

Kobierska, F., Jonas, T., Zappa, M., Bavay, M., Magnusson, J., & Bernasconi, S. M. (2013). Future runoff from a partly glacierized watershed in Central Switzerland: A two-model approach Advances in Water Resources, 55, 204-214.

Kochendorfer, J., Rasmussen, R., Wolff, M., Baker, B., Hall, M. E., Meyers, T., ... & Leeper, R. (2017). The quantification and correction of wind-induced precipitation measurement errors. Hydrology and Earth System Sciences, 21(4), 1973.

Konz, M., Uhlenbrook, S., Braun, L., Shrestha, A., & Demuth, S. (2007). Implementation of a process-based catchment model in a poorly gauged, highly glacierized Himalayan headwater.

Kraaijenbrink et al. 2020 Under review.

Kulkarni, A. V., Rathore, B. P., & Singh, S. K. (2010). Distribution of seasonal snow cover in central and western Himalaya. Annals of Glaciology, 51(54), 123-128.

Kumar, M., Marks, D., Dozier, J., Reba, M., & Winstral, A. (2013). Evaluation of distributed hydrologic impacts of temperature-index and energy-based snow models. Advances in Water Resources, 56, 77-89.

Lee, W. L., Liou, K. N., & Hall, A. (2011). Parameterization of solar fluxes over mountain surfaces for application to climate models. Journal of Geophysical Research: Atmospheres, 116(D1).

Leppäranta, M. (1983). A growth model for black ice, snow ice and snow thickness in subarctic basins. Hydrology Research, 14(2), 59-70.

Leppäranta, M. (1993). A review of analytical models of sea-ice growth. Atmosphere-Ocean, 31(1), 123-138.

Litt, M., Shea, J., Wagnon, P., Steiner, J., Koch, I., Stigter, E., & Immerzeel, W. (2019). Glacier ablation and temperature-indexed melt models in the Nepalese Himalaya. *Scientific reports*, *9*(1), 5264.

Lundquist, J. D., Pepin, N., & Rochford, C. (2008). Automated algorithm for mapping regions of cold-air pooling in complex terrain. *Journal of Geophysical Research: Atmospheres*, *113*(D22).

Lutz, A. F., Immerzeel, W. W., Kraaijenbrink, P. D. A., Shrestha, A. B., & Bierkens, M. F. (2016). Climate change impacts on the upper indus hydrology: Sources, shifts and extremes. PloS one, 11(11), e0165630.

Lutz, A. F., Immerzeel, W. W., Shrestha, A. B., & Bierkens, M. F. P. (2014). Consistent increase in High Asia's runoff due to increasing glacier melt and precipitation. *Nature Climate Change*, *4*(7), 587.

Magnusson, J., Wever, N., Essery, R., Helbig, N., Winstral, A., & Jonas, T. (2015). Evaluating snow models with varying process representations for hydrological applications. Water Resources Research, 51(4), 2707-2723.

Marshall, S. J., & Sharp, M. J. (2009). Temperature and melt modeling on the Prince of Wales ice field, Canadian High Arctic. *Journal of Climate*, *22*(6), 1454-1468.

Maussion, F., Scherer, D., Mölg, T., Collier, E., Curio, J., & Finkelnburg, R. (2014). Precipitation seasonality and variability over the Tibetan Plateau as resolved by the High Asia Reanalysis. *Journal of Climate*, *27*(5), 1910-1927.

Muhammad, S., & Thapa, A. A combined Terra/Aqua MODIS snow-cover and RGI6. 0 glacier product (MOYDGL06*) for the High Mountain Asia between 2002 and 2018.

Nepal, S., & Shrestha, A. B. (2015). Impact of climate change on the hydrological regime of the Indus, Ganges and Brahmaputra river basins: a review of the literature. International Journal of Water Resources Development, 31(2), 201-218.

Ohata, T., Higuchi, K., & Ikegami, K. (1981). Mountain-valley wind system in the Khumbu Himal, East Nepal. Journal of the Meteorological Society of Japan. Ser. II, 59(5), 753-762.

Ohmura, A. (2001). Physical basis for the temperature-based melt-index method. Journal of applied Meteorology, 40(4), 753-761.

Olson, M., Rupper, S., & Shean, D. (2019). Terrain induced biases in clear-sky shortwave radiation due to digital elevation model resolution for glaciers in complex terrain. Frontiers in Earth Science, 7, 216.

Palazzi, E., Von Hardenberg, J., & Provenzale, A. (2013). Precipitation in the Hindu-Kush Karakoram Himalaya: observations and future scenarios. Journal of Geophysical Research: Atmospheres, 118(1), 85-100.

Pellicciotti, F., Brock, B., Strasser, U., Burlando, P., Funk, M., & Corripio, J. (2005). An enhanced temperature-index glacier melt model including the shortwave radiation balance: development and testing for Haut Glacier d'Arolla, Switzerland. *Journal of Glaciology*, *51*(175), 573-587.

Pellicciotti, F., Buergi, C., Immerzeel, W. W., Konz, M., & Shrestha, A. B. (2012). Challenges and uncertainties in hydrological modeling of remote Hindu Kush–Karakoram–Himalayan (HKH) basins: suggestions for calibration strategies. Mountain Research and Development, 32(1), 39-50.

Pepin, N., Bradley, R. S., Diaz, H. F., Baraër, M., Caceres, E. B., Forsythe, N., ... & Miller, J. R. (2015). Elevation-dependent warming in mountain regions of the world. Nature climate change, 5(5), 424-430.

Petersen, L., & Pellicciotti, F. (2011). Spatial and temporal variability of air temperature on a melting glacier: atmospheric controls, extrapolation methods and their effect on melt modeling, Juncal Norte Glacier, Chile. *Journal of Geophysical Research: Atmospheres*, *116*(D23).

Ragettli, S., Bolch, T., & Pellicciotti, F. (2016). Heterogeneous glacier thinning patterns over the last 40 years in Langtang Himal, Nepal. The Cryosphere.

Ragettli, S., Pellicciotti, F., Immerzeel, W. W., Miles, E. S., Petersen, L., Heynen, M., ... & Shrestha, A. (2015). Unraveling the hydrology of a Himalayan catchment through integration of high resolution in situ data and remote sensing with an advanced simulation model. *Advances in Water Resources*, 78, 94-111.

Rangwala, I., Palazzi, E., & Miller, J. R. (2020). Projected Climate Change in the Himalayas during the Twenty-First Century. In Himalayan Weather and Climate and their Impact on the Environment (pp. 51-71). Springer, Cham.

Reijmer, C. H., Van den Broeke, M. R., Fettweis, X., Ettema, J., & Stap, L. B. (2012). Refreezing on the Greenland ice sheet: a comparison of parameterizations. The Cryosphere, 6, 743-762.

Ruiz-Arias, J. A., Tovar-Pescador, J., Pozo-Vázquez, D., & Alsamamra, H. (2009). A comparative analysis of DEM-based models to estimate the solar radiation in mountainous terrain. International Journal of Geographical Information Science, 23(8), 1049-1076.

Rutter, N., Essery, R., Pomeroy, J., Altimir, N., Andreadis, K., Baker, I., ... & Douville, H. (2009). Evaluation of forest snow processes models (SnowMIP2). *Journal of Geophysical Research: Atmospheres*, *114*(D6).

Sakai, A., Nakawo, M., & Fujita, K. (1998). Melt rate of ice cliffs on the Lirung Glacier, Nepal Himalayas, 1996. Bull. Glacier Res, 16, 57-66.

Saloranta, T. M. (2012). Simulating snow maps for Norway: description and statistical evaluation of the seNorge snow model. The Cryosphere, 6(6), 1323.

Saloranta, T. M. (2014). Simulating more accurate snow maps for Norway with MCMC parameter estimation method. *The Cryosphere Discussions,* , 8(2).

Saloranta, T. M. (2016). Operational snow mapping with simplified data assimilation using the seNorge snow model. Journal of Hydrology, 538, 314-325.

Saloranta, T. M., Thapa, A., Kirkham, J., Koch, I., Melvold, K., Stigter, E., ... & Møen, K. (2019). A model setup for mapping snow conditions in High-Mountain Himalaya. Frontiers in Earth Science, 7, 129.

Samimi, S., & Marshall, S. J. (2017). Diurnal cycles of meltwater percolation, refreezing, and drainage in the supraglacial snowpack of Haig glacier, Canadian Rocky Mountains. Frontiers in Earth Science, 5, 6.

Seko, K. (1987). Seasonal variation of altitudinal dependence of precipitation in Langtang Valley, Nepal Himalayas. *Bulletin of glacier research*, *5*, 41-47.

Seko, K., & Takahashi, S. (1991). Characteristics of winter precipitation and its effect on glaciers in the Nepal Himalaya. Bulletin of Glacier Research, (9), 9-16.

Sevruk, B., Hertig, J. A., & Spiess, R. (1991). The effect of a precipitation gauge orifice rim on the wind field deformation as investigated in a wind tunnel. *Atmospheric Environment. Part A. General Topics*, *25*(7), 1173-1179.

Sharma, R. H., & Shakya, N. M. (2006). Hydrological changes and its impact on water resources of Bagmati watershed, Nepal. Journal of Hydrology, 327(3-4), 315-322.

Shea, J. M., Wagnon, P., Immerzeel, W. W., Biron, R., Brun, F., & Pellicciotti, F. (2015). A comparative high-altitude meteorological analysis from three catchments in the Nepalese Himalaya. *International Journal of Water Resources Development*, *31*(2), 174-200.

Shrestha, U. B., Gautam, S., & Bawa, K. S. (2012). Widespread climate change in the Himalayas and associated changes in local ecosystems. PloS one, 7(5).

Shyam S, C., & Rajeev K, A. (2011). Estimation of hourly solar radiation on horizontal and inclined surfaces in Western Himalayas. Smart grid and renewable energy, 2011.

Skamarock, W. C., & Klemp, J. B. (2008). A time-split nonhydrostatic atmospheric model for weather research and forecasting applications. *Journal of computational physics*, *227*(7), 3465-3485.

Smith, T., Bookhagen, B., & Rheinwalt, A. (2017). Spatiotemporal patterns of High Mountain Asia's snowmelt season identified with an automated snowmelt detection algorithm, 1987–2016. The Cryosphere, 11(5), 2329.

Stefan, J. (1891) Über die Theorie der Eisbilding, insbesondere iiber Eisbildung im Polar- meere. Ann. Physik, 3rd Ser., 42, 269-286

Steinegger, U., Braun, L. N., Kappenberger, G., & Tartari, G. (1993). Assessment of annual snow accumulation over the past 10 years at high elevations in the Langtang region. IAHS Publications-Publications of the International Association of Hydrological Sciences, 218, 155-166.

Steiner, J. F., & Pellicciotti, F. (2016). Variability of air temperature over a debris-covered glacier in the Nepalese Himalaya. Annals of Glaciology, 57(71), 295-307.

Steiner, J. F., Pellicciotti, F., Buri, P., Miles, E. S., Immerzeel, W. W., & Reid, T. D. (2015). Modelling ice-cliff backwasting on a debris-covered glacier in the Nepalese Himalaya. Journal of Glaciology, 61(229), 889-907.

Stigter, E. E., Litt, M., Steiner, J. F., Bonekamp, P. N., Shea, J. M., Bierkens, M. F., & Immerzeel, W. W. (2018). The importance of snow sublimation on a Himalayan glacier. Frontiers in Earth Science, 6, 108.

Stigter, E. E., Wanders, N., Saloranta, T. M., Shea, J. M., Bierkens, M. F., & Immerzeel, W. W. (2017). Assimilation of snow cover and snow depth into a snow model to estimate snow water equivalent and snowmelt runoff in a Himalayan catchment. Cryosphere, 11(4), 1647-1664.

Stranden, H. B., Ree, B. L., and Møen, K. M. (2015). Recommendations for Automatic Measurements of Snow Water Equivalent in NVE. Majorstua: Norges vassdrags- og energidirektorat.

Thapa, S., Li, B., Fu, D., Shi, X., Tang, B., Qi, H., & Wang, K. (2020). Trend analysis of climatic variables and their relation to snow cover and water availability in the Central Himalayas: a case study of Langtang Basin, Nepal. Theoretical and Applied Climatology, 1-13.

Thériault, J. M., Rasmussen, R., Ikeda, K., & Landolt, S. (2012). Dependence of snow gauge collection efficiency on snowflake characteristics. Journal of applied meteorology and climatology, 51(4), 745-762.

Uppala, S. M., Kållberg, P. W., Simmons, A. J., Andrae, U., Bechtold, V. D. C., Fiorino, M., ... & Li, X. (2005). The ERA-40 re-analysis. Quarterly Journal of the Royal Meteorological Society: A journal of the atmospheric sciences, applied meteorology and physical oceanography, 131(612), 2961-3012.

Upreti, B. N., Dhakal, S., Bhattarai, T. N., Adhikari, B. R., Bajracharya, S. R., & Yoshida, M. (2017). Climate change impact on glacier retreat and local community in the Langtang Valley, Central Nepal. Journal of Development Innovations, 1(1), 45-59.

Van Angelen, J., Lenaerts, J., Lhermitte, S., Fettweis, X., Kuipers Munneke, P., Van den Broeke, M., & Van Meijgaard, E. (2012). Sensitivity of Greenland Ice Sheet surface mass balance to surface albedo parameterization: a study with a regional climate model. Cryosphere, 6, 1175-1186.

Van Pelt, W. J. J., Oerlemans, J., Reijmer, C. H., Pohjola, V. A., Pettersson, R., & Van Angelen, J. H. (2012). Simulating melt, runoff and refreezing on Nordenskiöldbreen, Svalbard, using .a coupled snow and energy balance model. The Cryosphere, 6, 641-659.

Van Pelt, W. J., Pohjola, V. A., & Reijmer, C. H. (2016). The changing impact of snow conditions and refreezing on the mass balance of an idealized Svalbard glacier. Frontiers in Earth Science, 4, 102.

Vionnet, V., Brun, E., Morin, S., Boone, A., Faroux, S., Le Moigne, P., ... & Willemet, J. M. (2012). The detailed snowpack scheme Crocus and its implementation in SURFEX v7. 2.

Wang, Q., Fan, X., & Wang, M. (2014). Recent warming amplification over high elevation regions across the globe. Climate Dynamics, 43(1-2), 87-101.

Wester, P., Mishra, A., Mukherji, A., & Shrestha, A. B. (2019). The Hindu Kush Himalaya Assessment. Cham: Springer International Publishing: Basel, Switzerland.

Whiteman, C. D. (2000). *Mountain meteorology: fundamentals and applications*. Oxford University Press.

Winstral, A., Elder, K., & Davis, R. E. (2002). Spatial snow modeling of wind-redistributed snow using terrain-based parameters. Journal of hydrometeorology, 3(5), 524-538.

Wolff, M., Isaksen, K., Brækkan, R., Alfnes, E., Petersen-Øverleir, A., & Ruud, E. (2013). Measurements of wind-induced loss of solid precipitation: description of a Norwegian field study. *Hydrology Research*, *44*(1), 35-43.

Wolff, M. A., Isaksen, K., Petersen-Øverleir, A., Ødemark, K., Reitan, T., & Brækkan, R. (2015). Derivation of a new continuous adjustment function for correcting wind-induced loss of solid precipitation: results of a Norwegian field study. *Hydrology and Earth System Sciences*, *19*(2), 951-967.

Wright, A. P., Wadham, J. L., Siegert, M. J., Luckman, A., Kohler, J., & Nuttall, A. M. (2007). Modeling the refreezing of meltwater as superimposed ice on a high Arctic glacier: A comparison of approaches. Journal of Geophysical Research: Earth Surface, 112(F4).

Wu, J., Xu, Y., & Gao, X. J. (2017). Projected changes in mean and extreme climates over Hindu Kush Himalayan region by 21 CMIP5 models. Advances in Climate Change Research, 8(3), 176-184.

Wulf, H., Bookhagen, B., & Scherler, D. (2016). Differentiating between rain, snow, and glacier contributions to river discharge in the western Himalaya using remote-sensing data and distributed hydrological modeling. Advances in Water Resources, 88, 152-169.

Xu, J., Grumbine, R. E., Shrestha, A., Eriksson, M., Yang, X., Wang, Y. U. N., & Wilkes, A. (2009). The melting Himalayas: cascading effects of climate change on water, biodiversity, and livelihoods. Conservation Biology, 23(3), 520-530.

Ye, B., Yang, D., Ding, Y., Han, T., & Koike, T. (2004). A bias-corrected precipitation climatology for China. *Journal of Hydrometeorology*, *5*(6), 1147-1160

Yen, Y. C. (1981). Review of thermal properties of snow, ice and sea ice (No. CRREL-81-10). Cold Regions Research and Engineering Lab Hanover NH.

Yoshimura, Y. (1993). Biotic Acceleration of Glacier Melting in Yala Glacier9 Langtang Region, Nepal Himalaya.